

ENTANGLED STATE PREPARATION FOR OPTICAL
QUANTUM COMMUNICATION:
Creating and characterizing photon pairs from Spontaneous
Parametric Down Conversion inside bulk uniaxial crystals

Alexander LING Euk Jin

A THESIS SUBMITTED FOR THE DEGREE OF PhD

DEPARTMENT OF PHYSICS
NATIONAL UNIVERSITY OF SINGAPORE

SINGAPORE, 2008

Contents

Summary	v
List of Tables	vii
List of Figures	viii
1 Quantum Mechanics and Communication	1
1.1 The start of quantum communication	3
1.2 Qubit entanglement, very briefly	4
1.3 Entanglement and quantum communication	9
2 A Polarization-Entangled Photon Pair Source	12
2.1 Sources of polarization-entangled photon pairs	13
2.2 The experimental implementation	16
2.2.1 Basic principles of SPDC	16
2.2.2 Optimizing for collection bandwidth	19
2.3 Measuring the entanglement quality of a photon pair	22
2.4 Remarks on the source quality	27
3 Absolute Emission Rate of SPDC into a Single Transverse Mode	31
3.1 Introduction	31
3.2 Model	32
3.2.1 Pump mode	34
3.2.2 Collection modes	35
3.2.3 Interaction Hamiltonian	36

3.2.4	Spectral emission rate	39
3.2.5	Total emission rate	40
3.2.6	Dependence of emission rate on beam waists	42
3.3	Physical interpretation and comparison to experiments	43
3.4	Implications of the model	45
4	Complete Polarization State Characterization	46
4.1	Polarimetry and qubit state tomography	46
4.2	State estimation using the optimal polarimeter	48
4.3	State tomography for ensembles of multi-photons	51
4.4	Phase correction and polarimeter calibration	53
4.4.1	Removing unwanted phase shifts	53
4.4.2	Calibrating the polarimeter	56
4.5	Experimental state tomography for single photon ensembles	57
4.6	Experimental state tomography for a two photon ensemble	58
4.7	Remarks on the minimal polarimeter	59
5	Asymptotic Efficiency of Minimal & Optimal Polarimeters	61
5.1	Efficiency of state reconstruction	61
5.2	Average accuracy	62
5.3	Accuracy in estimating single photon states	64
5.3.1	Direct observation on a maximally polarized single photon state	64
5.3.2	Accuracy as a function of the detected number of photons	64
5.3.3	An expression for accuracy	66
5.4	Accuracy in estimating two photon states	67
5.5	Scaling law for multi-photon polarimetry	68
6	Spectral Characterization of Entangled Photon Pairs	69
6.1	Spectral correlations of photon pairs	69
6.2	Measured spectra	71
6.2.1	Downconversion spectra using a “clean” pump	71
6.2.2	Downconversion spectra using a “dirty” pump	72

7	Preparing Bell states with controlled “White Noise”	77
7.1	Introduction	77
7.2	Making noise	78
7.2.1	Inducing noise via a time window	78
7.2.2	Inducing noise via a blackbody	79
7.3	Density matrix of Werner states	82
7.4	Spectral character of the Werner state	82
8	An experimental demonstration of the Ekert QKD protocol	84
8.1	Entanglement-based QKD	84
8.2	Experiment	88
8.2.1	Monitoring polarization states	88
8.2.2	A compact SPDC source	91
8.2.3	Experimental results	91
8.3	Extending QKD beyond BB84	94
9	Experimental Falsification of the Leggett Non-local Variable Model	96
9.1	Introduction	97
9.2	Theory	99
9.3	Experiment	102
9.4	Overview and Perspectives	105
10	Final Remarks	107
A	Vector Descriptions of Polarization States	110
A.1	Linear Polarization	111
A.2	Circular Polarization	112
A.3	Jones Vector Notation	113
A.4	Stokes Vector Notation	114
B	Partially Polarizing Beam Splitter (PPBS) Specification	117
C	Spectral Broadening in type-II non-collinear SPDC	120

CONTENTS	iv
Abbreviations	122
Bibliography	124
Publications	141
Index	142

Summary

This document is a summary of my studies on the creation, characterization and use of photon pairs that are emitted from a nonlinear optical material via the process of Spontaneous Parametric Down Conversion (SPDC). In particular, I focus on photon pairs that are in an entangled polarization state.

The past decade has witnessed an accelerated pace of research work on entangled optical states because of their potential application as a new communication technology. Communication protocols employing quantum states of light are generally grouped under the heading of optical quantum communication. An optical quantum communication infrastructure will require sources of pure entangled optical states that are bright and have a narrow spectral bandwidth. Such sources are not available yet.

In order to obtain such futuristic sources, the first step would be to examine the factors governing the brightness of existing photon pair sources. In this thesis I derive a model for the brightness of an experimental SPDC source. Predictions from the model are in rough agreement with experimentally observed pair rates.

I also describe techniques to completely characterize photon pairs in their spectral and polarization degrees of freedom. The spectral correlation from the photon pairs can be used to infer the spectral character of the pump light used in SPDC and its effects on the quality of entanglement in the generated photon pairs.

A minimal and optimal method of polarimetry is also described. This method is capable of characterizing the Stokes vector of both single and multi-photon states. Maximally entangled states from the SPDC source are characterized using these techniques.

The maximally entangled photons were then used to generate states with idealized noise characteristics, known as Werner states. Two novel and simple methods of gen-

erating Werner states are provided. Both spectral and tomography methods were used to characterize Werner states.

The non-classical correlations from entangled photon pairs are also useful for studying the validity of classical models that try to describe quantum non-locality. One family of such models may be tested against quantum mechanics via a Leggett Inequality. An experiment doing so is described.

Finally I report on a field implementation of quantum key distribution using entangled photon pairs.

List of Tables

2.1	Comparison of entangled photon pair sources. It is not meant to be a complete record of all reported entangled photon sources. [†] The following abbreviations are used to denote the different physical processes used in photon pair sources: Critical Phase Matching (CPM), Four Wave Mixing (FWM) and Quasi-Phase Matching (QPM). [‡] The first three sources are not normalized to input power and have their own set of units. * Entanglement quality is evaluated by the visibility of polarization correlations and is a unitless quantity. The source that is described in this chapter is in the last row.	30
2.2	Characteristics of two heralded single photon sources. It is interesting to compare the bandwidth of the heralded single photon sources to the spectral brightness of the entangled photon sources. In this table, the bandwidth is used because it is not always easy to define the photon rate as a function of input power (e.g. for atomic systems like the one by Thompson [1]).	30
5.1	Fit parameters for the test states	67
9.1	Selected values of L violating the NLV bounds L_{NLV} for different averaging numbers N	105

List of Figures

- 1.1 Simple representation of a Stern-Gerlach experiment using an electron pair in a classical state. Consider a source that prepares electron pairs only in the spin-up direction, and where the individual electrons are interrogated by separate Stern-Gerlach apparatus (S-G). In panel (a) the Stern-Gerlach devices on both sides are in the same basis as the prepared spins. The measurement outcome for the individual electrons can be predicted with certainty (represented by a solid outline for the electron) and are correlated. In panel (b), the Stern-Gerlach apparatus measures a conjugate basis and the individual measurement outcomes and the inter-electron correlations are random (dashed lines). 6
- 1.2 Simple representation of a Stern-Gerlach experiment using an entangled electron pair. Consider a source that prepares an entangled electron pair, and where the individual electrons are interrogated by separate Stern-Gerlach apparatus (S-G). For any measurement basis (panel (a)) the measurement outcome for the electron pair is always both spin-up or both spin-down (i.e same color), but occur randomly. This is true even if the Stern-Gerlach apparatus have been rotated to a conjugate basis as in panel (b). 7
- 1.3 Criteria for evaluating entangled light sources. Three ways of evaluating entangled light sources are to look at their brightness, the quality of their entanglement and the narrowness of the spectral bandwidth of the generated light. An ideal light source will be rated highly in all three areas (and should lie in the shaded region in the centre of the figure). Sometimes brightness and bandwidth are considered together as ‘spectral brightness’. 10
- 2.1 Spontaneous parametric downconversion for fixed signal and idler wavelengths under type II phase matching conditions. The emission may be collinear with the pump field direction, or noncollinear (shown in this diagram). Here, the cones overlap at two points. Degenerate twin photons that are emitted in these overlap regions are indistinguishable apart from their polarization states, and will be polarization-entangled. This figure is adapted from reference [61]. 17

2.2	A fiber-coupled polarization-entangled photon pair source. The fiber modes are mapped onto the two intersection points in the SPDC emission. Half-wave plates and compensating crystals perform correction for longitudinal walk-off. The bandwidth of collected light is determined by the acceptance angle $\Delta\theta$ of the fiber modes. This figure is adapted from reference [99].	19
2.3	Bandwidth optimization with single mode fiber collection. The collection mode waist, W , and angular divergence, θ_D , is determined by the desired bandwidth of SPDC light that is to be selected. The pump is restricted to areas of the crystal that are observed by the fibers and this means matching it to the collection mode.	20
2.4	The emission profile of degenerate SPDC light at 702.2 nm. The emission profile calculated by assuming perfect phase matching and a plane wave pump beam is presented in (a). The emission angle for different SPDC wavelengths in the plane $\phi_{s,i} = 0^\circ$ is shown in (b). The slope of the emission angle $ d\theta/d\lambda $ at 702.2 nm is estimated to be $0.055^\circ \text{ nm}^{-1}$. . .	21
2.5	The spectra of SPDC light collected into the two single mode fibers. The FWHM of the collected spectra is 4.5 nm. The resolution of the spectrometers is approximately 0.25 nm.	22
2.6	Scheme for checking polarization correlations between a photon pair. In each arm the light is sent through a half-wave plate (HWP) and a polarizing beam splitter, before being collected and sent to photon counting detectors. The angular setting of the HWP in one arm selects for the polarization basis under test (HV or $\pm 45^\circ$). The HWP in the other arm is turned by a full revolution, and for each angle of the wave plates the number of detected photon pairs is noted.	25
2.7	Polarization correlations in two conjugate bases. The visibility of the correlation curve in the HV basis (99.9%) is higher than that for the curve in the $\pm 45^\circ$ basis (98.4%). The lower visibility in one basis is attributed to experimental alignment and compensation errors, resulting in a residual distinguishability of the HV and VH decay paths.	26
3.1	A schematic of the downconversion model considered in this chapter. The pump, signal and idler fields are treated as paraxial beams, with a Gaussian transverse intensity. The focus of all beams coincide at the crystal. The x-axis is coming out of the plane of the diagram. Coordinate systems of the signal and idler ($x_{s,i}, y_{s,i}, z_{s,i}$) are rotated about the coordinate system of the pump (x, y, z). This figure is adapted from reference [66].	33

3.2	Longitudinal overlap Φ_z/l as a function of the total phase mismatch $\Delta\varphi = Kl/2$ for various walk-off parameters Ξ . For $\Xi = 0$, the typical sinc -shaped spectral distribution is revealed, whereas for large walk-off parameters $\Xi > 1$ the phase matching condition is determined by the overlap region formed by pump- and collection modes, and Φ_z/l develops into a Gaussian-like distribution. This figure is adapted from reference [66].	38
3.3	Variation of Φ_T with walkoff parameter Ξ . The absolute emission rate is proportional to Φ_T . The largest absolute rate is obtained in the thin-crystal limit when $\Phi_T = \pi$. This figure is adapted from reference [66].	42
3.4	Dependence of the total pair rate \tilde{R}_T on the ratio γ between target and pump waist. The maximum emission rate can be expected at $\gamma = 1/\sqrt{2}$	43
4.1	Stokes vectors for minimal and optimal polarimetry. Four reduced Stokes vectors in the Poincare sphere that form a tetrahedron define the optimal POVM operators used for polarization state estimation. The tetrahedron gives the largest volume encompassable by a vector quartet in the sphere making it the optimal measurement when using four POVMs. This figure is adapted from figure [65].	49
4.2	Practical implementation of the tetrahedron polarimeter that achieves the ideal instrument matrix. Each detector b_j is associated to the tetrahedron vector \vec{b}_j . The partially polarizing beam splitter (PPBS) separates incoming light according to polarization, and quartz plates remove unwanted phase shifts. Light leaving the PPBS is passed through waveplates and polarizing beam splitters (PBS) to be projected on two different bases ($\pm 45^\circ$ basis for transmitted light and the circular basis for reflected light). This figure is adapted from figure [65].	50
4.3	Scheme for estimating the polarization state of an ensemble of N photons using N polarimeters (P1,P2,...,PN). A multiple coincidence circuit identifies the 4^N possible coincidence combinations. For photon pairs ($N=2$), two polarimeters are used giving 16 possible coincidence combinations. Several copies of the state are processed giving a coincidence pattern used in estimating the polarization state of the ensemble. This figure is adapted from figure [65].	53

4.4	Instrument response of the polarimeter to linearly polarized light. The data points show the variation in relative intensity at each detector with respect to the angle of the half wave plate (HWP) in the polarisation state preparation. The solid lines show the expected intensity modulation for an ideal device for each HWP setting (equation (4.13)), scaled for appropriate detector efficiencies. Error bars are smaller than the point markers. Panel (a) shows the relative intensity at detector 2 without compensation plates. Panels (b) and (c) are taken with compensation for phase shifts. The oscillation in (a) is out of phase and also of lower amplitude compared to the phase corrected behaviour of detector 2 in panel (b). Plots in (c) shows a lower amplitude because light in the reflected arm is not projected on a linear polarization basis. This figure is adapted from figure [65].	54
4.5	Fidelity of reconstructed states to the prepared states. A set of polarization states (\vec{S}_i) equally distributed over the Poincare sphere surface was generated; photons from each of these states were sent to the polarimeter, from which an estimated state (\vec{S}_e) is obtained. The fidelity is given by $\frac{1}{2}(\vec{S}_e \cdot \vec{S}_i)$. It is roughly constant over the Poincare sphere, showing that the polarimeter is an unbiased polarization state estimator. This figure is adapted from figure [65].	57
4.6	The density matrix of a Bell state $ \Psi^+\rangle\langle\Psi^+ $ obtained by linear reconstruction from photon pairs. This figure is adapted from figure [65]. . .	60
5.1	Estimated states plotted on the surface of the Poincaré sphere. The horizontal line represents linearly polarized states. Light crosses mark the prepared polarization state, and a darker cross marks the estimated state. The likelihood region is marked in white. This series of plots can be viewed as a demonstration of how accuracy and uncertainty in state reconstruction changes with increasing number of detected photons. . .	63
5.2	Average trace distances for three different test states, obtained by experiment (points) and by a statistical model (solid lines). The measurements were taken by averaging over 40 experimental runs, each run accumulating 150 detection events. For clarity, only a subset of the experimental data for each state are plotted.	65
5.3	Average trace distance for two test states using only the results of the analytical model. The data points are a subset of the analytical results while the solid lines are fits to the results.	66
5.4	The averaged trace distances (over 5 experimental runs) for a two-photon Bell state, $ \Psi^+\rangle$ and single photon maximally horizontal polarized state, after normalizing over the number of free parameters (3 for a one-photon state, and 15 for the two-photon state).	68

6.1	Schematic of a simple grating based spectrometer. A 1200 line per mm grating is mounted on a motorized rotation stage with a high angular resolution. The first order reflection is collected into a multi-mode fiber that goes to a single photon counter.	70
6.2	Spectra of H and V polarized light in the two different arms of the experimental source described in section 2.3. The spectra of the polarized light is practically indistinguishable, ensuring high quality polarization-correlations. The average FWHM of the spectra are 4.5 nm. There is a residual background count of approximately 300 s^{-1}	71
6.3	The coincidence spectrum of photon pairs. The coincidence spectrum (a) is manifested as a single line obeying energy conservation. A projection spectrum of the coincidence spectrum onto the λ_1 axis is shown in (b).	72
6.4	Change in polarization correlation quality with increasing pump power. The polarization correlation in the $\pm 45^\circ$ basis is reduced dramatically above 40 mW of pump power, suggesting that the collected photon pairs are no longer in a maximally entangled state.	73
6.5	Emergence of a second spectral peak as pump power increases. The emergence of the second peak is correlated to the decrease in the quality of polarization correlations, and is evidence that information leakage into the spectral degree of freedom leads to distinguishable decay processes that degrade the quality of polarization-entanglement. In this case, the second peak in the spectrum arises from a second pump line (351.4 nm) of the Argon ion laser that becomes stronger when the lasing power is increased.	74
6.6	The calculated emission angles of SPDC at 702.2 nm and 702.8 nm under experimental conditions. The emission is strongest in the direction where the phase matching value equals 1. In reference to figure 2.4 (a), this is the emission angle in the plane where $\theta = 0^\circ$	75
6.7	Coincidence spectrum of collected downconversion light from a spectrally “dirty” pump. The second spectral line is just visible at 71 mW. The pump at these power levels have two different wavelengths. The additional wavelength introduces an additional two decay paths. These two new decay paths are spectrally different from the original decay paths at low power.	76
7.1	The visibility plotted against coincidence window time. Increasing the time window leads to more accidental coincidences and a corresponding loss of polarization correlation purity. The solid line is a fitted curve provided by a theoretical model. This figure is adapted from reference [63].	80
7.2	The visibility of polarization correlations plotted against the power supplied to the light bulb. Error bars here are much smaller than the plot markers. This figure is adapted from reference [63].	80

7.3	The noise admixture calculated from the tomographically obtained density matrices. The straight line is the predicted r value for corresponding visibility of the polarization correlation. This figure is adapted from reference [63].	81
7.4	Coincidence spectrum of a Werner state. The amount of background light here was sufficient to create a Werner state with $r = 46\%$. The pump power was increased to allow the spectrum to be collected faster (leading to the two downconversion lines), but the raised background is indicative of the thermal light that has been mixed with the collected photon pairs. This figure is adapted from reference [63].	83
8.1	Schematic of the BB84 protocol for quantum key distribution between two parties (Alice and Bob). Bob must decide randomly between the 0 and 1 bits, as well as the polarization basis in which to encode the bit. Alice must choose randomly the measurement basis. Half the time the transmitted state is not in the measurement basis and such outcomes are discarded. The remaining cases can be used to derive a secure key. Since the polarization state is encoded before transmission, the photons have “an element of reality”.	86
8.2	Schematic for an entanglement-based QKD protocol. Alice and Bob share a stream of polarization-entangled photon pairs. Unlike BB84, they only have to choose the measurement basis. Half the time their choices coincide, in which case a random encryption key can be derived. The remaining cases are discarded. The polarization state of individual photons are not determined until measurement, and are said to lack “an element of reality”.	87
8.3	Orientation of different detector polarizations.	88
8.4	Experimental QKD setup. Polarization-entangled photon pairs are generated via parametric downconversion pumped by a laser diode (LD, PO) in a nonlinear optical crystal (BBO) with walk-off compensation (WP, CC) into single mode optical fibers (SMF). A free-space optical channel for one detector set (Bob) is realized using small telescopes on both sides (ST, RT) with some spatial and spectral filtering (PH, F). Both parties perform polarization measurements in bases randomly chosen by beam splitters (B1-B3), and defined by properly oriented wave plates (H1-H3) in front of polarizing beam splitters (PBS) and photon counting detectors. Photo events are registered separately with time stamp units (TU) connected to two personal computers (PC) linked via a classical channel.	90

8.5	Compact source of entangled photon pairs. This was the diode-pumped source that supplied entangled photon pairs for the QKD demonstration. The pump beam profile is corrected in the lower deck (using anamorphic prisms) and then sent to the SPDC crystal in the upper deck. To restrict footprint of the source further, the downconverted light is reflected into the compensation optics and single mode fiber couplers. The apparatus was mounted on a breadboard drilled with holes that are spaced 1 inch apart. This source was first built by Antia Lamas-Linares and Loh Huan Qian.	92
8.6	Coincidence spectrum of collected photon pairs from the diode pumped source. The spectra were measured after the photon pairs had passed through horizontal (H) and vertical (V) polarization filters. The measurements reveal that the polarization of the photon pairs may be distinguished from their spectra. These measurements were carried out by Loh Huan Qian.	93
8.7	Experimental results in a key distribution experiment implementing an E91 protocol. The experiment ran for 8 hours until sunrise, when excessive background light caused too many accidental coincidences to be detected. In panel 2, the abbreviations EC and PA stand for Error Correction and Privacy Amplification respectively.	95
9.1	Dependency of the combined correlation parameters $L(\varphi)$ as a function of the separation angle φ for the quantum mechanical prediction for a pure singlet state, and bounds for non-local variable models assuming an averaging over various numbers of directions N . This figure is adapted from reference [48].	101
9.2	Experimental setup to test Leggett's Inequality. Polarization-entangled photon pairs are generated in β -barium-borate (BBO) by parametric downconversion of light from an Ar ion pump laser (PL). After walk-off compensation ($\lambda/2$, CC), down-converted light is collected behind interference filters (IF) into birefringence-compensated (FPC) single mode optical fibers (SMF). Polarization measurements are carried out with a combination of a quarter wave plate ($\lambda/4$) and polarization filters (PF) in front of photon counting detectors $D_{1,2}$. The measurement basis for each arm (1,2) is chosen by rotation of the wave plate and polarizing filter by angles $\alpha_{1,2}, \beta_{1,2}$ accordingly. This figure is adapted from reference [48].	102
9.3	Experimental results for the observed correlation parameters L_N (dots), the quantum mechanical prediction for a pure singlet state (curved lines, dashed), and the bounds for the non-local variable models (almost straight lines). In all cases, our experiment exceeds the NLV bounds for appropriate difference angles φ . This figure is adapted from reference [48].	104

-
- A.1 Poincare sphere representation of polarization states. The Poincare sphere is a ball of unit radius. Pure polarization states lie on the sphere's surface while mixed polarization states reside within the sphere. 116

Chapter 1

Quantum Mechanics and Communication

Advances in miniaturisation are beginning to allow the fabrication and manipulation of physical systems which exhibit quantum effects. In the context of information technology, this means that quantum systems can act as the physical carriers of information. As a consequence, standard information theory (which is based on the properties of classical objects) will need to be revised in order to consider any additional power and functionality that quantum systems can bring to computing and information processing [2, 3, 4, 5, 6, 7].

In order to appreciate the different effects of quantum and classical systems on information theory, it is best to start by considering how information is encoded. In the standard treatment of information theory, information is encoded in discrete storage units called bits. The simplest system of encoding information is to use Boolean logic where a single bit has two possible values: 0 or 1. A classical bit can have only one value; it is either in the state 0 or the state 1. In standard information technology, the bit is realized through a classical object such as a magnetic domain or an ink blot on a piece of paper.

Now, a classical bit can also be encoded with the state of a spin- $\frac{1}{2}$ (or two level) quantum system. This can be done, for example, by identifying 0 with the $|-\frac{1}{2}\rangle$ state and 1 with the $|+\frac{1}{2}\rangle$ state. It is also possible, however, to prepare the quantum system

such that its state is: $\alpha|+\frac{1}{2}\rangle+\beta|-\frac{1}{2}\rangle$, where $|\alpha|^2+|\beta|^2=1$. The *probability amplitudes* α and β are generally complex numbers. Essentially, the quantum system can encode any *superposition* of the 0 and 1 states. The two level quantum system is an implementation of a quantum bit or *qubit* [8]¹. Qubits are the building blocks of quantum information.

The superposition of states that was introduced in the above description of qubits is a quantum phenomenon. Other quantum features that are exhibited by qubits include entanglement, interference and non-clonability². Together, these effects have enabled theoretical proofs showing that qubits can be exploited to enable specific tasks that are either inefficient or impossible under classical information processing³.

A prominent example of quantum information is the development of quantum algorithms (such as the Shor algorithm [12] and the Grover search method [13]) that use quantum systems to obtain an improvement in the efficiency of information processing over classical methods. Another example of quantum information are the use of non-clonability for secure transmission of classical information [14] (quantum key distribution). Also interesting is the exploitation of quantum entanglement in showing how to transfer quantum states between distant locations (quantum teleportation) [15] or to increase communication channel capacity (dense coding) [16].

Public interest in this subject is spurred by the hope for faster information processing and better security in data transmission. Consider the Shor algorithm which uses qubits to carry out prime number factorization more efficiently than any known classical method. The ramification of the Shor algorithm was that the security of commonly used encryption schemes relying on the intractability of prime number factorization (e.g. RSA [17]) would be put into jeopardy by advanced quantum computers.

Apart from applications, this emerging field of study has provided a boost to research into fundamental areas of quantum physics. For example, it is very intriguing to consider

¹Quantum systems can also implement multi-level schemes of coding information. For example, ternary systems are encoded via three level quantum systems called qutrits. N-level encoding schemes are implemented via quNits. As with relatively new inventions the shorthand for quantum bit has sometimes been “controversially” written as qbit [9, 10]. This thesis adopts the more popular qubit terminology.

²The role these effects play is described in [2]. Non-clonability and entanglement are described in sections 1.1 and 1.2 respectively.

³Not all problems faced by classical information can be solved with quantum methods. Although the limits of quantum information are not yet known, computer scientists have suggested that a large class of problems are intractable for both classical and quantum information processing [11].

that quantum entanglement, which arises from the tension between quantum mechanics and special relativity, can be used to prove security of data transmission [18, 19].

The formal name for the study of information science with quantum mechanical properties is Quantum Information Theory, and it may be divided into two rough areas: Quantum Computation and Quantum Communication. Quantum communication is devoted primarily to studying the distribution of quantum states between spatially separated parties, and the potential applications (like key distribution, teleportation and dense coding) [6]. This thesis concentrates on the experimental aspects of generating optical qubit states for quantum communication.

1.1 The start of quantum communication

Quantum communication started in the 1970s when Stephen Wiesner first mentioned the use of quantum mechanics in communication security (although he published it only in 1983 [20]). One of his original formulations was to use states of spin- $\frac{1}{2}$ particles to encode unforgeable serial numbers in money. The subject, however, only rose to prominence when Bennett and Brassard discussed their protocol for distributing secret keys for encryption and decryption in 1984 [14]. Their protocol is called BB84, and it solved the following problem: How do two spatially separated parties agree rapidly on a shared random key in complete secrecy?

The insight provided by Bennett and Brassard was to show that the random bits (0s and 1s) making up the key could be encoded in the polarization state of single photons. Thus, if the polarization states of the single photon pulses are prepared and measured randomly in two conjugate bases, these pulses could be sent between two parties who will quickly build up a shared key that is completely random.

The secrecy of the key is derived from the no-cloning theorem [21, 22] and the fact that individual photons are single quanta. The no-cloning theorem says that it is impossible to perfectly copy an unknown quantum state. This can be viewed as a consequence of the Heisenberg Uncertainty Principle which states the impossibility of simultaneously measuring, with complete precision, the state of an unknown quantum system in two conjugate bases. By measuring the photon state in one basis, information

on its state in the conjugate basis becomes increasingly uncertain (lost). Hence, any attempt to extract information from a single photon would result in changes to its polarization state. Such eavesdropping attempts are revealed as errors in the final key. Bennett and Brassard had provided the first example of a quantum key distribution (QKD) protocol.

Due to a lack of single photon sources, initial demonstrations of BB84 were carried out with weak coherent pulses [23]. These are laser light pulses that have been attenuated to a very low intensity level such that the probability of finding a single photon in each pulse is very small. The corresponding probability of finding two or more photons is even smaller; however it is not zero. Surprisingly, this small probability was sufficient to put into doubt the security of the original experimental demonstrations [24, 25, 26]. These doubts were put to rest when Norbert Lütkenhaus provided a security proof for BB84 with weak coherent pulses in 2000 [27]⁴. Since then, various commercial QKD devices based on weak coherent pulses have appeared on the market⁵, and QKD remains the most mature quantum information application.

At the same time, QKD continued to hold the attention of physicists (as well as computer scientists and mathematicians) with a new protocol suggested by Artur Ekert in 1991 [18]. This protocol, called E91, pushed the “quantum” character of QKD further by proposing that aspiring quantum cryptographers exploit the property of quantum mechanics known as entanglement⁶.

1.2 Qubit entanglement, very briefly

Entanglement is a feature of quantum mechanics in which the correlations shared between separate systems cannot be obtained from the states of the individual systems. Effectively, these separate systems must be treated as the components of a larger object. A precise mathematical description for the state of such a joint system can be written

⁴Single photon sources have since become less crucial for QKD since a key distribution protocol based on *decoy states* was developed in 2003 [28].

⁵In 2001, a company called idQuantique started offering commercial QKD devices; it has at least one serious competitor (MagiQ Technologies) at the moment.

⁶For a discussion of the differences between the E91 and BB84 protocols see chapter 8.

(such as equations (2.3) and (1.1)), and Erwin Schrödinger was the first to call the joint state an *entangled state* [29]. The simplest system that can be entangled is a bi-partite system. Entangled bi-partite systems are commonly observed in atomic physics, e.g. when treating the spins of two electrons⁷.

A consequence of being in an entangled state is that there are correlations between observable physical properties of the sub-systems. For example, it is possible to prepare two electrons in a joint quantum state such that the electrons are always found to be both in the spin-up state, or both in the spin-down state, *for all measurement basis*. The entangled state $|\Psi\rangle$ of such an electron pair can be written as

$$\Psi = \frac{1}{\sqrt{2}} (|+\frac{1}{2}, +\frac{1}{2}\rangle - |-\frac{1}{2}, -\frac{1}{2}\rangle) \quad (1.1)$$

One way to think of this is that some composite systems, like the electron pair, can provide the same random answer when asked the same question. In the context of electron pairs, asking a question means putting an individual electron through a Stern-Gerlach apparatus⁸. The question can vary (i.e. the measurement basis, or orientation of the Stern-Gerlach apparatus can rotate), and the individual answer (measurement outcome) is always random: the individual electron is randomly spin-up or spin-down. The feature of entanglement is that when the question is the same for both electrons (same orientation of Stern-Gerlach apparatus), they always give the same answer (both spin-up or both spin-down)⁹. The difference in the measurement outcome for classical and entangled systems is illustrated in figures 1.1 and 1.2.

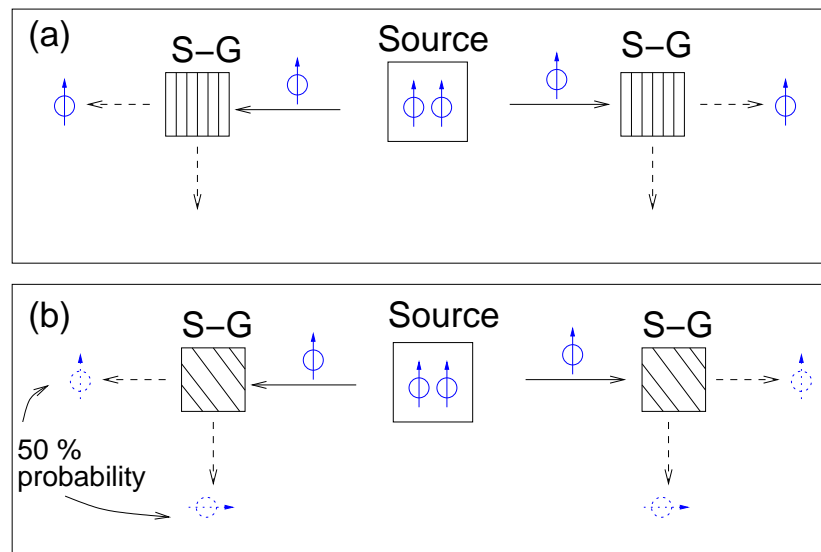
An insistence on finding a cause-and-effect mechanism for the above results leads to the following conclusion: the measurement outcome on one electron is influencing the state of the other electron instantaneously. The realisation that the superluminal mechanism must hold even when the electrons are spatially separated made the phenomenon very controversial (and popular), because it seemed to contradict relativity¹⁰.

⁷Such examples are readily found in introductory texts such as in section 9.4 of the textbook by Eisberg and Resnick [30]. They describe a state for two electrons (the singlet state) that is actually entangled, although they did not elaborate on its non-classical features.

⁸For a description of the Stern-Gerlach experiment, see the introduction to J. J. Sakurai's textbook [31].

⁹This example is adapted from the review article by Gisin and Thew [6].

¹⁰Special relativity forbids instantaneous influences between distant locations, and more generally,



Classical Bi-partite System

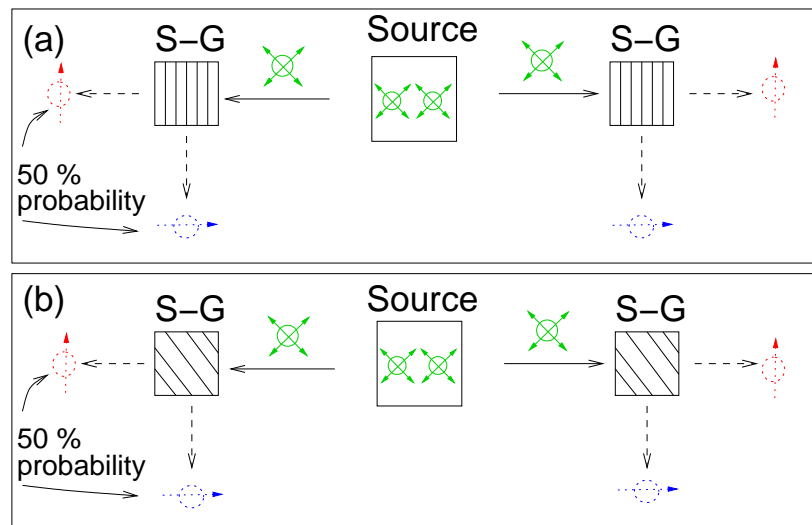
Figure 1.1: Simple representation of a Stern-Gerlach experiment using an electron pair in a classical state. Consider a source that prepares electron pairs only in the spin-up direction, and where the individual electrons are interrogated by separate Stern-Gerlach apparatus (S-G). In panel (a) the Stern-Gerlach devices on both sides are in the same basis as the prepared spins. The measurement outcome for the individual electrons can be predicted with certainty (represented by a solid outline for the electron) and are correlated. In panel (b), the Stern-Gerlach apparatus measures a conjugate basis and the individual measurement outcomes and the inter-electron correlations are random (dashed lines).

This tension between quantum mechanics and relativity was discussed extensively by the trio of Einstein, Podolsky and Rosen (EPR)¹¹ [32]. The EPR trio concluded that quantum mechanics must be incomplete (in a classical sense), and proposed that additional *local* parameters are necessary for describing the state of physical systems. These parameters would exert an influence that provided the illusion of instantaneous effects. In principle, these parameters can be unknown (hidden), and a model that described physical states with these parameters is a Local Hidden Variable (LHV) model.

Despite the efforts of EPR, entanglement was not widely investigated for several decades although various theories (in particular by David Bohm [33] and Hugh Everett [34]) were put forward to address the thorny philosophical issues that arose from the EPR paradox. Widespread interest in entanglement only began after John Bell derived

prohibits the propagation of information at superluminal speeds.

¹¹Historically, the EPR paper appeared first. Schrödinger invented the term “quantum entanglement” (and his famous Schrödinger cat thought experiment) in a subsequent paper that was meant to discuss the EPR article.



Entangled Bi-partite System

Figure 1.2: Simple representation of a Stern-Gerlach experiment using an entangled electron pair. Consider a source that prepares an entangled electron pair, and where the individual electrons are interrogated by separate Stern-Gerlach apparatus (S-G). For any measurement basis (panel (a)) the measurement outcome for the electron pair is always both spin-up or both spin-down (i.e same color), but occur randomly. This is true even if the Stern-Gerlach apparatus have been rotated to a conjugate basis as in panel (b).

his famous theorem [35]. Bell's theorem was important because it showed explicitly that a physical theory based on local parameters could not reproduce all the predictions of quantum mechanics¹². By working with probabilities, Bell showed that the observable correlations between two systems described only by local parameters could never exceed a certain bound. This bound was known as Bell's inequality and suggested how experimental tests for the validity of models using local parameters might be carried out.

Experimental tests [37, 38] were carried out in the 70s and 80s with modified Bell inequalities, such as the Clauser-Horne-Shimony-Holt (CHSH) inequality [39]. In particular, the experiment by Alain Aspect and his co-workers [40] is accepted as showing that observed physical correlations exceed Bell's inequality, conclusively showing that quantum correlations between distant systems are an observable fact of nature. However, this does not mean quantum mechanics and relativity are in conflict; it has been shown that EPR's concept of locality is a conjunction of special relativity plus classical

¹²This is discussed extensively by Bell in his book [36].

assumptions about predictability of systems [41]. It is the additional classical assumptions that are not satisfied.

It should be kept in mind, however, that all current experimental tests of Bell's inequalities take place with imperfect experimental devices [42]. These imperfections allow for loopholes in any argument about the lack of local parameters. For example, experimental equipment often have low detection efficiency (detection loophole) [43], or are not placed sufficiently far apart (locality loophole). The technical loopholes have been covered in separate tests. For example, see the work of Rowe *et al.* [44] on the detection loophole, and the separate publications by Weihs *et al.* [45] and Tittel *et al.* [46] concerning the locality loophole. No experiment has yet been performed which is completely loophole-free. The best that can be said currently is that the loopholes are generally covered by reasonable assumptions that seem valid when the devices are under careful control¹³.

It is assumed, however, that the problem of loopholes can be resolved with better technology and it is widely accepted that quantum mechanics is able to explain a larger body of observed facts compared to classical theories based on local parameters (and even some theories using non-local parameters! [47, 48]). A modern understanding of quantum correlations is that it is simply a description of physical systems that are naturally counterintuitive [49]. Furthermore, entanglement is beginning to be viewed as a “resource” to be exploited in communications technology, because they can be used to distribute quantum correlations over wide distances. Apart from the notable exception of BB84, virtually all quantum communication requires entangled quantum states [6]. In fact, Bell's inequalities now have relevance for technology since a violation of a Bell inequality is the only way to distinguish between entangled and unentangled quantum states without having to know the dimensions of the relevant Hilbert space [50].

¹³For example, the “fair-sampling” assumption is used to deal with the detection loophole. The loophole arises because the experimental equipment have less than perfect detection efficiency. Hence, only a subset of systems from an ensemble can be detected. Fair sampling assumes that the detected systems are representative of the entire ensemble.

1.3 Entanglement and quantum communication

The most basic entangled quantum system is a pair of qubits. For quantum communication, qubits are most easily implemented with single photons [7], primarily because of speedy transmission. Furthermore, a photonic qubit can be conveniently encoded in any of several degrees of freedom. A natural choice is polarization, and polarization-entangled photon pairs are one of the most commonly implemented entangled photon systems. Polarization-entangled photon pairs have been used in experimental demonstrations of various quantum communication protocols like dense coding [51], teleportation [52, 53] and quantum key distribution [54]. A good review of the subject of entanglement based quantum communication is provided by Gisin and Thew [6].

One of the grand challenges in applied quantum communication is to build a robust and wide-spread communication network based on quantum protocols. Such a network will require a bright source of high quality entangled photon pairs. Furthermore, in an extensive quantum communication system there will be a need for signal repeaters and current proposals call for such devices to be based on atom-like systems [55, 56]. This means any entangled light will have to be in a sufficiently narrow spectrum (tens of MHz) to interact with atomic memories and repeaters¹⁴.

Future sources of entangled photon pairs will need to meet three criteria: high brightness (large rate of photon pairs), high quality of entanglement (large violation of a Bell inequality), and narrow bandwidths (large coherence times). This can be visualized by the Venn diagram in figure 1.3. Currently, no source of entangled light is able to meet all three criteria. For example, parametric downconverters based on nonlinear optical crystals [61, 62] produce high quality entangled photons but have very broad bandwidth (about 1 THz), and so their spectral brightness (brightness per unit of frequency) is quite low. A summary of contemporary photon pair sources is provided by table 2.1 in the next chapter.

To be able to supply entangled light for future quantum information applications, the first step is to study contemporary photon pair sources and understand the limits

¹⁴Many experimental approaches are being investigated in this subject, such as the use of atomic vapors [57] and atomic ensembles [58, 59, 60].

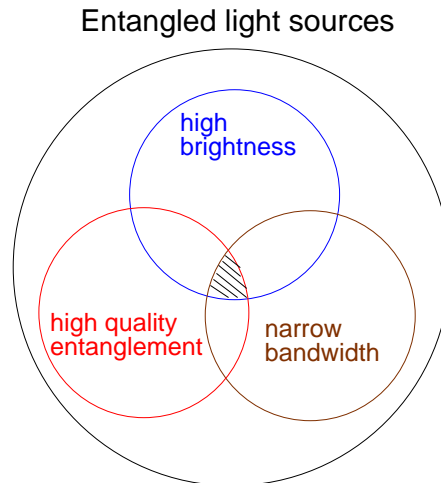


Figure 1.3: Criteria for evaluating entangled light sources. Three ways of evaluating entangled light sources are to look at their brightness, the quality of their entanglement and the narrowness of the spectral bandwidth of the generated light. An ideal light source will be rated highly in all three areas (and should lie in the shaded region in the centre of the figure). Sometimes brightness and bandwidth are considered together as ‘spectral brightness’.

to their spectral brightness. Also techniques must be developed to characterize the states of the generated light. At the same time, it is possible to experimentally validate quantum communication proposals and carry out further investigations into the nature of entanglement.

The above issues are addressed within this thesis which is roughly divided into two parts - building the source and applications for photon pairs generated by the source. The bulk of the thesis concerns the implementation of a source of polarization-entangled photon pairs (based on nonlinear optical crystals), and the characterization of the generated photon states (chapters 2 to 6). Chapter 2 provides a description of the source, while chapter 3 describes a physical model giving absolute emission rates from the source. Techniques for characterizing the correlations in the polarization and spectral degrees of freedom are described in chapters 4, 5 and 6. These techniques will reveal that the photon pairs produced by the experimental source are of a very high quality.

The second part of the thesis, focusses on experiments that use these highly entangled photon pairs. Chapter 7, describes how the photon pairs are used to implement idealized states known as Werner states. A field demonstration of QKD was also per-

formed with a miniaturized photon pairs source, and this experiment is described in chapter 8. We return to the lab with chapter 9 which describes a project to provide experimental falsification of a class of non-local variable models via the Leggett inequality.

The subject matter of this thesis depends heavily on a consistent description of polarization states. Such polarization states are most conveniently expressed in a vector notation, and one may choose between the Stokes notation (for all polarization states), or Jones notation (for pure polarization states only). A brief introduction to the vector notation used in this thesis is provided in Appendix A.

Many of the results reported in this thesis will have been reported already in several published papers [63, 64, 65, 48, 66] (see Appendix C). The basic layout of this manuscript is such that the material for each chapter is often drawn from a published paper. The text has been altered so that the material can be read smoothly from beginning to end, and also for consistency of notation and references.

Chapter 2

A Polarization-Entangled Photon Pair Source

Quantum communication uses the states of quantum systems that have been distributed between distant locations, and virtually all quantum protocols (apart from BB84) require entangled quantum states. The simplest and most commonly used entangled state is composed of two qubits. Qubits are described by a two dimensional Hilbert space, and are easily realized by the states of spin- $\frac{1}{2}$ systems such as the spin of electrons.

For the purposes of communication, it is natural to use the fastest travelling qubits and these are states encoded using photons (which are single light quanta). Apart from speed of transmission, other advantages of using photons exist. For instance, in free space, photons are only weakly coupled to the environment and so can travel long distances without their polarization state being lost (i.e. decohering).

Another advantage of using photonic qubits is that the qubit state is not restricted to the polarization degree of freedom. For example, there has been experimental implementations of entangled states based on time-bin qubits [67, 68] (this is based on the concept of time-energy entanglement first suggested by J. Franson [69]). Time-bin qubits are especially suited for quantum communication over optical fibers, and this has been demonstrated for fiber-based QKD [70, 71] and quantum teleportation [72] (polarization based qubits would decohere rapidly in such an environment). However,

polarization qubit states are easier to manipulate and detect¹. The quantum communication projects considered in this thesis are also free-space applications² and so my focus will be on qubit states realized via photon polarization.

This chapter is divided into four main parts. In the first section, we briefly review the different physical processes that can be used to build sources of correlated (and entangled) photon pairs³. In the second section, an experimental implementation of a source of high quality polarization-entangled photon pairs is provided⁴. The third section gives a method to quantify the entanglement. The chapter ends with a brief remark on the brightness and quality of the implemented source and compares it to other sources that have been reported in the literature.

2.1 Sources of polarization-entangled photon pairs

The first experimental sources of polarization-entangled photon pairs were implemented with atomic-cascade decays in order to violate a Bell inequality at distant points [37, 38, 40]. Beginning in 1987 quantum correlations were also observed between photon pairs that were emitted from nonlinear crystals that are pumped with with intense coherent light [74, 75]. In fact, nonlinear optics (achieved using bulk crystals or atomic vapors) is now the basis for most entangled photon sources.

The strongest physical process leading to emission of photon pairs from a nonlinear crystal is called Spontaneous Parametric Down Conversion (SPDC)⁵. It is a three-wave mixing process that utilizes the lowest order nonlinear susceptibility in birefringent crystals. This susceptibility is labelled as $\chi^{(2)}$ and its mathematical representation is a tensor of rank 2⁶ The phenomenon was first predicted in 1961 by Louisell and his

¹This is because the manipulation of polarization qubits requires the same equipment (e.g. waveplates) and methods as in classical optics, and many of these techniques have been well understood since at least the 19th century. A historical development of optics is provided in many standart texts such as the one by E. Hecht [73].

²Chapter 8 describes a free-space QKD experiment.

³The first step to obtaining entangled photons is to find a physical process that gives rise to photon correlations.

⁴This includes equations that describe the entangled state.

⁵Early literature on SPDC referred to the process by many names, such as parametric fluorescence, or parametric scattering.

⁶A full description is given in chapter 2 of the classic text by Y. R. Shen [76].

co-workers [77]. In general, SPDC is any mechanism that causes a single parent photon to decay into lower energy daughter photons. In this thesis, however, SPDC will be identified with the $\chi^{(2)}$ process.

The theory of SPDC was formally established by Kleinman [78] and independently by Klyshko (whose work was compiled into a textbook [79]). A modern quantum mechanical derivation was provided by Hong and Mandel in 1985 [80].

The essential feature of SPDC is that a single pump photon passing through a uniaxial nonlinear optical material can decay into two daughter photons obeying energy and momentum conservation⁷. These daughter photons will be correlated in momentum, energy and time. These two downconverted photons may be of the same polarization (type I downconversion) or of orthogonal polarization (type II downconversion). The standard technique for detecting photon pairs is the timing coincidence method that was first demonstrated in 1970 by Burnham and Weinberg [81]. Generally, the photon pairs display only classical correlations; special steps need to be taken to ensure that they become entangled and this is described further in the next section.

Over the last two decades the design of SPDC sources has become more refined resulting in less complicated setups. For instance, the original SPDC-based sources [74, 75, 82, 83, 84] needed polarization independent 50:50 beam splitters in order to convert correlated photon pairs into entangled states. The need for such beam splitters was removed with new source designs by Kwiat and his co-workers in 1995 [61] and 1999 [62]. In particular, the design introduced in 1995 utilised the concept of noncollinear type II phase matching, where photon pairs were emitted from a single downconversion crystal in an entangled polarization state.

The similarity shared by all the bulk crystal sources above was that the conditions for SPDC were satisfied through a technique called critical phase matching (CPM). With this technique the emission angle of a particular wavelength is selected by tuning the angle between the optical axis of the crystal and the pump beam. In most of such cases the experimentalist can only access smaller elements of the $\chi^{(2)}$ tensor, and pair generation also suffers from a reduced interaction length because of walk-off effects. The

⁷The probability of a pump photon decaying is on the order of 10^{-12} for every mm of nonlinear crystal material; see section 3.3.

overall result is a reduced rate of photon pair production.

The conditions for SPDC to take place can also be achieved through a technique called quasi-phase matching (QPM). Quasi-phase matching was first described by Armstrong *et al.* [85] and independently by Franken and Ward [86]. In QPM, frequency conversion is enhanced via some kind of periodicity in the nonlinear material. This periodicity can be introduced by alternating the orientation of the crystal optical axis between two directions. Such crystals are known as periodically poled crystals. Frequency conversion with QPM has two advantages over methods using unpoled crystals. First, quasi-phase matching gives the experimentalist access to larger elements of the $\chi^{(2)}$ tensor. The other advantage is that the interaction length can be increased as walk-off effects are minimized. The primary application of QPM is in second harmonic generation [87], which provided the main motivation for research on the production of crystals with a periodic poling structure. However, periodically poled materials are being increasingly used for SPDC as well.

The first sources exploiting quasi-phase matching to obtain entangled photon pairs were implemented in 2001 [88, 89]. Engineering difficulties at first restricted periodic poling to small waveguide structures. Bulk periodically poled crystals have since become available, leading to simpler alignment criteria and also higher quality entangled photon pairs [90, 91, 92, 93]. All these sources display much better spectral brightness compared to sources based on angle phase matching. These sources, however, are sensitive to the crystal poling period, and thus to temperature fluctuations which must be controlled during an experiment. Historically, they have suffered from being unable to compete with unpoled crystal sources when it comes to entanglement quality. It was only in 2007, that a periodically poled crystal source (built by Fedrizzi *et al.* [94]) had been able to achieve a competitive quality of entanglement⁸.

Another process known as Four-Wave Mixing (FWM) has been demonstrated to produce entangled photon pairs [97]. This is a process that utilizes the $\chi^{(3)}$ susceptibility. Although FWM experiments had been carried out before to demonstrate quantum

⁸In an interesting twist, it has been shown that confining SPDC to waveguide structures can enhance the rate of photon pair production [95, 96], and periodically poled waveguides are likely to return to the centre of attention in future research on entangled light sources.

correlations (as in squeezing experiments from atomic vapors [98]), the modern experiments are geared towards generating telecom wavelength photon pairs. In these modern schemes FWM generally takes place inside a micro-structure (photonic) fiber, where two pump photons are parametrically scattered into two other photons of different energies, obeying energy conservation. In a recent experiment, Fan *et al.* [99] reported a measured pair generation rate of 7000 pairs s^{-1} using only $300\mu W$ of pump power in a 1.8m spool of fiber that was at room temperature. Four-Wave Mixing appears to be a promising method for correlated photon pair generation.

From the above discussion it will be seen that there are several alternatives for obtaining entangled photon pairs from nonlinear optical methods, even when considering SPDC based sources alone. When the research work described in this thesis began in 2004, the choice was made to study the brightest and highest quality entangled photon pair sources in existence and at the time this was the 2001 design by Kurtsiefer *et al.* [100]. This was a modification of Paul Kwiat's 1995 source where the spectral bandwidth of the entangled photon pairs was optimized by manipulating the coupling of photon pairs into single mode fibers.

2.2 The experimental implementation

2.2.1 Basic principles of SPDC

SPDC is a three wave mixing process where a pump photon passing through a nonlinear optical crystal has the probability of being converted into two daughter photons. Here it is assumed that the three mixing waves are plane waves (in the next chapter the mixing waves will be treated as beams). In type II downconversion, the daughter photons may be identified according to their polarization with respect to the crystal axes and labeled as ordinary or extraordinary. However, the choice is made to follow convention in nonlinear optics and label the downconverted photons as the signal photon (index s) and the idler photon (index i). The idler photon is identified as extraordinary polarized, and as having the same polarization as the pump (index p). In the laboratory frame of reference the extraordinary polarization is the same as the vertical polarization state $|V\rangle$ (Appendix A).

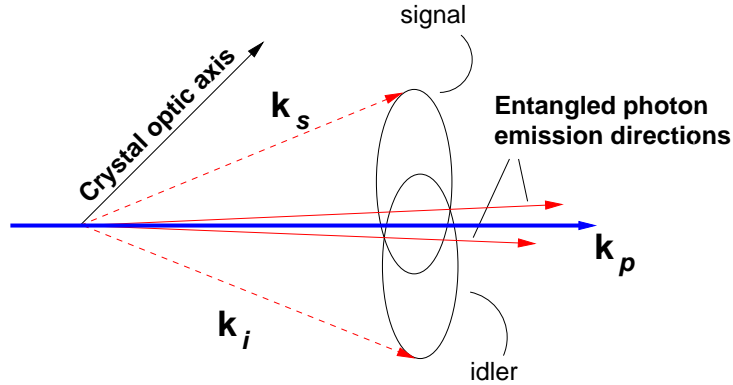


Figure 2.1: Spontaneous parametric downconversion for fixed signal and idler wavelengths under type II phase matching conditions. The emission may be collinear with the pump field direction, or noncollinear (shown in this diagram). Here, the cones overlap at two points. Degenerate twin photons that are emitted in these overlap regions are indistinguishable apart from their polarization states, and will be polarization-entangled. This figure is adapted from reference [61].

The frequencies of the three fields are written as $\omega_{p,s,i}$. In the same way, the wave vector of the fields can be expressed as $\mathbf{k}_{p,s,i}$. The energy and momentum conservation rules are:

$$\omega_p = \omega_s + \omega_i \quad (2.1)$$

$$\mathbf{k}_p = \mathbf{k}_s + \mathbf{k}_i \quad (2.2)$$

For type II downconversion the degenerate twin photons are emitted in two cones. One cone is ordinary polarized while the other is extraordinary polarized. The opening angle of each cone depends on the angle that the pump field makes with the crystal optical axis; this angle is labeled as θ_p . At one value of θ_p , degenerate collinear emission is obtained. This occurs when the two cones overlap exactly at one point (i.e. in the pump beam direction). In this direction, the products of a single pump photon decay are emitted in the direction of the parent photon.

Further increase of θ_p causes the cones to move towards each other and they will intersect at two points centred around the pump beam. Degenerate emission at these two intersection points is essentially indistinguishable except for the polarization states.

Thus, two possible decay paths for the pump photon are now indistinguishable at the intersection points. This is the reason why the photon pairs are generated in a polarization-entangled state and is the most important point about Kwiat's 1995 design. A schematic of the source emission profile is shown in figure 2.1.

The polarization-entangled state emitted directly from the crystal in these two directions may be written as follows:

$$|\psi\rangle = \frac{1}{\sqrt{2}} \left(|H_1, V_2\rangle + e^{i\phi} |V_1, H_2\rangle \right) \quad (2.3)$$

The subscripts 1 and 2 are labels for the collection arms in the experiment (figure 2.2). Crystal birefringence introduces a relative phase ϕ , between the ordinary and extraordinary polarized light. Global phases may be ignored. In section 2.3 I will describe the correlations existing in polarization-entangled states in greater detail.

In addition to the relative phase ϕ , crystal birefringence also adds transverse and longitudinal walk-off. Longitudinal walk-off refers to the fact that the ordinary and extraordinary polarized light have different velocities inside the crystal, and can become distinguishable in principle because of the relative delay that is introduced by travelling through the crystal. Transverse walk-off refers to the fact that the ordinary and extraordinary light have different propagation directions and become separated by some distance after crossing the downconversion crystal. It is possible to completely correct for longitudinal walk-off and at the same time set the value of the relative phase ϕ by using additional birefringent crystals that are half the length of the pump crystal⁹.

After correcting for walk-offs, it is possible to obtain any of the four maximally entangled Bell-states from the source by having additional half-wave and quarter-wave plates in each of the arms of the source:

$$|\psi^\pm\rangle = \frac{1}{\sqrt{2}} (|H_1, V_2\rangle \pm |V_1, H_2\rangle) \quad (2.4)$$

$$|\phi^\pm\rangle = \frac{1}{\sqrt{2}} (|H_1, H_2\rangle \pm |V_1, V_2\rangle) \quad (2.5)$$

⁹These additional crystals are called compensators, and a comprehensive explanation is provided by Rubin *et al.* in reference [101]. At the same time, the compensators also correct partially for transverse walk-off.

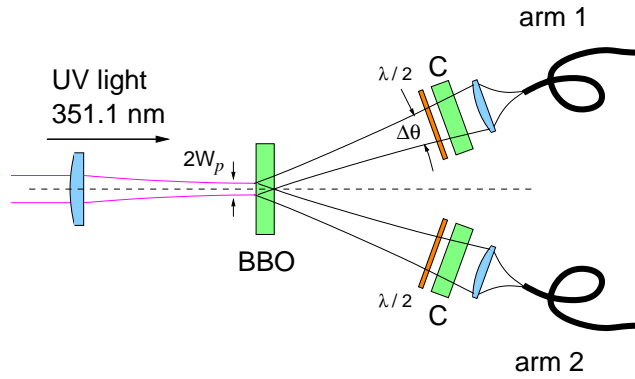


Figure 2.2: A fiber-coupled polarization-entangled photon pair source. The fiber modes are mapped onto the two intersection points in the SPDC emission. Half-wave plates and compensating crystals perform correction for longitudinal walk-off. The bandwidth of collected light is determined by the acceptance angle $\Delta\theta$ of the fiber modes. This figure is adapted from reference [99].

Photon pairs from the source can then be collected into single mode optical fibers so that the photons can be sent downstream to other optical devices for further manipulation and detection. The basic experimental setup is shown in figure 2.2. The pump beam is 351.1 nm light from an Argon ion laser (Coherent Innova 320C). The downconversion medium was a 2 mm thick β -Barium Borate (BBO) crystal that was cut so that the angle between its optical axis and crystal face was at 49.7° . Degenerate SPDC light at 702.2 nm emitted from the intersection points is coupled into single mode fibers that guide the light to further optical devices. The waist of the collection modes was designed to be 82 microns, and the pump waist was matched to this value. Single photons were detected by passively quenched silicon avalanche photo-diodes. The observed rate of pairs that are collected into the fibers was observed to be approximately $800 \text{ pairs s}^{-1} \text{ mW}^{-1}$.

2.2.2 Optimizing for collection bandwidth

One of the optimization steps when building a fiber-coupled SPDC source is to fix the bandwidth of collected light, following the optimization procedure in [100]. The first step in the optimization procedure is to approximate the collection mode of the single mode fiber with a Gaussian beam (figure 2.3). Every collection mode is defined by a beam waist, W . The waist, wavelength λ and divergence angle θ_D of the collection mode is related through the following expression: $W = \lambda/\pi\theta_D$.

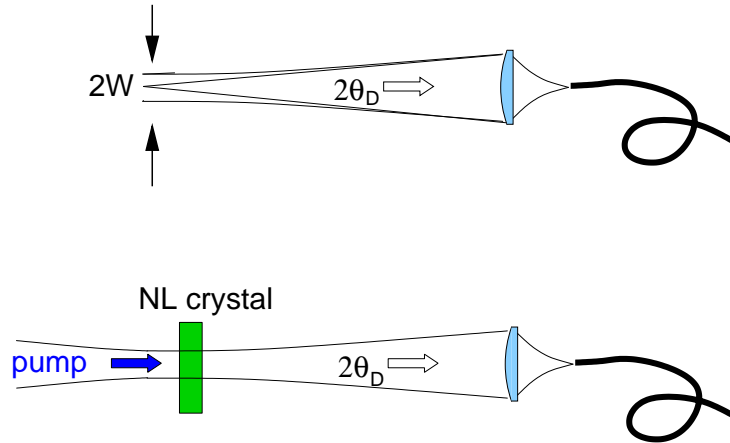


Figure 2.3: Bandwidth optimization with single mode fiber collection. The collection mode waist, W , and angular divergence, θ_D , is determined by the desired bandwidth of SPDC light that is to be selected. The pump is restricted to areas of the crystal that are observed by the fibers and this means matching it to the collection mode.

The next step is to consider the emission angle for different frequencies of light. This is obtained by assuming perfect phase matching of the interacting plane waves. For BBO crystals, pumped with 351.1 nm, the emission angle for wavelength in the neighborhood of the degenerate emission is given in figure 2.4. The rate of change of emission angle with respect to wavelength, $|d\theta/d\lambda|$, is found to be $0.055^\circ \text{ nm}^{-1}$ [100].

The intensity distribution of a Gaussian profile is

$$I(\theta) \approx \exp(-2\theta^2/\theta_D^2).$$

It is now possible to relate the spectral bandwidth of collected light to the characteristics of the collection mode. For example, if the aim is to collect light whose spectral bandwidth has a Full Width at Half-Maximum (FWHM) of 4 nm, the expected divergence angle is given by

$$\theta_D \approx \Delta\lambda_{\text{FWHM}}/\sqrt{2\ln 2} \times |d\theta/d\lambda| = 0.186^\circ.$$

This would be the divergence angle that is used in the experiment, if all conditions satisfied perfect phase matching. These conditions, however, are not met in the experiment as there are various effects that act to broaden the spectra of the collected light. One of this is the effect of transverse walk-offs, and the presence of some wave-front

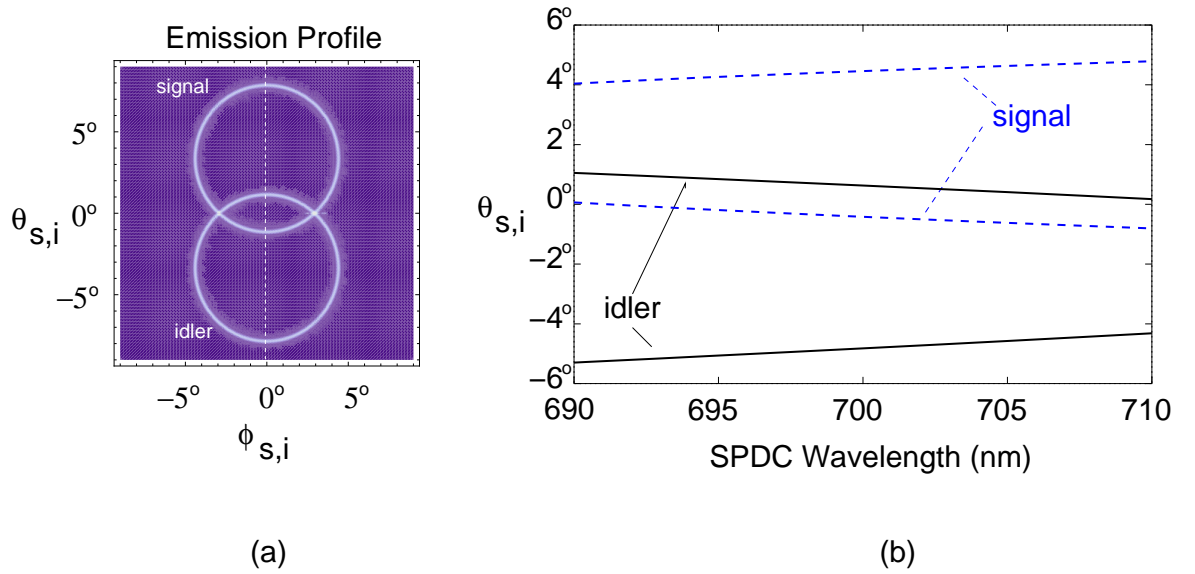


Figure 2.4: The emission profile of degenerate SPDC light at 702.2 nm. The emission profile calculated by assuming perfect phase matching and a plane wave pump beam is presented in (a). The emission angle for different SPDC wavelengths in the plane $\phi_{s,i} = 0^\circ$ is shown in (b). The slope of the emission angle $|d\theta/d\lambda|$ at 702.2 nm is estimated to be $0.055^\circ \text{ nm}^{-1}$.

curvature in our pump beam¹⁰. Another effect is due to the non-collinear geometry that is used¹¹. To compensate for these, and other effects, the experiment was designed with a smaller divergence angle instead. The final selected angle was $\theta_D = 0.16^\circ$. This corresponds to a beam waist of 82 microns which in the ideal case leads to collected light whose spectral FWHM is 3.4 nm. However, this value must be augmented by a correction factor due to the non-collinear geometry that is implemented in the setup. This correction factor is determined in Appendix C and it is found there that the FWHM is broadened by 13% compared to the ideal case. After correcting for this, the final expected spectral bandwidth is approximately 4 nm.

The pump mode is restricted to illuminate only parts of the crystal from which light is collected, and hence is matched to the collection mode¹². It is necessary to keep the Rayleigh range of the pump and collection modes to be at least the crystal length. Only then will the approximation of plane waves (and a lack of wavefront curvature) from

¹⁰For a drastic example of how spectral bandwidth can be affected by wave-front curvature see [102].

¹¹This spectral broadening effect of non-collinear phase matching is described in section 3.2.3 and illustrated in figure 3.2.

¹²This is actually not the optimal pump mode. For maximum count rate, the pump beam waist should actually be about 71% of the the collection waist. This is described in section 3.2.6.

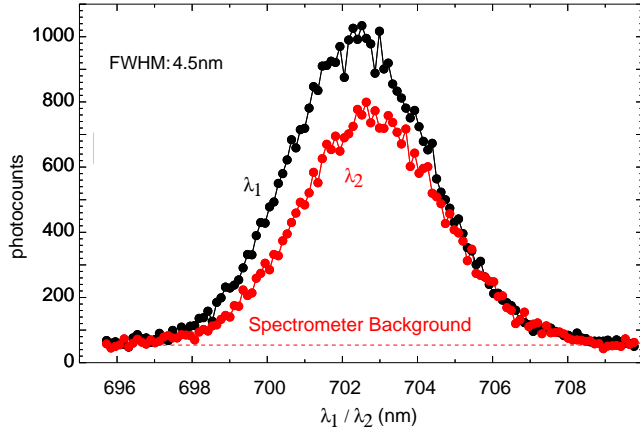


Figure 2.5: The spectra of SPDC light collected into the two single mode fibers. The FWHM of the collected spectra is 4.5 nm. The resolution of the spectrometers is approximately 0.25 nm.

the model be valid to our experimental setup. The Rayleigh range of 702.2 nm light in a beam of waist 82 microns is $z_r = \pi W^2 / \lambda \approx 30$ mm and is larger than our crystal length of 2 mm (and so the approximation should be valid).

The measured spectrum is shown in figure 2.5. The spectra was obtained from a simple grating spectrometer, with an estimated resolution of 0.25 nm. The Full Width at Half-Maximum (FWHM) of both spectra is 4.5 nm, and the peaks are centered at 702.5 nm (λ_1) and 702.8 nm (λ_2). The small offset in the central wavelength of both peaks may be attributed to residual mis-alignment of the collection modes. The collected downconversion bandwidth is still larger by about 0.5 nm despite the use of the correction factor obtained in Appendix C. This is probably due to a combination of spectrometer resolution, and unaccounted for physical effects such as pump wave-front curvature.

2.3 Measuring the entanglement quality of a photon pair

Consider the singlet Bell state that is obtained after compensation for longitudinal walk-off: $|\psi^-\rangle = 1/\sqrt{2}(|H_1V_2\rangle - |V_1H_2\rangle)$. This state cannot be factored into simple product states consisting of two photons, i.e. $|\psi^-\rangle \neq |A_1B_2\rangle$ where A and B denote arbitrary polarization states. This non-separability means that the state of one photon cannot be described without a reference to its twin. Indeed, a measurement of the polarization

state of the photons in only one arm (that ignores their twins in the other arm) will yield a randomly polarized state. Hence, the two particles are said to be in an entangled state of two photons.

Suppose that the polarization state of the photon pair is tested in the HV polarization basis, there will be only two possible outcomes: $|HV\rangle$ or $|VH\rangle$ (the subscripts 1 and 2 are dropped as the ordering is sufficient to indicate which arm is being referred to). The first outcome is obtained when a polarizing filter transmitting $|H\rangle$ is placed in arm 1, and another polarizing filter transmitting $|V\rangle$ is placed in arm 2. The second outcome is obtained when both polarizing filters are rotated by 90° . Both outcomes are detected with equal probability, and the polarization states are always anti-correlated, i.e. if both polarizers transmit $|H\rangle$ or $|V\rangle$ no photon pairs are detected.

The anti-correlation is present for different polarization bases as well. As a simple example, consider the $\pm 45^\circ$ basis that is achieved when polarizers in both arms are rotated from the HV basis by 45° . The original states $|H\rangle$ and $|V\rangle$ can be expressed in the $\pm 45^\circ$ basis as:

$$|H\rangle = \frac{1}{\sqrt{2}}(|+\rangle + |-\rangle), \quad |V\rangle = \frac{1}{\sqrt{2}}(|+\rangle - |-\rangle) \quad (2.6)$$

Hence, the singlet state is also

$$|\psi^-\rangle = \frac{1}{\sqrt{2}}(|-\rangle + |+\rangle - |+\rangle - |-\rangle), \quad (2.7)$$

with the same anti-correlation behavior in the $\pm 45^\circ$ basis.

In the actual experiment, each polarizer is a combination of one half-wave plate (HWP) and a polarizing beam splitter (PBS) set to transmit only $|H\rangle$. The only interesting outcome given a pair of HWP angles $\alpha_{1,2}$ is $H_{\alpha_1}H_{\alpha_2}$ which has a detection probability $P(H_{\alpha_1}, H_{\alpha_2})$, expressed as

$$P(H_{\alpha_1}, H_{\alpha_2}) = |\langle H_{\alpha_1}H_{\alpha_2}|\psi^-\rangle|^2. \quad (2.8)$$

Equation (2.8) can be reduced to a simple trigonometric function of the angles $\alpha_{1,2}$. This is easiest to work out by using the Jones vector notation (Appendix A) where

polarization states are represented by column vectors, and the measurement operators are denoted by matrices. In the Jones notation, the $|H\rangle$ and $|V\rangle$ states are denoted by:

$$|H\rangle = \begin{pmatrix} 1 \\ 0 \end{pmatrix}, |V\rangle = \begin{pmatrix} 0 \\ 1 \end{pmatrix} \quad (2.9)$$

A clockwise rotation by α is represented by the transformation matrix:

$$R = \begin{pmatrix} \cos \alpha & -\sin \alpha \\ \sin \alpha & \cos \alpha \end{pmatrix}. \quad (2.10)$$

To detect a photon in the state $|H_\alpha\rangle$, the HWP in front of the polarizing filter is rotated by an angle α , such that its Jones matrix is¹³

$$\begin{pmatrix} \cos 2\alpha & -\sin 2\alpha \\ -\sin 2\alpha & -\cos 2\alpha \end{pmatrix}, \quad (2.11)$$

and the state $|H_\alpha\rangle$ is:

$$|H_\alpha\rangle = \begin{pmatrix} \cos 2\alpha \\ -\sin 2\alpha \end{pmatrix} = \cos 2\alpha |H\rangle - \sin 2\alpha |V\rangle. \quad (2.12)$$

The probability of coincidence detection is expressed as:

$$P(H_{\alpha_1}, H_{\alpha_2}) = \frac{1}{2} |\sin 2(\alpha_1 - \alpha_2)|^2 \quad (2.13)$$

In the above experiment, this detection probability can be identified with the relative frequency of pair detection. A typical experimental test of the sine function is to fix one angle (e.g. α_1) while changing the other, and to measure the number of detected photon pairs for each set of angles. The polarization basis is selected by the angle that is fixed. In practice, the correlations are tested in two conjugate polarization bases, since a sinusoidal dependence in only one basis is not evidence of an entangled photon pair.

¹³A rotation by α for a HWP causes the basis to rotate by 2α .

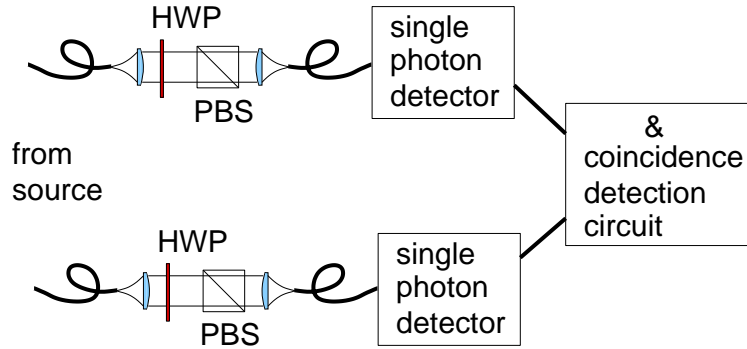


Figure 2.6: Scheme for checking polarization correlations between a photon pair. In each arm the light is sent through a half-wave plate (HWP) and a polarizing beam splitter, before being collected and sent to photon counting detectors. The angular setting of the HWP in one arm selects for the polarization basis under test (HV or $\pm 45^\circ$). The HWP in the other arm is turned by a full revolution, and for each angle of the wave plates the number of detected photon pairs is noted.

In the absence of noise, the detected correlations should be described by a sine curve with a perfect contrast. The primary effect of noise is to cause photon pair detection where there should be none, reducing the contrast of the sine curve. The quality of the state is determined from the contrast between the maximum N_{max} and minimum N_{min} number of detected pairs with $N_{min} = 0$ photon pairs described by a pure Bell state. This contrast is also known as the visibility \mathcal{V} ,

$$\mathcal{V} = \frac{N_{max} - N_{min}}{N_{max} + N_{min}} \quad (2.14)$$

A set of measured experimental correlations is shown in figure 2.7 (the experimental scheme used for polarization correlation is shown in figure 2.6). The visibility of the correlation curve in the HV basis is found to $99.9 \pm 0.6\%$, while the visibility in the $\pm 45^\circ$ basis is found to be $98.4 \pm 0.7\%$. The very high measured visibilities in two conjugate polarization bases is evidence that the source has generated a two-photon polarization-entangled state with little noise and other systematic imperfections.

It is always interesting to consider whether the visibility can be further improved, or a technical limit has been encountered. This requires an examination of the possible sources of noise.

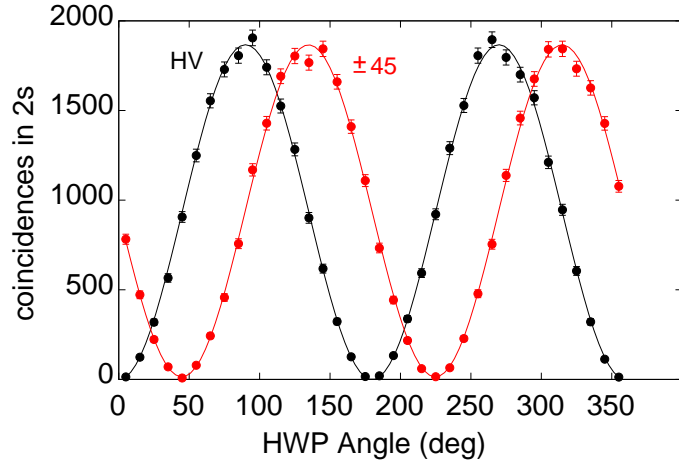


Figure 2.7: Polarization correlations in two conjugate bases. The visibility of the correlation curve in the HV basis (99.9%) is higher than that for the curve in the $\pm 45^\circ$ basis (98.4%). The lower visibility in one basis is attributed to experimental alignment and compensation errors, resulting in a residual distinguishability of the HV and VH decay paths.

One common noise source is accidental coincidences. Accidental coincidences arise when uncorrelated single photons are detected simultaneously, and wrongly identified as a valid photon pair. Accidental coincidences cause a higher background in the measured polarization correlation curves, which leads to a lower visibility. The rate of accidental coincidences a_c is determined by the relationship:

$$a_c = s_1 \times s_2 \times \tau, \quad (2.15)$$

where s_1 and s_2 are the rates of single photons in each arm, while τ is the timing-coincidence window. After a detector has registered a photon arrival, the electronic coincidence circuit waits for a time period τ to register a detection event from the other detector. Only when two detectors fire within the time period τ a coincidence will be counted.

However, accidental coincidences should affect visibility in both polarization bases equally. From the measurements presented in figure 2.7, accidental coincidences can account for at most 0.1% of the drop in visibility. The remaining 1.5% decrease in visibility for the $\pm 45^\circ$ basis requires another explanation.

In fact, such a difference in visibility for different polarization bases is characteristic of SPDC based photon pair sources. Typically, polarization correlations are very good

in the natural basis defined by the crystal axes. High contrast correlations in other bases must be achieved by using compensation crystals which correct for the relative phase ϕ between the $|H\rangle$ and $|V\rangle$ states (figure 8.4). This compensation, however, is offset by dispersive optical elements like the collection fibers that introduce arbitrary phase shifts and polarization rotations to the photons they carry. To control these unwanted dispersive effects, the optical fiber is passed through “bat-ear” polarization compensators (such as the Thorlabs Item# FPC031). These compensators work through stress-induced birefringence and vector transport on the fiber material. One interesting experimental observation is that the polarization compensators are unable to work equally well for all polarization bases. Typically one basis will have an unwanted dispersion remaining at the 1% level (this is true even for the highest quality correlations observed with this source which was reported in chapter 9). This leaves a remainder of 0.5% in the visibility difference which must be due to misalignment of the collection fibers.

2.4 Remarks on the source quality

In terms of brightness and entanglement quality, the entangled photon pair source described in this chapter is one of the best sources based on Kwiat’s 1995 design. The quality of the correlations produced also compares favorably with the output from sources based on quasi-phase matching although these newly developed sources have larger spectral brightness.

It is useful to note that high quality entanglement is important for quantum communication protocols, especially in QKD where any noise is to be treated as evidence of an eavesdropper. Hence, the performance of such protocols are not necessarily enhanced by having a spectrally bright source that has only lower entanglement quality. Furthermore, some experiments that probe the fundamental nature of physics make stringent demands on the quality of the correlations (chapter 9). The source described in this chapter is able to satisfy the requirements in both applied and fundamental studies.

In this concluding section, a comparison of different photon pair sources found in the literature is presented. Such a comparison is useful for charting the progress that has

been achieved in the field of entangled photon sources as well as to note possible future trends. The relevant parameters from the different sources are put together in table 2.1. In compiling the data, the parameters to be compared must be selected carefully because in the literature, there is a proliferation of different figures-of-merit, that do not receive consistent treatment. Table 2.1 attempts to do a comparison based on 3 different parameters: the normalized brightness of the source, the spectral brightness of the source, and the entanglement quality of the generated photon pairs.

The entanglement quality is quantified by the visibility of polarization correlations described in section 2.3. Normalized brightness is the observed rate of photon pairs normalized to input power, and has units of pairs $\text{s}^{-1} \text{mW}^{-1}$. In applications the actual rate of detected pairs is a crucial quantity, and it is why table 2.1 does not contain rates that have been corrected for experimental inefficiencies¹⁴. Some of the earlier reports do not include an input power and in these cases, the highest observed rate is reported instead.

It is possible to obtain a value for the spectral brightness (units of pairs $\text{s}^{-1} \text{mW}^{-1} \text{MHz}^{-1}$) of the source from its observed brightness. As was mentioned in chapter 1, the spectral brightness will become an increasingly important parameter in advanced quantum communication networks (section 1.3) utilizing atomic memories and repeaters [6]. It is interesting to note that some sources that are observed to have a high rate of photon pairs do not always have a large spectral brightness. Early sources [82, 84] typically do not report a bandwidth for their photon pairs, and that is why they will not have an entry for spectral brightness. It should also be noted that in many reports, the bandwidth reported is based on the use of interference filters.

Although table 2.1 does not list every single reported photon pair source in the literature, a few milestones over the last two decades may be noted. First, the entanglement quality of modern photon pair sources is very high with polarization correlation visibilities that are typically above 95%. Another development is that the observed rate of photon pairs has been rising steadily. This higher brightness is attributed to both improved technology (such as better nonlinear materials) and improved source design.

¹⁴For instance, it is often found that published rates were inflated by accounting for detector inefficiency and coupling losses. Such corrected rates, however, are not useful in actual applications.

Between 1995 and 2001, the brightness of the sources increased by two orders of magnitude primarily due to changes in source design. One variation of the 1995 Kwiat design, which is implemented in this thesis, uses no interference filters and the photon pairs were collected into single mode fibers [100]¹⁵. Since 2001, improvements in fabrication technology has allowed for the manufacture of periodically poled materials in which QPM can take place. Such materials have led to further improvements in the spectral brightness by several orders of magnitude [94]. In particular, Fiorentino *et al.* have experimentally demonstrated that confining QPM to waveguide structures can lead to unprecedented levels of spectral brightness¹⁶. A further theoretical analysis performed by Spillane *et al.* [96], found that photon pair sources based on nanophotonic waveguides would yield an astounding level of spectral brightness corresponding to $1700 \text{ pairs s}^{-1} \text{ mW}^{-1} \text{ MHz}^{-1}$. These latest developments indicate that it is very likely that in the future, the most dramatic improvements to entangled photon pair sources will come from sources based on QPM inside waveguide structures.

For completeness, two sources of heralded single photons¹⁷ have also been included. These are the sources developed by Thompson *et al.* [1] and Neegard-Nielsen *et al.* [104]. They are essentially photon pair sources and it is interesting to see that they have achieved high rates of photon pairs within very narrow bandwidths.

¹⁵A physical model describing the expected pair rate is given in the next chapter.

¹⁶It should be noted, however, that the design of the Fiorentino source does result in entangled photon pairs.

¹⁷Heralded single photons were first implemented using SPDC sources by Hong and Mandel [103].

Comparing some Photon Pair Sources					
Physical Process [†]	Observed Rate [‡] (pairs s ⁻¹ mW ⁻¹)	Entanglement Quality*	Spectral Brightness (pairs s ⁻¹ mW ⁻¹ MHz ⁻¹)	Reporting Authors	Year & Reference
Atomic Cascade	3.8 pairs s ⁻¹	≈ 84 %	0.1	Aspect <i>et al.</i>	1981 [105]
CPM	0.3 pairs s ⁻¹	> 76 %	unavailable	Ou <i>et al.</i>	1988 [82]
CPM	9 pairs s ⁻¹	> 99 %	unavailable	Kiess <i>et al.</i>	1993 [84]
CPM	10	> 97 %	3 × 10 ⁻⁶	Kwiat <i>et al.</i>	1995 [61]
CPM	140	> 98 %	5 × 10 ⁻⁵	Kwiat <i>et al.</i>	1999 [62]
CPM	900	> 96 %	3 × 10 ⁻⁴	Kurtsiefer <i>et al.</i>	2001 [100]
FWM	120	> 93 %	3 × 10 ⁻⁴	Li <i>et al.</i>	2005 [97]
QPM	8.2 × 10 ⁴	> 99 %	0.5	Fedrizzi <i>et al.</i>	2007 [94]
QPM	9.7 × 10 ⁵	unavailable	1.6	Fiorentino <i>et al.</i>	2007 [95]
QPM	n.a.	n.a.	1.7 × 10 ³ (theory only)	Spillane <i>et al.</i>	2007 [96]
FWM	7 × 10 ³	> 97 %	5 × 10 ⁻²	Fan <i>et al.</i>	2007 [99]
CPM	800	99.2 ± 0.6 %	3.3 × 10 ⁻⁴	this thesis	2007

Table 2.1: Comparison of entangled photon pair sources. It is not meant to be a complete record of all reported entangled photon sources. [†] The following abbreviations are used to denote the different physical processes used in photon pair sources: Critical Phase Matching (CPM), Four Wave Mixing (FWM) and Quasi-Phase Matching (QPM). [‡] The first three sources are not normalized to input power and have their own set of units. * Entanglement quality is evaluated by the visibility of polarization correlations and is a unitless quantity. The source that is described in this chapter is in the last row.

Heralded Single Photon Sources			
Physical Process	Spectral Brightness (s ⁻¹ MHz ⁻¹)	Reporting Authors	Year & Reference
Atomic Ensemble	5 × 10 ⁴	Thompson <i>et al.</i>	2006 [1]
QPM	1100	Neegard-Nielsen <i>et al.</i>	2007 [104]

Table 2.2: Characteristics of two heralded single photon sources. It is interesting to compare the bandwidth of the heralded single photon sources to the spectral brightness of the entangled photon sources. In this table, the bandwidth is used because it is not always easy to define the photon rate as a function of input power (e.g. for atomic systems like the one by Thompson [1]).

Chapter 3

Absolute Emission Rate of SPDC into a Single Transverse Mode

The last chapter contained a description of an experimental implementation of a fiber-coupled SPDC source and a simple bandwidth optimization method. This chapter describes a mathematical model of the SPDC source in order to better understand the key parameters controlling the absolute emission rate.

3.1 Introduction

The original studies that established the basic theory of SPDC [77, 78, 79, 80] treated the participating light fields as plane waves. Such a treatment is sometimes inadequate for analyzing modern SPDC sources. This is because many of the more recent applications often necessitate significant manipulation and transport of the photon pairs; this is achieved conveniently by guiding the light in single mode optical fibers (as described in section 2.2).

The basic idea of modeling SPDC in this regime is to map the optical modes propagating in the fibers into freely propagating modes of the electromagnetic field in the nonlinear conversion material, where they interact with a pump field. These freely propagating spatial modes can be described in good approximation by paraxial Gaussian beams.

Previous studies of SPDC light coupled into single mode fibers have focused on op-

timizing the coupling efficiency, defined as the ratio of photon pairs to single photons that are observed because this is a quantity which can be measured easily in an experiment. This quantity is important for developing loophole-free tests of Bell's inequality [106], heralded single photon sources [107, 108, 109], or simply sources of high pair brightness[100].

So far, theoretical work in this area has focused mostly on such secondary parameters, and no closed expression for the absolute rate of photon pairs was available for typical experimental configurations. This made it difficult to estimate whether a particular experimental source implementation could be improved with respect to a particular figure-of-merit, be it total rate or spectral brightness.

This chapter presents an attempt at deriving a closed expression for the absolute rate of SPDC emission from a bulk crystal into Gaussian modes. The effort is partially successful; a closed expression is obtained for SPDC in the collinear geometry (see equation (3.36)). The expression for the non-collinear geometry still has a numerical component (see equation (3.34)).

The work connects to earlier investigations of absolute SPDC rates with beams of finite diameter by Kleinman and Klyshko [78, 79]. It was found there that the overall rate of pair production is independent of the spot-size of the pump beam [78], and that the conversion efficiency of pump photons into correlated pairs integrated over all emission directions [79] is in the order of 10^{-8} per mm of crystal made of a typical non-linear material. The restriction on specific spatial modes defined by single mode optical fibers in the more recent applications, however, made it difficult to relate their results directly to experiments. The description here will apply both to Type I and II phase matching conditions, and covers collinear and noncollinear geometries important for the generation of polarization-entangled photon pairs [61, 62].

3.2 Model

Let us review in greater detail, the basic process of SPDC: the spontaneous decay of a photon from a pump field into two daughter photons propagating in two —possibly different— target modes, with the process being mediated by a material with a nonlinear

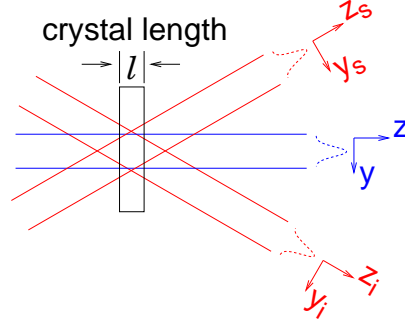


Figure 3.1: A schematic of the downconversion model considered in this chapter. The pump, signal and idler fields are treated as paraxial beams, with a Gaussian transverse intensity. The focus of all beams coincide at the crystal. The x -axis is coming out of the plane of the diagram. Coordinate systems of the signal and idler $(x_{s,i}, y_{s,i}, z_{s,i})$ are rotated about the coordinate system of the pump (x, y, z) . This figure is adapted from reference [66].

optical susceptibility. The physical implementation of SPDC utilizes the lowest order of the nonlinear susceptibility tensor $\chi^{(2)}$. While energy conservation between input and output photons typically allow the decay process to take place in many target modes, phase matching requirements need to be engineered to allow conversion to take place into any particular pair of directions.

The physical model of the three interacting optical modes is depicted in figure 3.1. The pump beam and the target modes for the downconverted light are treated as propagating paraxial beams with a Gaussian transverse profile. The beams overlap within a nonlinear optical crystal of finite length l , with surfaces normal to the propagation direction of the pump beam. Pump and target modes propagate in one plane, but need not be parallel. It is further assumed that the three interacting modes overlap in a region without a significant variation of the transverse profile along their respective propagation directions. This is a reasonable assumption for typical Gaussian beam parameters and conversion crystal lengths used in experiments [100].

Following chapter 2, I refer to the target modes as signal (index s) and idler (index i) and choose coordinate systems where the $z_{s,i,p}$ directions are parallel to the main propagation direction for each mode s, i, p (p refers to the pump mode). The spatial mode function of the electrical field for each of the modes can be written as

$$g(\mathbf{r}) = e^{ikz} \cdot U(x, y) = e^{ikz} \cdot e^{-\frac{x^2+y^2}{w^2}} \quad , \quad (3.1)$$

where k denotes the z -component of the corresponding wave vector, W the Gaussian beam waist parameter, and x, y, z refer to the corresponding coordinate system for each mode. The overlap calculations are simplified by using normalization constants α for the envelope functions $U(x, y)$ such that

$$\alpha^2 \int dx dy |U(x, y)|^2 = 1 \quad (3.2)$$

in their corresponding coordinate systems, which implies

$$\alpha_{p,s,i} = \sqrt{\frac{2}{\pi W_{p,s,i}^2}}. \quad (3.3)$$

Note that the spatial mode function $g(\mathbf{r})$ fulfills Maxwell's equations only approximately. For the calculations presented below, however, this poses no problem. Furthermore, the dispersion relation connected with this mode function has a confinement correction that is not so commonly recognized:

$$\omega^2 = c^2 \left(k^2 + \frac{2}{W^2} \right) \quad (3.4)$$

Again, for practical beam diameters W of about 100 wavelengths considered in this chapter, this correction term is small enough to safely neglect it.

3.2.1 Pump mode

The pump mode is aligned with the main coordinate system x, y, z , and treated as a classical monochromatic field of amplitude E_p^0 . This is the semi-classical approach where it is assumed that there is no significant depletion of the pump in the downconversion crystal. The electrical field of the pump can thus be written as

$$\begin{aligned} \mathbf{E}_p(\mathbf{r}, t) &= \frac{1}{2} \left[\mathbf{E}_p^{(+)}(\mathbf{r}, t) + \mathbf{E}_p^{(-)}(\mathbf{r}, t) \right] \\ &= \frac{1}{2} \left[E_p^0 \mathbf{e}_p g_p(\mathbf{r}) e^{-i\omega_p t} + c.c. \right], \end{aligned} \quad (3.5)$$

with a polarization vector \mathbf{e}_p , and a corresponding angular frequency ω_p . Using the normalization expression (3.2), the electrical field amplitude E_p^0 is connected to the

optical power P in the pump beam,

$$|E_p^0|^2 = \alpha_p^2 \frac{2P}{\epsilon_0 n_p c} \quad , \quad (3.6)$$

where the refractive index for the pump field is n_p , the electrical field constant is ϵ_0 and the speed of light in vacuum is c .

3.2.2 Collection modes

The general propagation direction of the collection modes are fixed with respect to the pump. By introducing collection mode angles $\theta_{s,i}$, and using an orientation as indicated in figure 3.1, the local coordinates of the collection modes are expressed in terms of the main coordinates x, y, z used for pump and crystal boundaries:

$$\begin{pmatrix} x_{s,i} \\ y_{s,i} \\ z_{s,i} \end{pmatrix} = \begin{pmatrix} 1 & 0 & 0 \\ 0 & \cos \theta_{s,i} & \pm \sin \theta_{s,i} \\ 0 & \mp \sin \theta_{s,i} & \cos \theta_{s,i} \end{pmatrix} \begin{pmatrix} x \\ y \\ z \end{pmatrix} \quad (3.7)$$

Then, to arrive at a rate of photon pairs generated via SPDC, the fields in the collection modes are quantized. Field quantization is done by introducing a quantization length L in the propagation direction (for clarity in the counting of modes) and postulating periodic boundary conditions; later this requirement is dropped. Following the notation in equation (3.5), the electrical field operators take the form

$$\begin{aligned} \hat{\mathbf{E}}_{s,i} &= \frac{1}{2} [\hat{\mathbf{E}}_{s,i}^{(+)}(\mathbf{r}, t) + \hat{\mathbf{E}}_{s,i}^{(-)}(\mathbf{r}, t)] \\ &= \frac{i}{2} \sum_{k_{s,i}} \left[\sqrt{\frac{2\hbar\omega_{s,i}}{n_{s,i}^2 \epsilon_0}} \frac{\alpha_{s,i}}{\sqrt{L}} \mathbf{e}_{s,i} g_{s,i}(\mathbf{r}) e^{-i\omega_{s,i}t} \hat{a}_{k_{s,i}} + h.c. \right] \end{aligned} \quad (3.8)$$

Here, $\mathbf{e}_{s,i}$ indicate the polarization vectors, and $n_{s,i}$ and $\omega_{s,i}$ the corresponding refractive indices and angular frequencies of the collection modes. The collection modes are indexed by $k_{s,i}$, and the corresponding wave vector in the pump coordinates are given by

$$\mathbf{k}_{s,i} = k_{s,i} (\mp \sin \theta_{s,i} \mathbf{e}_y + \cos \theta_{s,i} \mathbf{e}_z). \quad (3.9)$$

Motivated by an experimental situation where collection modes will get coupled into single mode optical fibers, one can work with only one transverse mode, and the longitudinal wave vector components $k_{s,i}$ serve as a complete, discrete mode index $k_{s,i} = 2\pi m_{s,i}/L$ with integer numbers $m_{s,i}$. The coefficients before the raising and lowering operators are chosen such that the free field Hamiltonian \hat{H}_0 for the collection modes takes the usual form

$$\hat{H}_0 = \sum_{k_{s,i}} \hbar\omega_{s,i} \left(\hat{a}_{k_{s,i}}^\dagger \hat{a}_{k_{s,i}} + \frac{1}{2} \right). \quad (3.10)$$

3.2.3 Interaction Hamiltonian

The SPDC process is enabled by a nonlinear optical material whose presence is described by the Hamiltonian \hat{H}_I , written in the interaction picture [76] as

$$\begin{aligned} \hat{H}_I &= -\frac{2\epsilon_0\chi^{(2)}}{8} \int_{-\infty}^{\infty} dx dy \int_{-l/2}^{l/2} dz \mathbf{E}_p^{(+)} \hat{\mathbf{E}}_s^{(-)} \hat{\mathbf{E}}_i^{(-)} + h.c. \\ &= d \int_{-\infty}^{\infty} dx dy \int_{-l/2}^{l/2} dz \left(\sum_{k_s, k_i} \frac{\hbar\sqrt{\omega_i\omega_s}}{n_s n_i} \frac{\alpha_s \alpha_i E_p^0}{L} e^{-i\Delta\omega t} g_p(\mathbf{r}) g_s^*(\mathbf{r}) g_i^*(\mathbf{r}) \hat{a}_{k_s}^\dagger \hat{a}_{k_i}^\dagger \right) \\ &+ h.c. \end{aligned} \quad (3.11)$$

The crystal is assumed to be of infinite transverse (x, y) extent, which is justified when the beam diameters are much smaller than the crystal dimensions. A frequency mismatch $\Delta\omega = \omega_p - \omega_s - \omega_i$ is introduced. The effective non-linearity d captures the contraction of the nonlinear susceptibility tensor with the corresponding polarization vectors ($2d = \mathbf{e}_p \chi^{(2)} : \mathbf{e}_s \mathbf{e}_i$) [76]. With this notation, the type of phase matching condition (type I or II) is reflected in an appropriate effective non-linearity.

Most of the scaling aspects of the parametric downconversion process connected with the geometry of the interaction Hamiltonian are determined by the overlap integral $\Phi(\Delta\mathbf{k})$ of the three mode functions $g_{p,s,i}(\mathbf{r})$ in the crystal:

$$\begin{aligned} \Phi(\Delta\mathbf{k}) &= \int dz \int dy dx g_p(\mathbf{r}) g_s^*(\mathbf{r}) g_i^*(\mathbf{r}) \\ &= \int dz \int dy dx e^{i\Delta\mathbf{k}\cdot\mathbf{r}} U_p(\mathbf{r}) U_s(\mathbf{r}) U_i(\mathbf{r}). \end{aligned} \quad (3.12)$$

In this expression, $\Delta \mathbf{k} = \mathbf{k}_p - \mathbf{k}_s - \mathbf{k}_i$ describes the wave vector mismatch. Since pump and collection modes are defined in the y - z plane, there are no wave vector components in the x -direction and hence $\Delta k_x = 0$. Carrying out the integration in the transverse directions (x, y) we arrive at

$$\Phi(\Delta \mathbf{k}) = \frac{\pi}{\sqrt{A \cdot C}} e^{-\frac{\Delta k_y^2}{4C}} \int dz e^{-Hz^2 + izK}, \quad (3.13)$$

with the abbreviations

$$A = \frac{1}{W_p^2} + \frac{1}{W_s^2} + \frac{1}{W_i^2} \quad (3.14)$$

$$C = \frac{1}{W_p^2} + \frac{\cos^2 \theta_s}{W_s^2} + \frac{\cos^2 \theta_i}{W_i^2} \quad (3.15)$$

$$D = \frac{\sin 2\theta_s}{W_s^2} - \frac{\sin 2\theta_i}{W_i^2} \quad (3.16)$$

$$F = \frac{\sin^2 \theta_s}{W_s^2} + \frac{\sin^2 \theta_i}{W_i^2} \quad (3.17)$$

$$H = F - \frac{D^2}{4C} \quad (3.18)$$

$$K = \Delta k_y \frac{D}{2C} + \Delta k_z \quad (3.19)$$

The exponential term before the residual integral in equation (3.13) represents the approximate transverse wave vector mismatch. This term can be ignored only if one of the beams is infinitely large ($W_{p,s,i} \rightarrow \infty$) or if there is perfect transverse phase matching.

The residual integral along z in equation (3.13) can be re-written in a form that allows also for a physical interpretation. I introduce Φ_z where

$$\Phi_z := \int_{-l/2}^{l/2} dz e^{-Hz^2 + izK} \quad (3.20)$$

$$= l \cdot \int_0^1 du e^{-\Xi^2 u^2} \cos(\Delta \varphi u) \quad (3.21)$$

The phase mismatch is now defined as $\Delta \varphi = Kl/2$. The argument $\Xi := \sqrt{H}l/2$ in the exponential can be viewed as a “walk-off” parameter due to noncollinear mode propa-

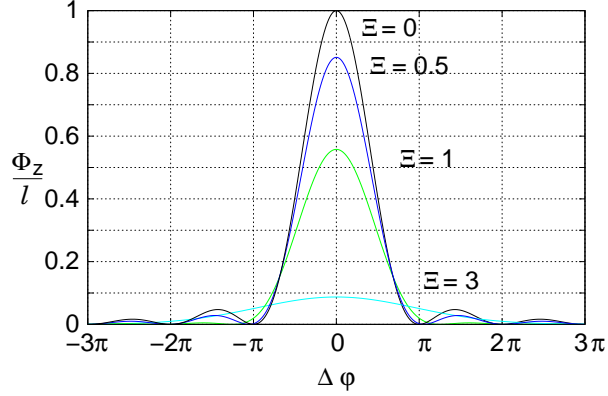


Figure 3.2: Longitudinal overlap Φ_z/l as a function of the total phase mismatch $\Delta\varphi = Kl/2$ for various walk-off parameters Ξ . For $\Xi = 0$, the typical sinc-shaped spectral distribution is revealed, whereas for large walk-off parameters $\Xi > 1$ the phase matching condition is determined by the overlap region formed by pump- and collection modes, and Φ_z/l develops into a Gaussian-like distribution. This figure is adapted from reference [66].

gation. This parameter is useful for identifying two different physical regimes which will be called the thin crystal and the thick crystal regimes [106]. In our model, these regimes refer to the physical boundary conditions imposed on the interaction volume by the geometry of the pump and collection modes.

In the thick crystal regime with a large walk-off parameter ($\Xi > 1$), the overlap integral Φ_z depends mostly on the characteristic beam parameters $W_{p,s,i}$ and not much on the physical limits of the non-linear material. For $\Xi \rightarrow \infty$ the length of the crystal ceases to play a role altogether:

$$\begin{aligned}\Phi_z &\approx l \frac{\sqrt{\pi}}{2\Xi} \text{Erf}(\Xi) \\ &= \sqrt{\frac{\pi}{H}} \text{Erf}(\Xi)\end{aligned}\quad (3.22)$$

The thin crystal regime refers to a small walk-off parameter, $\Xi \ll 1$, so that the characteristic beam parameters have almost no influence on Φ_z . In particular, this applies for collinear arrangement of all modes ($\theta_i = \theta_s = 0$), where $\Xi = 0$. In this case, $K = \Delta k_z$, and

$$\Phi_z = l \text{sinc}(\Delta\varphi)\quad (3.23)$$

This reveals the well-known influence of the longitudinal phase mismatch on the down-conversion spectral properties [78]. Figure 3.2 shows the overlap contribution Φ_z/l as

a function of the phase mismatch $\Delta\varphi$ for various walk-off parameters Ξ . Note that as Ξ becomes large, the spectrum becomes Gaussian-like. If Ξ is identified as the degree of (non)collinearity, it suggests if all beam parameters are constants, collinear emission will always have a narrower spectral profile than noncollinear emission.

3.2.4 Spectral emission rate

In order to obtain absolute emission rates, Fermi's Golden Rule is used as an expression for the transition rate $R(k_s)$ between the initial vacuum state $|i\rangle = |0_{k_s}, 0_{k_i}\rangle$ of the collection modes, and a final state $|f\rangle = \hat{a}_{k_s}^\dagger \hat{a}_{k_i}^\dagger |0_{k_s}, 0_{k_i}\rangle$ populated in the mode pair k_s, k_i . Fermi's rule applies for asymptotic scattering rates, so the relation between k_s and k_i is fixed by energy conservation:

$$\Delta\omega = \omega_p - k_s \frac{c}{n_s} - k_i \frac{c}{n_i} = 0 \quad (3.24)$$

The first step is to evaluate the transition rate $R(k_s)$ to a *fixed* collection mode index k_s . The density of states ρ per unit of energy $\hbar\Delta\omega$ is extracted out of a quasi-continuum of states for the mode k_i :

$$\rho(\Delta E) = \frac{\Delta m}{\Delta k_i} \frac{\partial k_i}{\partial(\hbar\Delta\omega)} = \frac{L}{2\pi} \frac{n_i}{\hbar c} \quad (3.25)$$

where $\Delta m/\Delta k_i = L/2\pi$ denotes the number of modes per unit of wave vector component k_i .

With the transition matrix element expressed in terms of the overlap integral $\Phi(\Delta\mathbf{k})$,

$$\langle f|\hat{H}_I|i\rangle = d \frac{\hbar\sqrt{\omega_s\omega_i}}{n_s n_i} \frac{\alpha_s \alpha_i}{L} E_p^0 \Phi(\Delta\mathbf{k}), \quad (3.26)$$

the transition rate is then given by

$$R(k_s) = \frac{2\pi}{\hbar} \left| \langle f|\hat{H}_I|i\rangle \right|^2 \rho(\Delta E) \quad (3.27)$$

$$= \left| d \alpha_s \alpha_i E_p^0 \Phi(\Delta\mathbf{k}) \right|^2 \frac{\omega_s \omega_i}{n_s^2 n_i c L} \quad (3.28)$$

The spectral emission rate per unit of angular frequency ω_s is obtained by multi-

plying $R(k_s)$ by the number of modes of k_s in a unit interval of ω_s , which is $Ln_s/2\pi c$. Hence,

$$\frac{dR(\omega_s)}{d\omega_s} = \left[\frac{d\alpha_s \alpha_i E_p^0 \Phi(\Delta\mathbf{k})}{c} \right]^2 \frac{\omega_s \omega_i}{2\pi n_s n_i} \quad (3.29)$$

At this point, the earlier introduced quantization length L has vanished as expected.

3.2.5 Total emission rate

The total pair generation rate may now be determined by integrating the spectral rate density over all frequencies ω_s . Assuming that the overlap term $\Phi(\Delta\mathbf{k})$ is only non-vanishing over a small range of frequencies ω_s , the total pair generation rate can be written as

$$R_T = \left[\frac{d\alpha_s \alpha_i E_p^0}{c} \right]^2 \frac{\omega_s \omega_i}{2\pi n_s n_i} \int d\omega_s |\Phi(\Delta\mathbf{k})|^2 \quad (3.30)$$

The dependency of $\Phi(\Delta\mathbf{k})$ on ω_s can be quite involved, as in the noncollinear case $\theta_{i,s} \neq 0$ both Δk_y and Δk_z must be considered. However, the alignment criteria for most experimental setups assume perfect longitudinal phase matching to arrive at the collection angles for degenerate downconversion[61, 100]. In these collection directions, the collection mode angles $\theta_{s,i}$ are equal. Furthermore, the typical experiment uses identical collection modes ($W_s = W_i$) [100]. Under these two conditions, it is assumed that the phase mismatch $\Delta\varphi$ is dependent only on Δk_z .

This leaves the exponential term in Φ that contains Δk_y (equation (3.13)). For experiments which collect light centered on the degenerate wavelengths with a small bandwidth (≈ 2 nm on either side of the center [100]), perfect transverse phase matching is assumed. A treatment with non-zero transverse phase mismatch will require a numerical procedure as in reference [110].

With perfect transverse phase matching, an expression for equation (3.30) is obtained. This is done by re-parameterizing the frequencies of the signal and idler about the degenerate SPDC frequency: $\omega_s = \frac{\omega_p}{2} - \delta_\omega$ and $\omega_i = \frac{\omega_p}{2} + \delta_\omega$. The approximation $\omega_s \omega_i \approx \frac{\omega_p^2}{4}$ is made by ignoring the δ_ω^2 term because R_T rapidly falls to 0 when δ_ω increases. The longitudinal wave vector mismatch is made from energy conservation

(equation (3.24)) and phase matching conditions:

$$\Delta k_z = n_s \omega_s \cos \theta_s + n_i \omega_i \cos \theta_i - n_p \omega_p \quad (3.31)$$

Hence, a dispersion relation between $d\omega_s$ and $d(\Delta k_z)$ is obtained.

$$d(\Delta k_z) = \frac{(n_i \cos \theta_i - n_s \cos \theta_s)}{c} d\omega_s \quad (3.32)$$

The emission rate can now be integrated over the longitudinal wave vector mismatch, Δk_z . Effectively, this means that we are considering the pair emission rate for all allowed wavelengths in the direction defined by our paraxial beams,

$$R_T = \frac{d^2(\alpha_i \alpha_s E_p^0)^2 \omega_p^2}{4c n_s n_i (2\pi)(n_i \cos \theta_i - n_s \cos \theta_s)} \int |\Phi(\Delta \mathbf{k})|^2 d(\Delta k_z). \quad (3.33)$$

If we recall that the pump has a Gaussian envelope, and choose all beam characteristics to be equal ($W_p = W_s = W_i$) [100], then R_T finally can be written as

$$R_T = \frac{4d^2 P l \omega_p^2}{3\pi n_p n_s n_i \epsilon_0 c^2 (\pi W_p^2) (1 + \cos \theta_i^2 + \cos \theta_s^2) (n_i \cos \theta_i - n_s \cos \theta_s)} \Phi_T, \quad (3.34)$$

where $\Phi_T := \int \left| \frac{\Phi_z(\Delta \mathbf{k}_z)}{l} \right|^2 d(\Delta k_z l/2)$. The absolute emission rate is proportional to Φ_T which has a dependence on the value of the walk-off parameter Ξ as shown in figure 3.3. The largest value of Φ_T is π , which is obtained in the thin crystal limit. In the thin crystal limit closed form expressions for the spectral and total rates are

$$\frac{d\tilde{R}(\omega_s)}{d\omega_s} = \frac{2d^2 \omega_p^2 P l^2 \text{sinc}^2(\Delta k_z l/2)}{9\pi n_p n_s n_i \epsilon_0 c^3 (\pi W_p^2)} \quad (3.35)$$

$$\tilde{R}_T = \frac{4d^2 P l \omega_p^2}{9n_s n_i n_p \epsilon_0 \pi W_p^2 (n_i - n_s) c^2}. \quad (3.36)$$

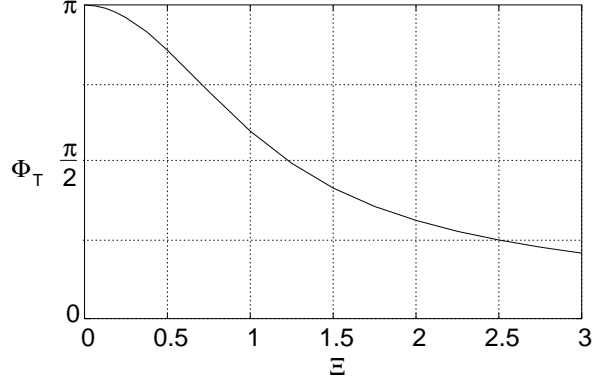


Figure 3.3: Variation of Φ_T with walkoff parameter Ξ . The absolute emission rate is proportional to Φ_T . The largest absolute rate is obtained in the thin-crystal limit when $\Phi_T = \pi$. This figure is adapted from reference [66].

3.2.6 Dependence of emission rate on beam waists

Although it is convenient to set all beam waists to be equal, this is not necessary. In fact, it can be shown that this choice does not maximize the total emission rate for a given optical pump power. This is simplest to show in the thin-crystal limit. Carrying out the more general derivation to arrive at an expression similar to (3.35), the dependency on the various beam waists W_p, W_s and W_i can be written as

$$\tilde{R}_T \propto \frac{1}{W_p^2 W_s^2 W_i^2 \left(\frac{1}{W_p^2} + \frac{1}{W_s^2} + \frac{1}{W_i^2} \right)^2}. \quad (3.37)$$

To develop an alignment strategy, we may assume that the collection modes are identical ($W_s = W_i = W$), but we re-express the pump waist as $W_p = \gamma W$. Thus, equation (3.37) reduces to

$$\tilde{R}_T \propto \frac{1}{W^2 \left(\frac{1}{\gamma} + 2\gamma \right)^2}, \quad (3.38)$$

This relationship is illustrated in figure 3.4, and exhibits a maximum of \tilde{R}_T for $\gamma = \frac{1}{\sqrt{2}}$. For $\gamma = 1$, the emission rate is about 12% lower than the maximum value. This suggests that experimental setups that are designed with equal beam waists for pump and collection modes may be further optimized, and the simple argument of maximizing a mode overlap [100] with matching beam waists does not hold.

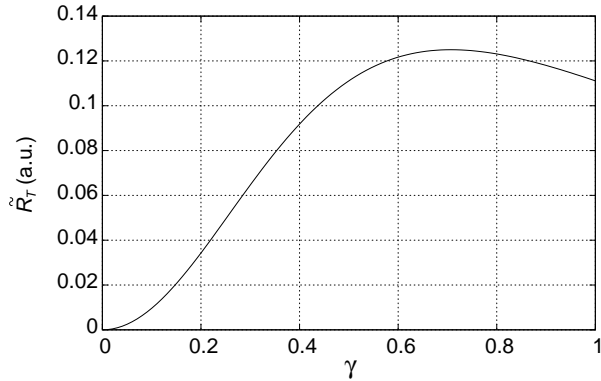


Figure 3.4: Dependence of the total pair rate \tilde{R}_T on the ratio γ between target and pump waist. The maximum emission rate can be expected at $\gamma = 1/\sqrt{2}$.

3.3 Physical interpretation and comparison to experiments

The absolute rate R_T is proportional to crystal length l , while the spectral rate $dR(\omega_s)/d\omega_s$ is proportional to the square of a sinc function. This is in agreement with results from previous work [78]. However, our expression reveals dependencies on other factors, namely pump wavelength, emission geometry and pump spot-size.

The absolute rate is proportional to the square of pump frequency since the signal and idler are re-parametrized about the degenerate frequency: so downconversion efficiency can be improved with shorter wavelength pumps as long as they are transparent in the crystal. The expression for R_T reveals that the emission rate is higher in a collinear geometry compared to a noncollinear case. This is because the noncollinear case has a smaller interaction volume.

Both the spectral and total emission rates are inversely proportional to the mode area of the beams, in contrast to previous papers which showed that the total SPDC cannot be enhanced by focusing [78, 111] (these papers, however, were not considering SPDC emission in single transverse modes). The dependence of emission rates on mode area has also been reported in a previous analysis of SPDC in waveguide structures [95]. This should not be surprising because the emission into paraxial beams is essentially the same problem as SPDC in waveguides, where the collection modes are quantized in one dimension only. For example, equation (3.35) is similar to the equation obtained in reference [95].

We should not draw the conclusion, however, that SPDC emission into single transverse modes can be arbitrarily enhanced by tight focusing. Our model is only valid in cases where the transverse profile of the beams do not vary significantly over the crystal length. For an optimization study of focus size on SPDC emission I refer the reader to reference [109].

For explicit comparison of equation (3.34) with experimental values, consider the experimental setup described in section 2.2. In this experiment a pump beam (beam waist, $W_p = 82\mu\text{m}$) at a wavelength of 351.1 nm is incident on a 2 mm thick BBO crystal. Two single mode fibers are used to collect degenerate downconverted photons, which is estimated to have an external emission angle of 3.1° . The collection modes also have beam waists of $W_{s,i} = 82\mu\text{m}$.

For uniaxial, birefringent crystals like BBO, the effective non-linearity is given by $d = d_{22} \cos^2 \theta_p \cos 3\phi_p$. The angle between pump wave vector and crystal optical axis is $\theta_p = 49.7^\circ$, while the azimuthal angle is $\phi_p = 60^\circ$, resulting in an effective nonlinearity of $9 \times 10^{-13} \text{ m/V}$ ($d_{22} = 2.11 \times 10^{-12} \text{ m}^{-1} \text{ V}^{-1}$ according to [112]). The observed pair rate is approximately $800 \text{ pairs mW}^{-1}\text{s}^{-1}$ with a pair-to-singles ratio of 0.23.

The walk-off parameter of this setup is $\Xi = 0.933$, indicating that the overlap integral is intermediate between the thin and thick crystal limits. The maximum observable rate according to our model, $2(0.23 \times R_T)$ is $1100\text{mW}^{-1}\text{s}^{-1}$. The additional factor of 2 is used because in experiments, the geometry is used to collect downconversion emission in two decay paths.

The source of the discrepancy between experiment and our model is hard to identify. The assumptions used in the model make it an overestimate, primarily in the re-parametrizing of signal and idler frequencies about the degenerate. Experimentally, there are several sources of uncertainty, the main one being the difficulty in establishing pump power very accurately. For example, the average observed value was arrived by measuring the power using two different power-meters (a Newport Model 818-UV reported 11.7mW while a Coherent Fieldmaster reported 9mW). The error in pump power estimation, however, is not sufficient to make the observed result compatible with the calculated value.

According to the model, the conversion efficiency into Gaussian transverse modes for our experimental setting will be $3 \times 10^{-12} \text{ mm}^{-1}$ of crystal. Other experimentally reported rates in the literature reveal similar downconversion efficiencies [100, 113, 107]. The total conversion efficiency of SPDC for a generic crystal was found by Klyshko to be approximately $3 \times 10^{-8} \text{ mm}^{-1} \text{ sr}^{-1}$ [79] (for degenerate SPDC with a 500 nm pump wavelength). When the collection angles used in our experiment (solid angle of $3.3 \times 10^{-5} \text{ sr}$) is taken into consideration, Klyshko's conversion efficiency is approximately $1 \times 10^{-12} \text{ mm}^{-1}$.

3.4 Implications of the model

Although the expression for absolute rates given by the model is an idealized case for the total pair emission rate, the predicted rates are only slightly larger than experimental observations. The model derived in this chapter suggests that experimental setups using single mode collection fibers (e.g. [107, 100]) operate close to the optimal limit.

Substantial increase of the emission rates are to be expected from larger nonlinearities, since emission rates are proportional to d^2 . Small mode diameters are also expected to enhance emission rates, as has been convincingly reported for SPDC experiments using waveguide structures [88, 89, 93], and a similar theoretical analysis [95]. Overall spectral brightness will be improved by combining larger nonlinearities with collinear mode confinement in longer structures. Even then, however, the spectral width is still ultimately determined by the longitudinal wave vector mismatch. This indicates that very dramatic improvements (by several orders of magnitude) to the generated pair rate in a narrow bandwidth necessary for addressing atomic systems is not very likely to be expected from bulk crystal emission.

Chapter 4

Complete Polarization State Characterization

The high quality of the polarization correlations from the implemented SPDC source was determined by measuring the visibility of polarization correlations in section 2.3. However, the exact polarization state of the photon pairs was not measured. This chapter will describe a method to completely characterize the polarization state of the photon pairs. We begin by looking at how to characterize polarization states of an ensemble of single photons.

4.1 Polarimetry and qubit state tomography

It was stated in chapter 1 that the building blocks of quantum information were known as qubits, which could be realized through the polarization state of single photons. Qubits are essentially two level (spin- $\frac{1}{2}$) quantum systems that can exist in a state described by the superposition of those two levels. Qubits are easily realised with polarization states of photons because the polarization degree of freedom is described by a two dimensional Hilbert space. For this particular physical implementation, qubit state estimation is the same as polarization state estimation. Qubit state estimation is sometimes called qubit state tomography¹. For polarization based qubits, this makes qubit state tomography

¹The simplest method of state estimation is by using a series of projective measurements because a state cannot be estimated from a single projection. Instead, several different projections are needed,

the same problem as classical polarimetry.

In some ways, the use of polarization based qubits has made the problem of qubit state estimation simpler, because one can rely on a huge body of work studying classical polarization state estimation. In fact, it is useful to point out that polarized classical light can be described as an ensemble of qubits, all sharing an identical state. In this chapter, we will see how to employ polarimetric techniques that are relevant to quantum information.

In the context of quantum information applications it is compelling to implement qubit state estimation techniques that are fast and consume as few copies of the state as possible. Research in improving the efficiency of quantum state estimation techniques is an area of active theoretical study [114, 115, 116, 117, 118, 119, 120] with much focus on qubits. Experimental reports on state estimation are fewer [121], partly because many schemes call for a joint measurement on an ensemble of qubits which is not always possible to implement.

Polarimetry that uses the least number of measurement outcomes is said to be minimal. Minimal polarimetry techniques in classical optics have been known for a long time and a lot of work in their optimization has been done [122, 123, 124, 125, 126]. While these classical methods perform well in estimating the polarization state for single photon ensembles in the limit of large numbers, their performance in the regime of extremely low light intensity (single photon level) was uncertain and it was not obvious how to use them in estimating non-classical states of light. For this reason, progress in polarimetry at the single photon limit are of interest in many areas, including characterization of faint sources of light, classical ellipsometry [122], and advanced quantum key distribution protocols [127, 128, 129].

From the different minimal estimation techniques it is desirable to implement the ones that are also optimal [116, 120]: optimal methods have the best asymptotic efficiency in determining an unknown state when averaged over all possible input states. This gives an operational definition of minimal and optimal state estimation for ensembles of prepared quantum systems. It is the technique that provides the best improve-

each providing a different section of information on the state. Such a method of state estimation from different sections is called tomography.

ment to our estimated state for each additional copy taken from the ensemble. In 2005, Řeháček *et al.* proposed such a method for state estimation of polarization based single qubits [120].

In this chapter I address the experimental problem of implementing the optimal state estimation method described in [120] by using a complete four output polarimeter with no moving parts. The technique is described in section 4.2 by reviewing the theory of optimal polarization state estimation. In section 4.3 polarization state estimation of multi-photon states is addressed. Section 4.4 is devoted to the experimental alignment procedure to make the polarimeter perform optimally. Experimental state reconstruction on ensembles of single photon and two-photon states will be illustrated in sections 4.5 and 4.6.

4.2 State estimation using the optimal polarimeter

The polarisation state of light can be completely characterized by a reduced Stokes vector that is denoted by $\vec{S}_r = (S_1, S_2, S_3)$ (Appendix A). The reduced Stokes vector identifies a point in the Poincare sphere.

A minimal scheme of estimating the Stokes vector requires exactly four detector readings, which corresponds to finding the overlap of the unknown Stokes vector with four non-coplanar vectors that define a tetrahedron in the Poincare sphere (figure 4.1). These four non-coplanar vectors define four measurement operators B_j that govern the detector readings and form a set of complete Positive Operator Value Measurements (POVM) [130]. Such POVMs that use a small number of measurement operators are called finite POVMs. The tetrahedron geometry defines the largest volume that can be enclosed by a vector quartet in the Poincare sphere, making it the optimal estimation technique when using four POVMs [124, 131]. Such a state estimation technique is also unbiased in the asymptotic limit because the total distance of any vector in the Poincare sphere to all four POVM vectors depends only on the vector's magnitude. In other words, the orientation of the unknown vector does not affect the final accuracy with which it is estimated [120]. However, the rate at which the accuracy improves does depend on the relative orientation of the unknown vector (see sections 5.3 and 5.4).

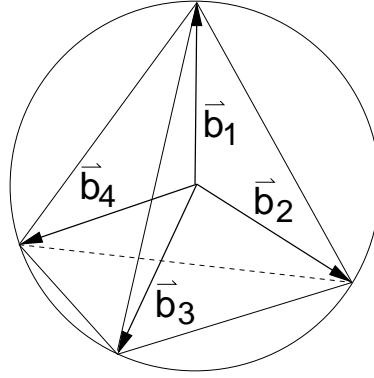


Figure 4.1: Stokes vectors for minimal and optimal polarimetry. Four reduced Stokes vectors in the Poincare sphere that form a tetrahedron define the optimal POVM operators used for polarization state estimation. The tetrahedron gives the largest volume encompassable by a vector quartet in the sphere making it the optimal measurement when using four POVMs. This figure is adapted from figure [65].

I shall denote the tetrahedron's reduced Stokes vectors by $\vec{b}_1, \vec{b}_2, \vec{b}_3, \vec{b}_4$ as shown in figure 4.1. Each measurement operator B_j may be expressed as

$$B_j = \frac{1}{4}(\vec{b}_j \cdot \vec{\sigma}), \quad (4.1)$$

where $\vec{\sigma} = (\sigma_0, \sigma_1, \sigma_2, \sigma_3)$, σ_0 being the unit matrix and $\sigma_{1,2,3}$ the Pauli matrices.

In an experiment each operator B_j is associated with a detector b_j . The average intensity falling on detector b_j is denoted as I_j . Thus expectation values of the tetrahedron operators are related to detected intensities as follows:

$$\frac{I_j}{I_t} = \langle B_j \rangle = \frac{1}{4}(\vec{b}_j \cdot \vec{S}) \quad \text{with} \quad I_t = \sum_{j=1}^4 I_j \quad (4.2)$$

Writing the intensities as a vector $\vec{I} = (I_1, I_2, I_3, I_4)/I_t$ gives the Stokes vector

$$\vec{I} = \Pi \cdot \vec{S} \quad \Leftrightarrow \quad \vec{S} = \Pi^{-1} \cdot \vec{I}, \quad (4.3)$$

where Π is referred to as the instrument matrix. Each row of this matrix is composed

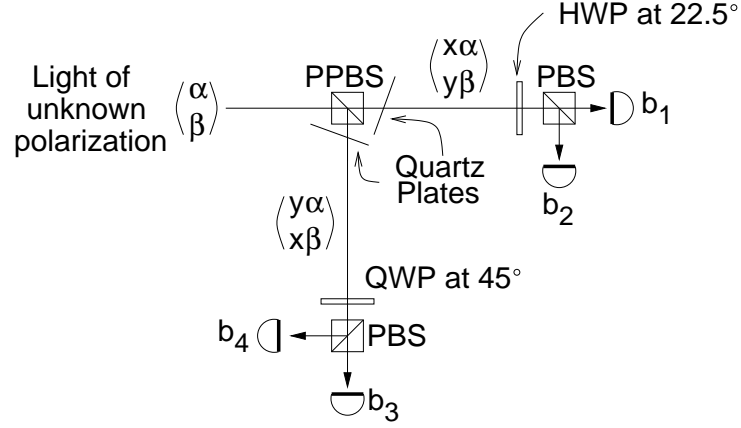


Figure 4.2: Practical implementation of the tetrahedron polarimeter that achieves the ideal instrument matrix. Each detector b_j is associated to the tetrahedron vector \vec{b}_j . The partially polarizing beam splitter (PPBS) separates incoming light according to polarization, and quartz plates remove unwanted phase shifts. Light leaving the PPBS is passed through waveplates and polarizing beam splitters (PBS) to be projected on two different bases ($\pm 45^\circ$ basis for transmitted light and the circular basis for reflected light). This figure is adapted from figure [65].

from a vector \vec{b}_j . One possible instrument matrix of the ideal polarimeter is:

$$\Pi = \frac{1}{4} \begin{pmatrix} 1 & \sqrt{\frac{1}{3}} & \sqrt{\frac{2}{3}} & 0 \\ 1 & \sqrt{\frac{1}{3}} & -\sqrt{\frac{2}{3}} & 0 \\ 1 & -\sqrt{\frac{1}{3}} & 0 & -\sqrt{\frac{2}{3}} \\ 1 & -\sqrt{\frac{1}{3}} & 0 & \sqrt{\frac{2}{3}} \end{pmatrix} \quad (4.4)$$

Experimental realisation of this instrument matrix is achieved by the polarimeter shown in figure 4.2. The first component of the polarimeter is a partially polarizing beam splitter (PPBS) that has a particular amplitude splitting ratio for incoming light, most easily determined using Jones vector notation for polarization. The amplitude division coefficients of the PPBS x and y obey energy conservation $|x^2| + |y^2| = 1$. The PPBS takes horizontally polarized light $\begin{pmatrix} 1 \\ 0 \end{pmatrix}$, to the polarizations $\begin{pmatrix} x \\ 0 \end{pmatrix}$ and $\begin{pmatrix} y \\ 0 \end{pmatrix}$ in the transmitted and reflected arm, respectively, and vertically polarized light $\begin{pmatrix} 0 \\ 1 \end{pmatrix}$, to $\begin{pmatrix} 0 \\ y \end{pmatrix}$ in transmission and $\begin{pmatrix} 0 \\ x \end{pmatrix}$ in reflection.

Light in the transmitted arm of the PPBS is projected on the $\pm 45^\circ$ polarization basis and light in the reflected arm onto the circular polarization basis, the tetrahedral

arrangement of the vectors \vec{b}_j are ensured with the following relations:

$$x^2 = \frac{1}{2} + \frac{1}{2\sqrt{3}} \quad \text{and} \quad y^2 = \frac{1}{2} - \frac{1}{2\sqrt{3}}. \quad (4.5)$$

Detailed steps are given in Appendix B.

Partially polarized light can be described using a density matrix (or coherency matrix). By writing the entries of the density matrix as a column vector $\vec{\rho}$, they can be determined from the Stokes vector [132] using the following transformation:

$$\begin{aligned} \vec{\rho} &= \frac{1}{2} \Gamma_1 \cdot \vec{S} \\ &= \frac{1}{2} \begin{pmatrix} 1 & 1 & 0 & 0 \\ 0 & 0 & 1 & i \\ 0 & 0 & 1 & -i \\ 1 & -1 & 0 & 0 \end{pmatrix} \cdot \vec{S} \end{aligned} \quad (4.6)$$

The columns of the matrix Γ_1 are the Pauli operators written as column vectors $\Gamma_1 = (\vec{\sigma}_0, \vec{\sigma}_1, \vec{\sigma}_2, \vec{\sigma}_3)$. The matrices Π^{-1} and Γ_1 can be combined into a single matrix

$$T := \frac{1}{2} \Gamma_1 \Pi^{-1} \quad \Rightarrow \quad \vec{\rho} = T \cdot \vec{I} \quad (4.7)$$

which might be referred to as a tomography matrix as it directly relates the detected intensities to the density matrix of the state.

4.3 State tomography for ensembles of multi-photons

The instrument matrix scheme above can be extended to perform polarization state tomography on ensembles of multi-photon states. James *et al.* [121] have described a similar state estimation method. I follow their approach but use the optimal and instrumentally motivated measurement operators, thereby reducing any ambiguity over the choice of operators.

The simplest multi-photon system is a photon pair detected by testing for coincidence in the detection time of their component photons. In our measurement process

each member of the photon pair is passed through a polarimeter. Given two polarimeters 1 and 2, each with four detectors b_{i_1} and b_{i_2} , respectively, ($i_1, i_2 = 0, 1, 2, 3$), there will be 16 possible coincidence combinations between the detectors (figure 4.3). Each coincidence rate is governed by an operator composed from the individual detectors' measurement operators. If the measurement operator for detectors b_{i_1} and b_{i_2} are denoted as B_{i_1} and B_{i_2} , and the coincidence count between them as c_{i_1, i_2} , the coincidence rates can be expressed as a linear function of a two-photon polarization state vector S_2 :

$$\frac{c_{i_1, i_2}}{c_t} = \langle B_{i_1} \otimes B_{i_2} \rangle = \left(\frac{1}{4} \vec{b}_{i_1} \otimes \frac{1}{4} \vec{b}_{i_2} \right) \cdot \vec{S}_2, \quad (4.8)$$

$$\text{with } c_t = \sum_{i_1, i_2=1}^4 c_{i_1, i_2}$$

Here, \vec{S}_2 is the Stokes vector equivalent for a two-photon system [121] and c_t is the total number of observed coincidences. This gives the set of measurement operators governing the coincidence pattern. The sixteen coincidences c_{i_1, i_2} can be written in column vector format $\vec{C}_2 = (c_{1,1}, c_{1,2}, \dots, c_{4,4})$. If the two-polarimeter instrument matrix is defined as Π_2 , the instrument response is analogous to equation (4.3):

$$\vec{C}_2 = \Pi_2 \cdot \vec{S}_2 \Leftrightarrow \vec{S}_2 = \Pi_2^{-1} \cdot \vec{C}_2 \quad (4.9)$$

Thus the density matrix of the two-photon state by constructing the analogous two-photon expression for equation (4.6) is:

$$\vec{\rho}_2 = \frac{1}{2^2} \Gamma_2 \cdot \vec{S}_2 = T_2 \cdot \vec{C}_2 \quad (4.10)$$

Each column of Γ_2 is the product of two Pauli operators $\sigma_{i_1} \otimes \sigma_{i_2}$ ($i_1, i_2 = 0, 1, 2, 3$) written in column vector format and T_2 is the tomography matrix for the two-photon state.

It is now straightforward to generalize this concept to obtain the density matrix for states of N correlated photons. Using N polarimeters, we obtain the pattern of N -fold coincidences to build up the coincidence vector \vec{C}_N which is used to find the N -photon

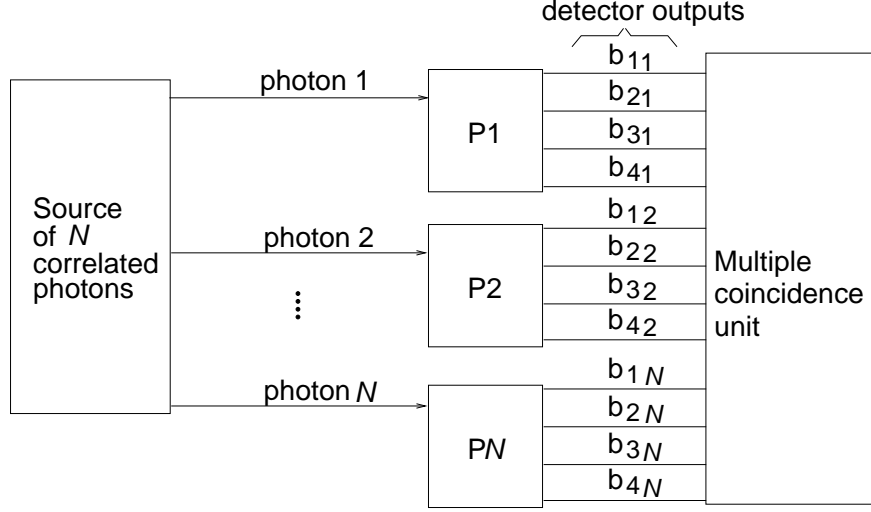


Figure 4.3: Scheme for estimating the polarization state of an ensemble of N photons using N polarimeters (P1,P2,...,PN). A multiple coincidence circuit identifies the 4^N possible coincidence combinations. For photon pairs ($N=2$), two polarimeters are used giving 16 possible coincidence combinations. Several copies of the state are processed giving a coincidence pattern used in estimating the polarization state of the ensemble. This figure is adapted from figure [65].

Stokes vector and density matrix:

$$\vec{S}_N = \Pi_N^{-1} \cdot \vec{C}_N, \quad (4.11)$$

$$\vec{\rho}_N = \frac{1}{2^N} \Gamma_N \cdot \vec{S}_N = T_N \cdot \vec{C}_N \quad (4.12)$$

Each row of the instrument matrix Π_N is given by $(\frac{1}{4}\vec{b}_{i_1} \otimes \frac{1}{4}\vec{b}_{i_2} \dots \otimes \frac{1}{4}\vec{b}_{i_N})$ and each column of Γ_N is the product of N Pauli matrices $\sigma_{i_1} \otimes \sigma_{i_2} \dots \otimes \sigma_{i_n}$ ($i_n = 0, 1, 2, 3$ and $n = 1, 2, \dots, N$). This generalized approach will work for all four-detector polarimeters in multi-photon analysis schemes (figure 4.3).

4.4 Phase correction and polarimeter calibration

4.4.1 Removing unwanted phase shifts

In the presented polarimeter, an ideal PPBS has the nominal beam splitting ratio (equation (4.5)) and also rotates the polarization state of light leaving the beamsplitter into the correct polarization basis [125]. Such beamsplitters, however, are not easily available and their design is the focus of active research [133]. The implementation here uses

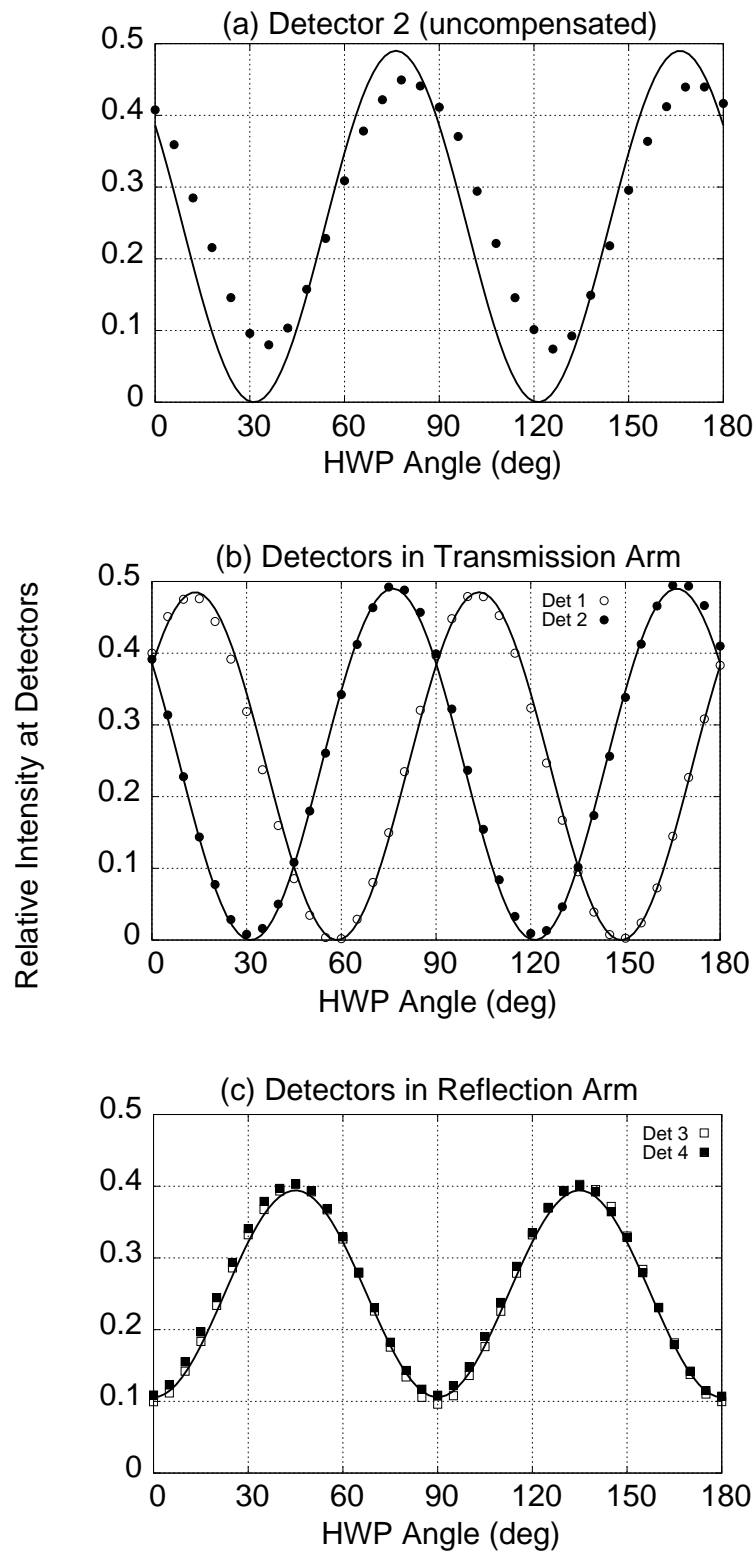


Figure 4.4: Instrument response of the polarimeter to linearly polarized light. The data points show the variation in relative intensity at each detector with respect to the angle of the half wave plate (HWP) in the polarisation state preparation. The solid lines show the expected intensity modulation for an ideal device for each HWP setting (equation (4.13)), scaled for appropriate detector efficiencies. Error bars are smaller than the point markers. Panel (a) shows the relative intensity at detector 2 without compensation plates. Panels (b) and (c) are taken with compensation for phase shifts. The oscillation in (a) is out of phase and also of lower amplitude compared to the phase corrected behaviour of detector 2 in panel (b). Plots in (c) shows a lower amplitude because light in the reflected arm is not projected on a linear polarization basis. This figure is adapted from figure [65].

beamsplitters with only the nominal intensity splitting ratio.

A PPBS without phase shift diverts light in state $-\vec{b}_j$ (that is conjugate to a tetrahedron vector \vec{b}_j) from detector b_j . General beamsplitters, however, lack this phase preserving property. The result is that input of conjugate states $-\vec{b}_j$ does not stop light from reaching the associated detectors. This suggests an easy alignment method for correcting any unwanted phase shifts with birefringent compensation plates.

For phase correction high quality horizontally polarized light was prepared using polarizers of extinction ratio 10^5 . With one subsequent half wave plate (HWP) and one quarter wave plate (QWP) it is possible to prepare any polarization state on the surface of the Poincare sphere. Compensator plates (0.5 mm thick quartz crystals) mounted on rotating stages were placed at each output arm of the PPBS, and light with a conjugate polarization state was sent to the polarimeter. For each polarization state $-\vec{b}_j$ the compensator in the relevant output arm was rotated until the detector b_j received no light. Two input states (one for each output arm) were sufficient to compensate for the unwanted phase shifts.

The compensated polarimeter behavior was verified using linearly polarized light prepared using only the polarizer and HWP (this reduces preparation errors due to residual errors in the QWP). The prepared states have a Stokes vector of the form $(1, \cos 4\psi, \sin 4\psi, 0)$, where ψ is the angle of the HWP, so the normalized response of detector 1, for example, will be

$$I_1 = 1 + \sqrt{\frac{1}{3}} \cos 4\psi + \sqrt{\frac{2}{3}} \sin 4\psi. \quad (4.13)$$

The number of photons accumulated at each single photon detector was noted for each angle of the HWP. The results are shown in figure 4.4.

The results show that the response of the compensated polarimeter is very close to ideal. The extrema of the measured intensities are less than 1° (of HWP angle) away from their nominal positions. This means that the actual measurement vectors are pointing in the same direction as the ideal tetrahedron vectors, although their magnitudes will be different due to imbalanced detection efficiencies. While this renders the asymptotic efficiency of the polarimeter less than ideal, it still represents the optimal

setup for achievable collection efficiencies. In other words, the volume defined by the experimental POVM vectors [131] is maximized.

This measurement result is limited by the accuracy of the rotation controllers. The waveplates are mounted on rotary motors with an accuracy of 0.3° . The polarizing beam splitters in the output arms have an extinction ratio of 10^4 and the waveplates' optical path length differ from their nominal values by less than 2%.

4.4.2 Calibrating the polarimeter

The instrument matrix of this polarimeter is calibrated to account for all residual phase shifts and coupling inefficiencies. A general calibration technique for four detector polarimeters (“equator-poles method”) was described by Azzam *et al.* [134]. Incidentally, the phase dependency measurement shown in figure 4.4 was an essential part of this calibration.

Using this technique it is possible to find the correction terms needed to be made to our ideal instrument matrix. A typical corrected instrument matrix Π_c is shown below:

$$\Pi_c = \frac{1}{4} \begin{pmatrix} 0.962 & 1.051\sqrt{\frac{1}{3}} & 0.920\sqrt{\frac{2}{3}} & 0.005 \\ 0.991 & 1.031\sqrt{\frac{1}{3}} & -0.956\sqrt{\frac{2}{3}} & -0.005 \\ 1.010 & -1.045\sqrt{\frac{1}{3}} & 0.005 & -0.945\sqrt{\frac{2}{3}} \\ 1.032 & -1.009\sqrt{\frac{1}{3}} & 0.029 & 1.011\sqrt{\frac{2}{3}} \end{pmatrix}.$$

The uncertainty for each of the correction terms above is on the order of 0.002. The deviation from entries in the ideal instrument matrix (equation (4.4)) is on the order of a few percent.

The phase correction and calibration steps presented above must take into account the wavelength of the input light because optical elements are specified to perform only within a certain bandwidth. The polarimeter was built to study the polarization state of light coming from the SPDC source described in chapter 2. The same light source was used for phase correction and polarimeter calibration and the experiments described in the remaining sections.

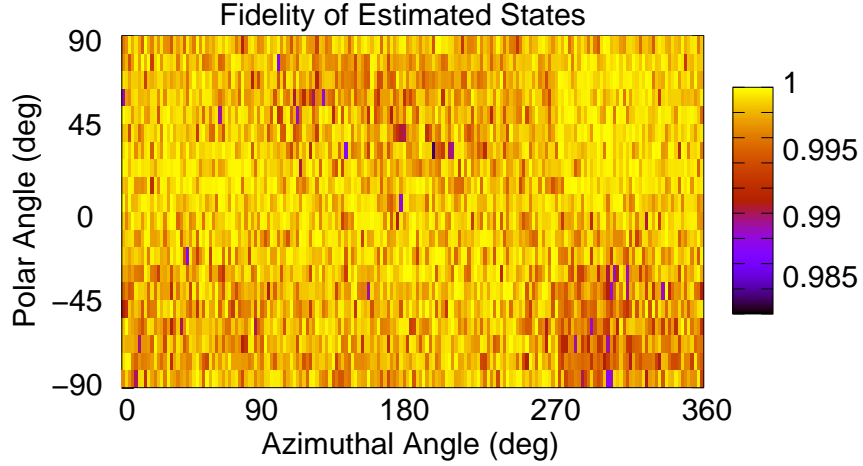


Figure 4.5: Fidelity of reconstructed states to the prepared states. A set of polarization states (\vec{S}_i) equally distributed over the Poincare sphere surface was generated; photons from each of these states were sent to the polarimeter, from which an estimated state (\vec{S}_e) is obtained. The fidelity is given by $\frac{1}{2}(\vec{S}_e \cdot \vec{S}_i)$. It is roughly constant over the Poincare sphere, showing that the polarimeter is an unbiased polarization state estimator. This figure is adapted from figure [65].

4.5 Experimental state tomography for single photon ensembles

The ability of the tetrahedron polarimeter to estimate polarization states without bias was tested by preparing a set of pure polarization states equally distributed over the Poincare sphere. In this way regions that suffer poor state estimation (if any) can be identified.

Computer controlled motors were used to rotate waveplates (after a H-filter) in preparing the set of polarization states. The Stokes vector of a pure polarization state can be expressed as $\vec{S} = (1, \cos 2\delta \cos 2[\psi + \delta], -\cos 2[\psi + \delta] \sin 2\delta, -\sin 2[\psi + \delta])$, where δ and ψ are the QWP and HWP angles, respectively. Thus any set of coordinates (characterized by the polar and azimuthal angles) on the Poincare sphere can be expressed in terms of the waveplate angles.

For each set of angles, the detectors accumulated photon detection events for one second giving a particular vector \vec{I} from which an estimated Stokes vector \vec{S}_e and probability density matrix ρ_e can be obtained via equations (4.3) and (4.6). To calculate the distance of the estimated state from the (ideal) prepared state ρ_i (\vec{S}_i), the Uhlmann fidelity is used. It is defined as $(\text{tr}[\sqrt{\sqrt{\rho_i}\rho_e\sqrt{\rho_i}}])^2$ [135, 136]. For pure states this quantity

reduces to the overlap of their Stokes vectors $\frac{1}{2}(\vec{S}_i \cdot \vec{S}_e)$.

The fidelity was mapped to the appropriate polar and azimuthal coordinates on the Poincare sphere (figure 4.5); linear polarization states correspond to a polar angle of 0° . The average fidelity for the whole map is 99.8% with a minimum fidelity of $98.4 \pm 0.9\%$ (the cumulative photon count per point is approximately 2000). There are no systematic areas of low fidelity even when wedge errors in the state preparation waveplates cause count rates to drop. This indicates that the polarimeter estimates all pure polarization states equally well.

Fidelity does not distinguish between errors introduced in state preparation from errors in the state estimation process. Therefore the state preparation apparatus was characterized independently and their contribution to the error in calculated fidelity was determined to be on the order of $\pm 0.01\%$. Thus the residual difference in fidelity is assigned to imperfections in the detection apparatus.

4.6 Experimental state tomography for a two photon ensemble

This section illustrates the use of two polarimeters to perform polarization state tomography on a two-photon state generated from an SPDC source. First, two polarimeters were correctly aligned and after calibration their instrument matrices were found to be:

$$\frac{1}{4} \begin{pmatrix} 0.903 & 0.927\sqrt{\frac{1}{3}} & 0.9997\sqrt{\frac{2}{3}} & -0.041 \\ 1.124 & 1.135\sqrt{\frac{1}{3}} & -1.014\sqrt{\frac{2}{3}} & 0.0602 \\ 0.995 & -1.079\sqrt{\frac{1}{3}} & 0.001 & 0.913\sqrt{\frac{2}{3}} \\ 0.978 & -0.983\sqrt{\frac{1}{3}} & 0.003 & -0.936\sqrt{\frac{2}{3}} \end{pmatrix}$$

and

$$\frac{1}{4} \begin{pmatrix} 1.074 & 1.171\sqrt{\frac{1}{3}} & 0.913\sqrt{\frac{2}{3}} & -0.082 \\ 0.983 & 0.8804\sqrt{\frac{1}{3}} & -1.044\sqrt{\frac{2}{3}} & 0.004 \\ 1.082 & -1.172\sqrt{\frac{1}{3}} & 0.001 & -0.9625\sqrt{\frac{2}{3}} \\ 0.862 & -0.88\sqrt{\frac{1}{3}} & -0.002 & 0.867\sqrt{\frac{2}{3}} \end{pmatrix}.$$

The SPDC source was arranged to generate photon pairs that are detected as a maximally entangled Bell state $|\Psi^+\rangle$. Bell states created via SPDC are typically characterized by a polarization correlation experiment, from which a visibility value can be obtained (section 2.3). For this particular measurement environment, the visibility measured in the HV and $\pm 45^\circ$ basis was $97.7 \pm 2\%$.

The photon pairs were passed through the polarimeters and the pattern of coincidences between them was observed. The 16 observed coincidence rates (collected using the scheme similar to [137]) make up the coincidence vector $\vec{C} = (21444, 1505, 24104, 26002, 979, 24716, 23210, 22447, 21661, 30752, 24061, 268, 19010, 23692, 339, 17695)$.

Using this vector with equations (4.9) and (4.10) we obtain the density matrix whose real components are

$$\text{Re}[\rho] = \begin{pmatrix} -0.002 & -0.01 & -0.03 & -0.024 \\ -0.01 & 0.506 & 0.485 & 0.025 \\ -0.03 & 0.485 & 0.498 & 0.009 \\ -0.024 & -0.024 & 0.009 & -0.003 \end{pmatrix},$$

while the magnitude of the imaginary components are below a value of 0.04 (figure 4.6).

The uncertainty in each of the above terms is on the order of 0.011. The Uhlmann fidelity of this state to the ideal $|\Psi^+\rangle$ state was found to be 0.990 ± 0.014 . Error bars in all cases were computed by numerical derivation and propagated Poissonian counting noise. The propagated error bars result in an estimated density matrix compatible with the ideal $|\Psi^+\rangle\langle\Psi^+|$ state.

4.7 Remarks on the minimal polarimeter

This chapter described the implementation and use of a minimal and optimal polarimeter, that can also completely describe the polarization of multi-photon states. In particular, the construction, calibration and use of the polarimeter in reconstructing single photon and two-photon states was demonstrated.

The response of the compensated polarimeter was measured over a dense sampling of states on the Poincare sphere, and found to be similar to that of an ideal device.

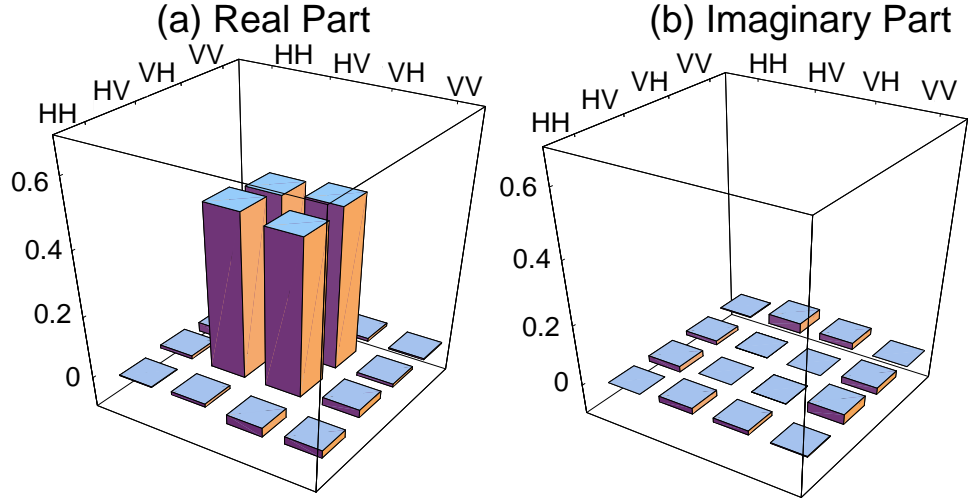


Figure 4.6: The density matrix of a Bell state $|\Psi^+\rangle\langle\Psi^+|$ obtained by linear reconstruction from photon pairs. This figure is adapted from figure [65].

This shows that minor defects in the optical elements (e.g. inexact amplitude splitting in the beam splitters) can be corrected or tolerated, making optimal polarimeters more accessible.

I also described an instrumentally motivated method for constructing the measurement operators governing light distribution to each output of the polarimeter. This instrument based approach also allows a convenient generalization to obtain measurement operators governing multi-photon coincidences. These operators can then be applied to the linear reconstruction of multi-photon Stokes vectors and their density matrices. Optimal polarimeters were then used for estimating the polarization state of experimentally prepared ensembles of single photons and photon pairs in a Bell state. The estimated states were evaluated by computing their fidelity to the (ideal) prepared states. It is found that the average fidelity in all experiments is above 99.8%.

Hence, the method I have presented works for both classical and quantum states of light. In the next chapter, we study state estimation for selected single photon and two-photon states in order to arrive at a scaling law governing the incremental improvement to the estimated state for each additional copy taken from the ensemble.

Chapter 5

Asymptotic Efficiency of Minimal & Optimal Polarimeters

5.1 Efficiency of state reconstruction

The last chapter described an implementation of minimal and optimal polarimetry, where detection of an asymptotically large (i.e. essentially infinite) number of copies of a polarization state gives an estimated vector that is very close to the true Stokes vector. Such a reconstructed state is known as the asymptotic estimate.

In many experimental scenarios, however, the experimentalist only has access to a finite sized ensemble. In these cases it is useful to have a model describing the average accuracy of a reconstruction based on the ensemble size. This chapter develops a model that provides an uncertainty budget for the tetrahedron POVM.

Finite POVMs (like the tetrahedron) do not reconstruct all states with the same efficiency, i.e. the incremental improvement to the estimated state with each additional detected copy is not uniform for all states. However, the difference between the best and worst cases is usually within counting errors making them indistinguishable. To establish a lower bound for the efficiency of state estimation, it is sufficient to study states that are reconstructed with the lowest rate of incremental improvement. In the context of the tetrahedron POVM, polarization states aligned with the tetrahedron vectors provide the worst reconstruction cases. For example, from equation (4.4) one such state has

the Stokes vector $\vec{b}_1 = (\sqrt{\frac{1}{3}}, \sqrt{\frac{2}{3}}, 0)$. Polarization states that are anti-aligned with the tetrahedron are estimated with slightly better efficiency because they have a restricted photon distribution pattern [120].

5.2 Average accuracy

In the last chapter the Uhlmann fidelity was used as a gauge of the state estimation accuracy. This chapter uses a different measure of accuracy called the trace distance D [138]. In particular, the *average* trace distance \bar{D} of an estimated state from the asymptotic estimate is desired.

Trace distance is used because it has a simple interpretation for single photon states in the Poincaré sphere. It is the geometric distance between the two points representing two states. In general trace distance is defined as $D = \frac{1}{2} \text{tr} |\rho_a - \rho_e|$, where ρ_a is the density matrix of the asymptote state, ρ_e is the density matrix of the estimated state, and $|X| = \sqrt{X^\dagger X}$. The value of D is between 0 and 1 such that $D = 0$ when $\rho_a = \rho_e$.

To determine \bar{D} all the possible ways to distribute N photons between four detectors is considered. Suppose there are k distribution patterns. For each distribution pattern $k = (n_1, n_2, n_3, n_4)$, the total number of compatible sequences is c_k where $c_k = N! / (n_1! n_2! n_3! n_4!)$. By linear reconstruction each sequence provides a Stokes vector \vec{S}_k (and trace distance value, D_k). The probability of each sequence occurring is given by $p_k = p_{k1}^{n_1} \cdot p_{k2}^{n_2} \cdot p_{k3}^{n_3} \cdot p_{k4}^{n_4}$, where p_{kj} is the probability that an input photon will arrive at detector j . The value of p_{kj} varies according to the choice of the tetrahedron vectors as well as the input state. The average of the trace distance is

$$\bar{D} = \sum_k c_k \cdot p_k \cdot D_k,$$

and \bar{D} is identified with the accuracy of our estimated state given N photons.

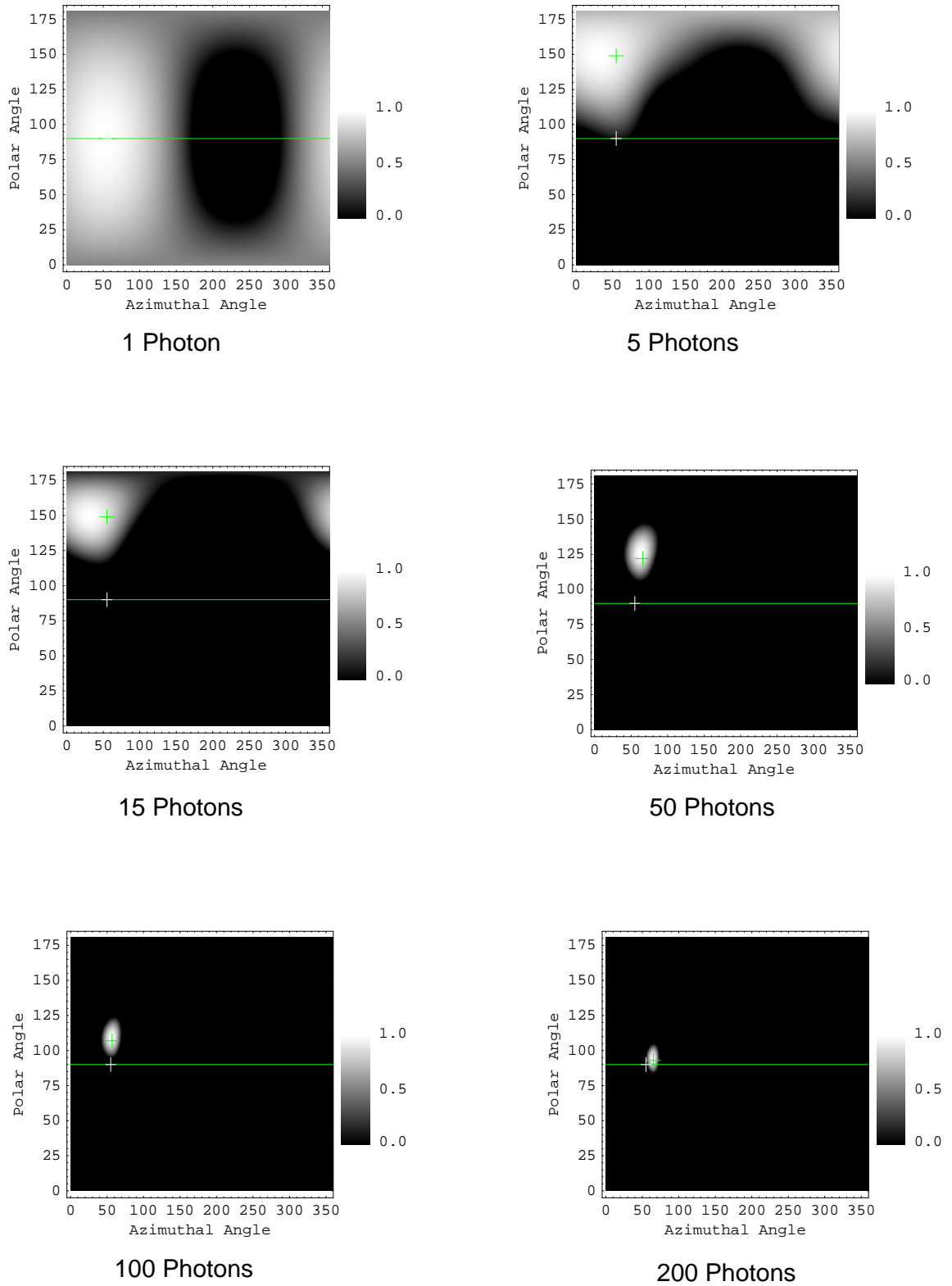


Figure 5.1: Estimated states plotted on the surface of the Poincaré sphere. The horizontal line represents linearly polarized states. Light crosses mark the prepared polarization state, and a darker cross marks the estimated state. The likelihood region is marked in white. This series of plots can be viewed as a demonstration of how accuracy and uncertainty in state reconstruction changes with increasing number of detected photons.

5.3 Accuracy in estimating single photon states

5.3.1 Direct observation on a maximally polarized single photon state

This subsection presents a direct observation of estimated states (obtained by linear reconstruction) converging to the asymptotic estimate. At the same time, a likelihood estimation is performed to find a region of states that are highly compatible with the observed pattern of photon distribution. The size of this region of this region can be interpreted qualitatively as the uncertainty in the estimate.

By operating the SPDC source as a heralded single photon source [103], it is possible to select a very well defined ensemble of photons virtually unaffected by accidental counts and background noise. An ensemble of 200 heralded photons prepared in the state $\vec{b}_1 = (\sqrt{\frac{1}{3}}, \sqrt{\frac{2}{3}}, 0)$ were detected. For each photon, the accumulated linear reconstruction is used to obtain a maximally polarized state. At the same time the likelihood region is determined. The estimated state and the likelihood region is plotted on a projection of the Poincaré sphere surface. Figure 5.1 shows a selected number of steps from the data.

It is clear that for low photon numbers, the estimated state can fluctuate wildly. However, as the accumulated number of photons increase the estimated state converges to prepared state, while the likelihood region is reduced in size showing that the uncertainty in the estimated state reduces quite rapidly.

5.3.2 Accuracy as a function of the detected number of photons

The results in the last subsection are a qualitative study of the convergence of estimated states to the asymptotic estimate. This convergence will now be studied quantitatively for the following polarization states: the tetrahedron state \vec{b}_1 , its conjugate state $-\vec{b}_1$, and the completely unpolarized state whose reduced Stokes vector is $(0, 0, 0)$. The completely unpolarized state is obtained by collecting unprepared light from one arm of the SPDC source, and is a test for the model when dealing with mixed states. The two maximally polarized states represent the worst and best cases, respectively, in the linear reconstruction of pure states.

For each test state, a very large number of heralded photons (several hundred thousand) was first measured in order to obtain an asymptotic estimate. Then 150 photons

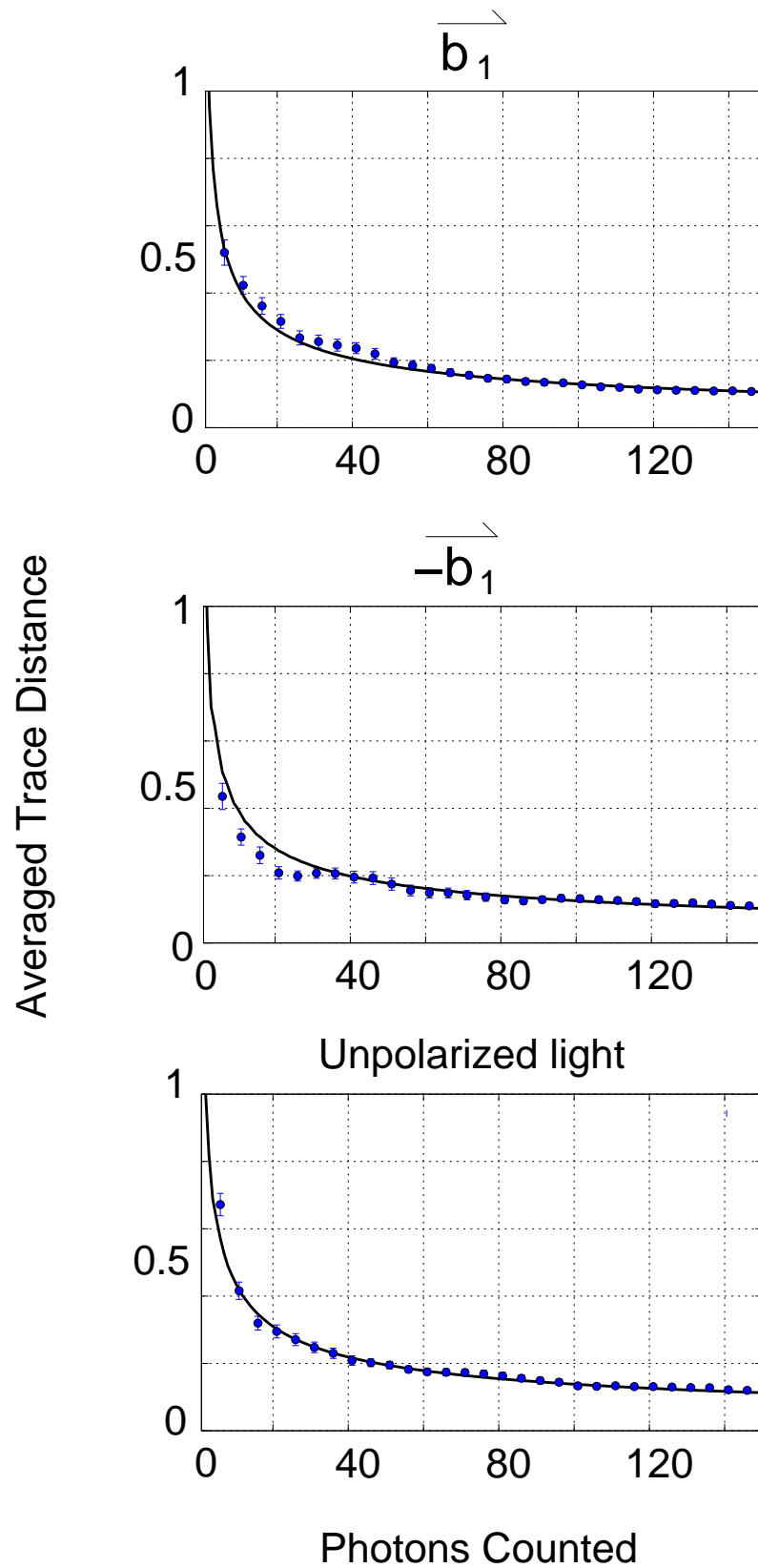


Figure 5.2: Average trace distances for three different test states, obtained by experiment (points) and by a statistical model (solid lines). The measurements were taken by averaging over 40 experimental runs, each run accumulating 150 detection events. For clarity, only a subset of the experimental data for each state are plotted.

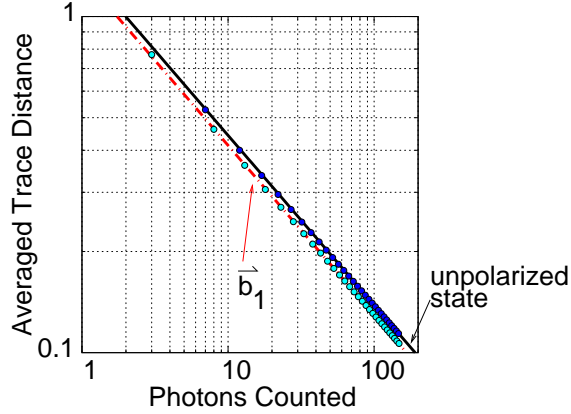


Figure 5.3: Average trace distance for two test states using only the results of the analytical model. The data points are a subset of the analytical results while the solid lines are fits to the results.

were detected and for each additional photon an estimated state was obtained by linear reconstruction, as well as the corresponding trace distance. These finite sized measurement sets were repeated 40 times, from which the average trace distance was obtained.

Selected steps in the measured data for the different test states are shown in figure 5.2. The statistically predicted average trace distance is shown by the solid line. The accuracy of the tetrahedron POVM is consistent with the statistical model for both polarized and unpolarized light and the maximum increase in accuracy occurs within the first 100 photons that are detected. Such a graph can be useful for predicting the accuracy of state estimation from a finite ensemble of photons.

5.3.3 An expression for accuracy

The results from the statistical model may be analyzed further by plotting the analytical results on a logarithmic scale as in figure 5.3. One possible expression between trace distance and sample size, N , is the following,

$$\bar{D} = \frac{a}{N^c} \quad (5.1)$$

The values of parameters a and c may be found by a least-squares fit to the analytical results, and their values for some test states are presented in table 5.1.

The c parameter indicates the rate at which information is obtained about a par-

ticular state. Indeed, from table 5.1 it is seen that c is compatible with a value of 0.5, which means that the accuracy scales as $\frac{1}{\sqrt{N}}$. This scaling law is also called the standard quantum limit. The value of the a parameter, however, seems to indicate the difficulty in estimating a particular state. Hence, the pure polarization states all have lower a values compared to the completely unpolarized state.

5.4 Accuracy in estimating two photon states

As a comparison to the single photon state, the \bar{D} value of reconstructed two-photon states was also measured. Following the single photon experiments, several hundred thousand copies of the two-photon state (prepared in section 4.6) were first detected to obtain the asymptotic estimate. Five sets, each containing five thousand detected pairs, were then analyzed. Within each set, a two-photon state was obtained by linear reconstruction for each incremental detected pair, and the corresponding trace distance to the asymptotic estimate was determined. In this way, an average of the trace distance was obtained. The result was compared with the one-photon tests.

However, instead of comparing \bar{D} directly, let us compare the normalized trace distances, \bar{D}_n defined as $\bar{D}_n = \bar{D}/(4^n - 1)$, where $(4^n - 1)$ is the number of free parameters in the system. A one-photon system has 3 free parameters while a two-photon system has 15. The normalized results are compared in figure 5.4. It is seen that for both single and two-photon systems, the normalized average trace distance is within 0.01% after 5000 detection events. This suggests that the POVM reconstructs both single and multi-photon states with the same *normalized* accuracy.

Table 5.1: Fit parameters for the test states

test state	a	c
unpolarized	1.4166	0.505525
horizontal, H	1.3122	0.505007
\vec{b}_1	1.3229	0.504702
$-\vec{b}_1$	1.2884	0.506201

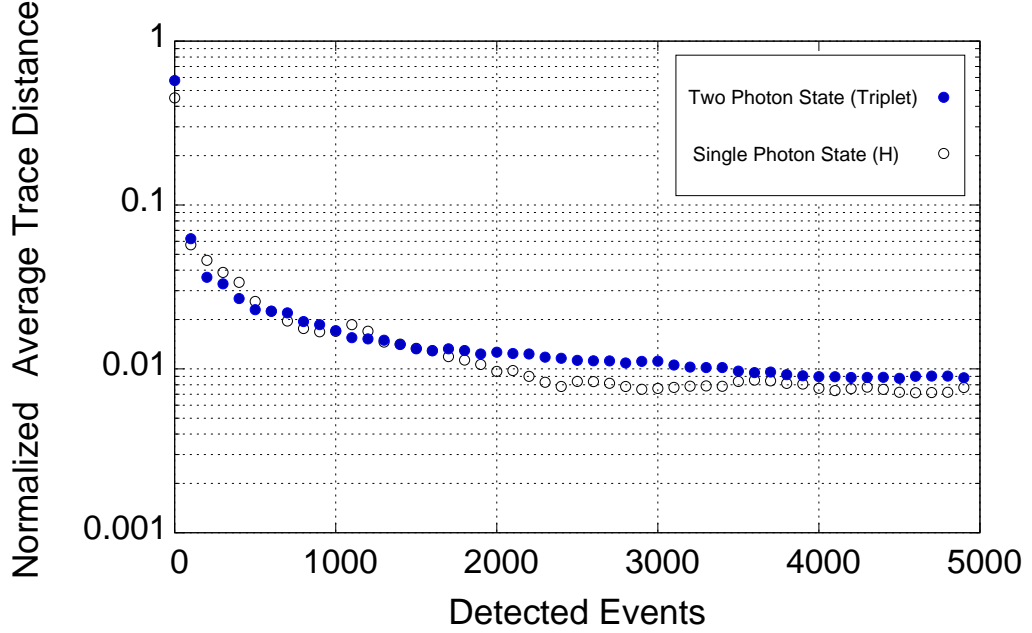


Figure 5.4: The averaged trace distances (over 5 experimental runs) for a two-photon Bell state, $|\Psi^+\rangle$ and single photon maximally horizontal polarized state, after normalizing over the number of free parameters (3 for a one-photon state, and 15 for the two-photon state).

5.5 Scaling law for multi-photon polarimetry

This chapter has presented a simple statistical model for the average accuracy (i.e. \bar{D}) of the tetrahedron POVM in reconstructing quantum systems at a given ensemble size. Furthermore, experimental results were provided for ensemble sizes in an intermediate regime that is rarely studied theoretically. It was found that the predictions of the statistical model were consistent with experimental observation.

The efficiency of state estimation was found to scale as $\frac{1}{\sqrt{N}}$, where N is the number of detected copies of the system. A similar trend was observed from a numerical simulation presented in [120]. It was seen that the difference in reconstruction efficiency between states is small - hence the tetrahedron POVM is effectively optimal for all states. From experimental observations, the accuracy in estimating a two-photon state appears to follow the same scaling law as for single photon states when normalized to the number of parameters to be estimated. It is speculated that the same scaling law would hold for all multi-photon systems. If this scaling law is found to hold for higher dimensional systems, it provides a simple way of determining the “cost” of estimating an unknown state, to any desired accuracy.

Chapter 6

Spectral Characterization of Entangled Photon Pairs

In chapter 2, the spectral bandwidth of the photons in each arm of the experimental source was measured and found to be approximately 4.5 nm. In this chapter, measurements are made to determine the actual spectral correlations between the photon pairs that are produced. It will be seen that the entanglement quality is closely connected with the spectral distinguishability of the photon pairs.

6.1 Spectral correlations of photon pairs

The SPDC process is able to generate polarization-entangled photon pairs because two different decay paths are indistinguishable apart from their polarization degree of freedom. In the source that was implemented (section 2.2), the two decay paths lead to a pair of photons that are polarized either as H_1V_2 or V_1H_2 (in the HV polarization basis). One implication of this requirement is that the spectral characteristics of the H_1V_2 pair must be identical to those of the V_1H_2 pair.

The spectral relationship that exists between photons in a pair comes from energy conservation: $\omega_p = \omega_1 + \omega_2$. When SPDC takes place with a monochromatic pump beam, there is a strict correlation between the frequencies of the downconverted photons. When the pump is no longer monochromatic the frequencies of downconverted photons are not exactly anti-correlated because of the broad range of available pump frequencies. In such

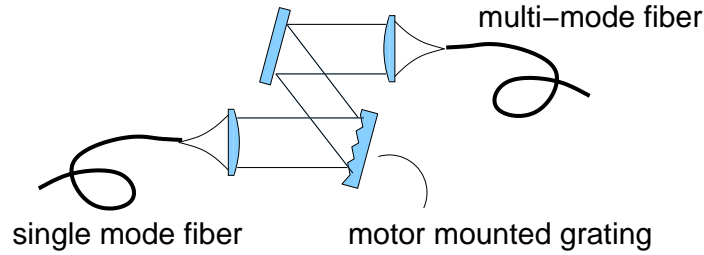


Figure 6.1: Schematic of a simple grating based spectrometer. A 1200 line per mm grating is mounted on a motorized rotation stage with a high angular resolution. The first order reflection is collected into a multi-mode fiber that goes to a single photon counter.

cases the polarization-entanglement quality is degraded and information on the SPDC decay paths can be treated as having leaked into the spectral degree of freedom. This effect was analyzed by Grice and Walmsley in reference [139], and has been observed experimentally [140, 141] with pulsed lasers that have a broad spectrum.

Such spectral correlations are not commonly studied with continuous-wave (cw) pumps because it is assumed that cw light may be approximated by monochromatic waves. This chapter presents results to show that polarization-entanglement quality is degraded even with a cw pump, as long as the pump light is not monochromatic.

Spectral properties of photon pairs can be investigated with tools like interferometers [142] or spectrometers. The tool of choice here was a very simple grating based monochromator. It is based on an interference grating that is mounted on a fine-resolution motorized rotation stage (OWIS DMT 40). The schematic for this device is shown in figure 6.1.

Input light is fed into the device from a single-mode fiber. This light is collimated and sent onto the grating. The first order interference fringe reflected off the grating is collected into a multi-mode fiber that is sent to single photon counting detectors. The device is calibrated using 632.8nm light from a standard He-Ne gas laser, by ensuring that the zeroth-order fringe at this wavelength is back reflected into the single mode fiber. Rotating the grating allows different wavelengths to couple into the multi-mode fiber. The resolution of the device was found to be 0.25nm.

To investigate the spectra of single photon ensembles only one monochromator is needed. However, two such devices were built as this allows one monochromator to be placed in each arm of the photon pair source, so that two different spectral regions could

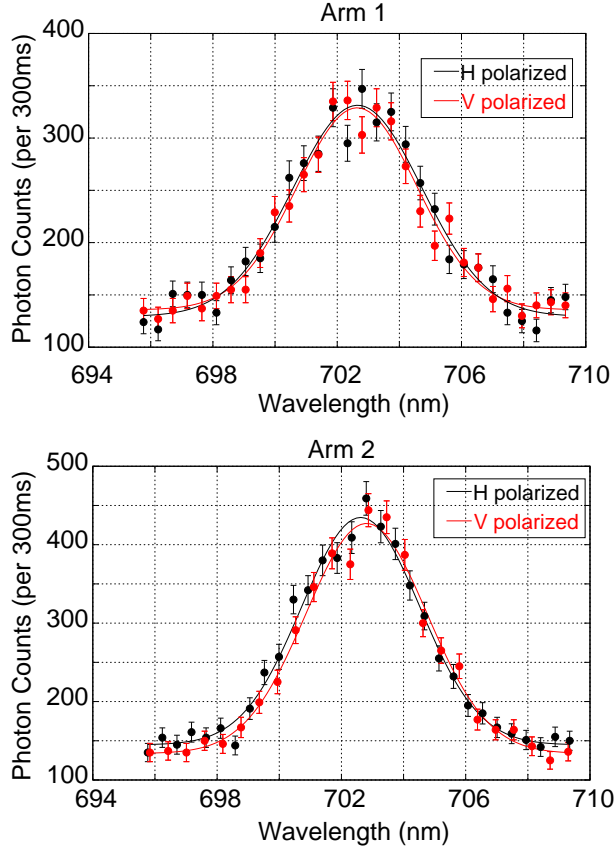


Figure 6.2: Spectra of H and V polarized light in the two different arms of the experimental source described in section 2.3. The spectra of the polarized light is practically indistinguishable, ensuring high quality polarization-correlations. The average FWHM of the spectra are 4.5 nm. There is a residual background count of approximately 300 s^{-1} .

be investigated for correlations.

A problem of this spectrometric method is that the device is lossy (not all the input light is sent into the collected first order fringe). It is also able to measure the spectrum only as fast as the motors are able to rotate. However, the spectrometer is reliable and easy to align.

6.2 Measured spectra

6.2.1 Downconversion spectra using a “clean” pump

This subsection presents measurement results on the bandwidth of polarized light from the source described in section 2.3, taken at an operating power of 35mW. Light in each arm is studied separately. A polarizing filter selects the polarization state sent to the

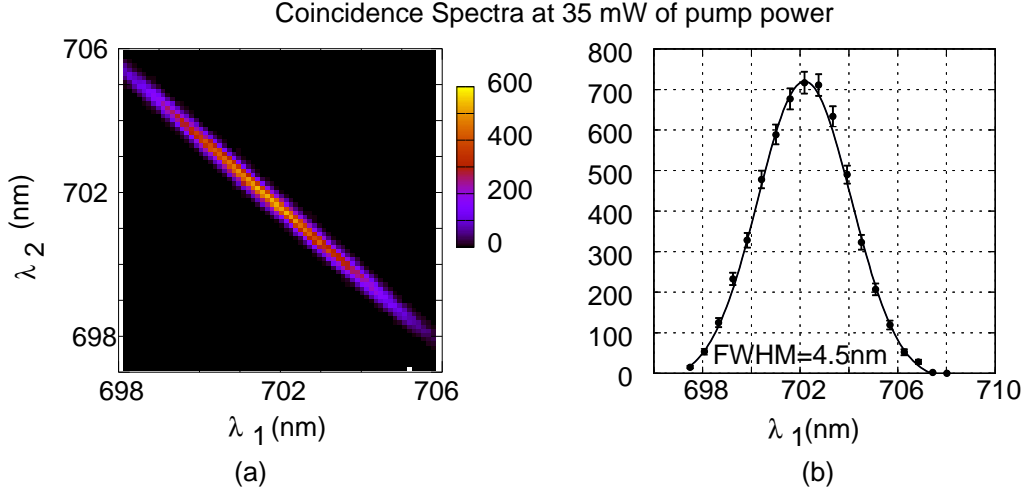


Figure 6.3: The coincidence spectrum of photon pairs. The coincidence spectrum (a) is manifested as a single line obeying energy conservation. A projection spectrum of the coincidence spectrum onto the λ_1 axis is shown in (b).

monochromator.

The measurement results are presented in figure 6.2. It is clear from the figure that the polarized spectra are almost indistinguishable. Hence the two decay paths in our setup will have almost no spectrally distinguishable information.

This is confirmed in the measured coincidence spectrum (also called a joint spectrum [142, 141]) shown in figure 6.3 (a). This spectrum is obtained by placing a monochromator in each arm of the source. The coincidence spectrum resembles a line corresponding to energy conservation (within the bandwidth of the monochromators). The measured coincidence spectra are degenerate and centred on 702.2 nm, just like the single photon spectra in figure 6.2. A projection of the coincidence spectra onto the λ_1 (or λ_2) axis also reveals a full-width at half-maximum of approximately 4.5 nm (figure 6.3 (b)). This is consistent with other single photon spectra (e.g. figure 2.5).

6.2.2 Downconversion spectra using a “dirty” pump

The purity of the polarization correlations from the source was quite high for typical pump powers of about 35 mW. The correlation quality, however, was found to degrade with higher pump power. This decrease in the polarization state purity was observed by measuring the visibility of the polarization curves in two polarization bases (HV and

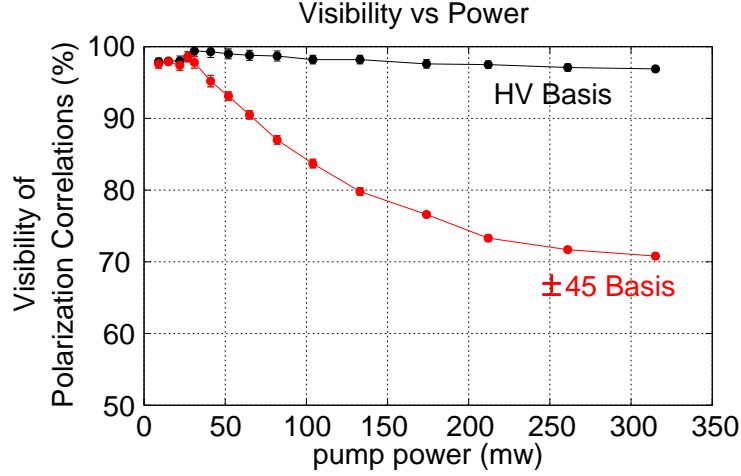


Figure 6.4: Change in polarization correlation quality with increasing pump power. The polarization correlation in the $\pm 45^\circ$ basis is reduced dramatically above 40 mW of pump power, suggesting that the collected photon pairs are no longer in a maximally entangled state.

$\pm 45^\circ$). The visibility of the correlation curves is plotted for different pump power levels in figure 6.4. Note that the decrease in average visibility becomes very pronounced after the pump power increases beyond 40mW.

One possible reason for a decrease in the quality of polarization correlations is due to increased accidental coincidences (section 2.3). Accidentals, however, should have a similar effect for polarization correlations in both the HV and $\pm 45^\circ$ basis. This is not the case here, and the loss of entanglement quality cannot be attributed to only accidental coincidences.

The decrease in average visibility was investigated in more detail using two monochromators in the heralded photon configuration [103]. The first monochromator was used to select photons with a central wavelength of 702.2 nm in one arm, and acted as the herald for the twins in the other arm. The second monochromator was scanned over a range of 4 nm, and the number of heralded photons at each wavelength was noted. It was found that after 40mW, a second peak in the SPDC spectrum appeared and grew stronger with pump power and is illustrated in the series of plots in Figure 6.5.

The coincidence spectra of the photon pairs at 70 mW and 530 mW (well into the pump power range when the second peak is present) reveal two lines as shown in figure 6.7. The main line of spectral correlations that was present at lower powers corresponded to the 351.1 nm line and the second spectral line that appeared at higher

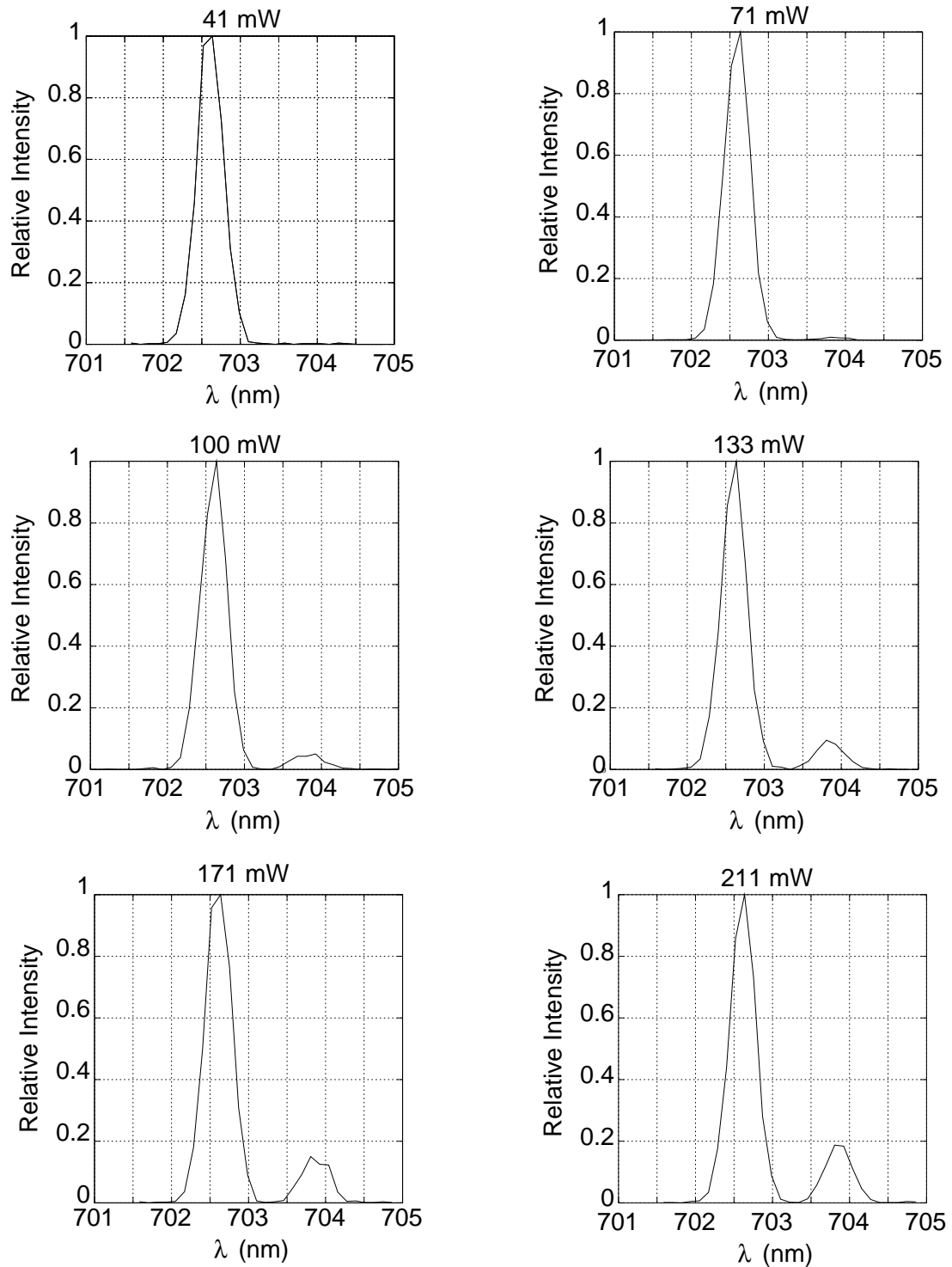


Figure 6.5: Emergence of a second spectral peak as pump power increases. The emergence of the second peak is correlated to the decrease in the quality of polarization correlations, and is evidence that information leakage into the spectral degree of freedom leads to distinguishable decay processes that degrade the quality of polarization-entanglement. In this case, the second peak in the spectrum arises from a second pump line (351.4 nm) of the Argon ion laser that becomes stronger when the lasing power is increased.

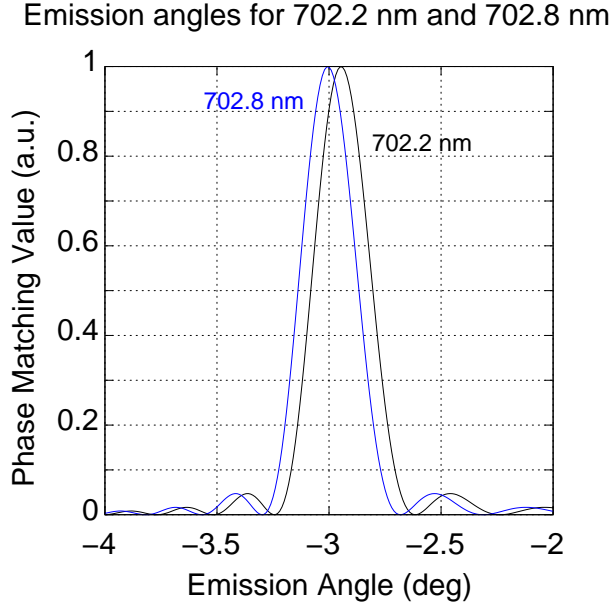


Figure 6.6: The calculated emission angles of SPDC at 702.2 nm and 702.8 nm under experimental conditions. The emission is strongest in the direction where the phase matching value equals 1. In reference to figure 2.4 (a), this is the emission angle in the plane where $\theta = 0^\circ$.

power corresponded to the 351.4 nm line. This second spectral line only appears at a higher lasing power because it had a higher energy threshold. Together, the figures 6.4, 6.5 and 6.7 provide evidence that spectral distinguishability of downconversion processes have a detrimental effect on the purity of polarization-entanglement.

Strictly speaking, both pump wavelengths are able to generate pure entangled states. Why then does the entanglement quality degrade? The reason for this is not exactly clear. Possibly the longitudinal compensation technique (section 2.2.1) is optimized only for 702.2 nm and not for 702.8 nm. It should also be noted that the degenerate entangled photon pairs generated by the second pump line have a wavelength of 702.8 nm. Consequently, the emission angle of the 702.8 nm pairs is different from that of the 702.2 nm pair generated by the original pump wavelength. This is illustrated in figure 6.6. The experimental setup is optimized to collect light from the 702.2 nm pairs, and it is not possible to accommodate the light generated by both pump wavelengths in the selected experimental design. It is very likely that unentangled photon pairs are being collected from the second pump wavelength.

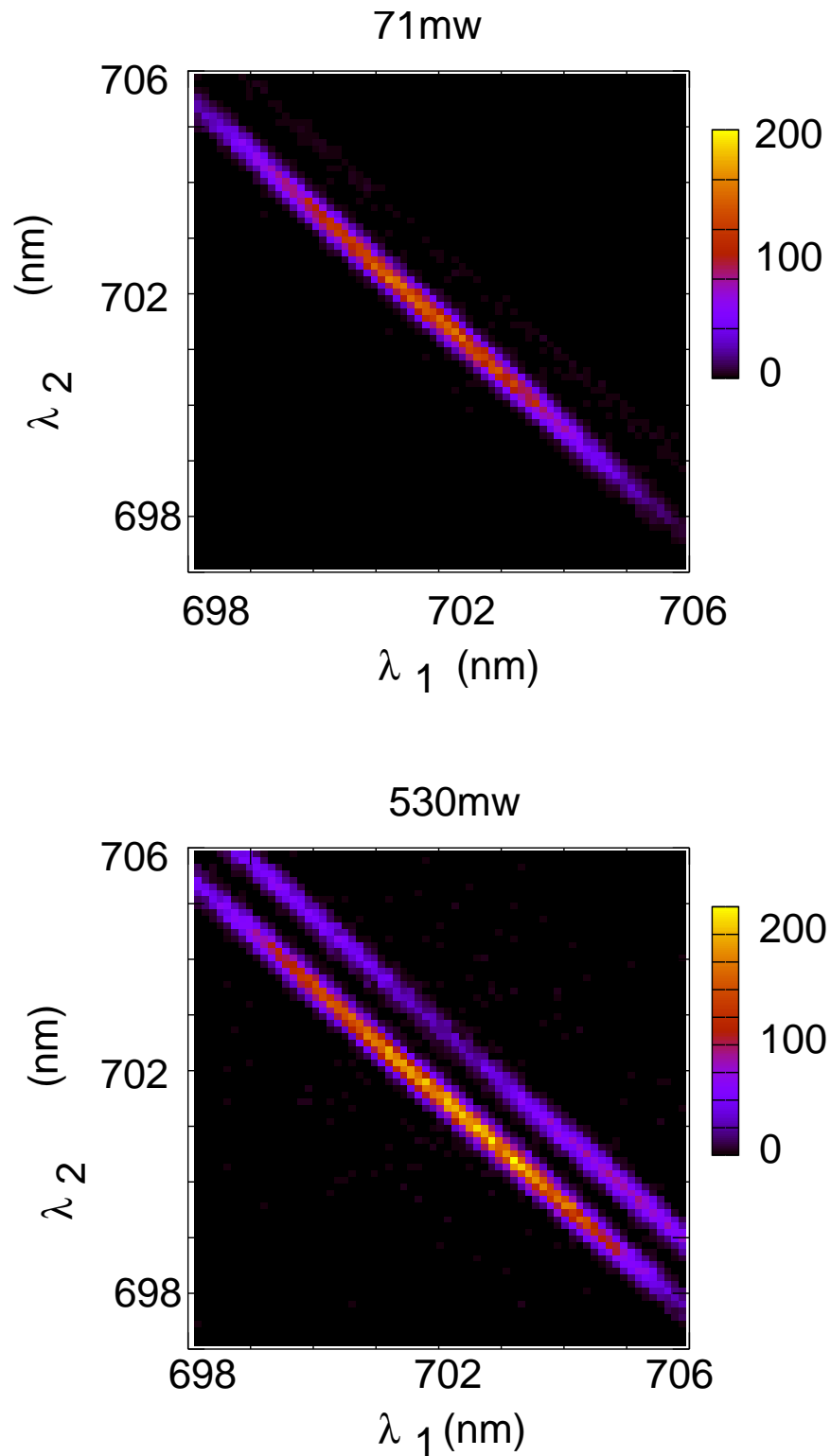


Figure 6.7: Coincidence spectrum of collected downconversion light from a spectrally “dirty” pump. The second spectral line is just visible at 71 mW. The pump at these power levels have two different wavelengths. The additional wavelength introduces an additional two decay paths. These two new decay paths are spectrally different from the original decay paths at low power.

Chapter 7

Preparing Bell states with controlled “White Noise”

The previous chapters have dealt with the issues of implementing and characterizing a photon pair source. The remainder of this thesis, will be devoted to applications for the generated photon pairs. The content of this chapter has been adopted from a paper published in Laser Physics [63]. The methods described here were first presented in the LASPHYS 05 conference held in Kyoto, Japan (2005).

7.1 Introduction

In the preceding chapters, most of the attention was given to the maximally entangled Bell states, since these states are most useful for quantum communication protocols. In a realistic situation, the photons would interact with the environment and their polarizations could change arbitrarily, or they could get mixed with stray light leading to mistaken correlations at the detectors. These arbitrary changes lead to a reduction in the (anti-)correlations between the polarization states of pairs of photons. This loss of polarization correlations is called noise, and because such losses degrade the quality of quantum communication, it becomes desirable to study noisy states and their effects.

Theoretically, the disturbance due to an eavesdropper is often modeled as white noise as this is easy to express analytically. A Werner state [143] is an example of a Bell

state plus white noise. It can be expressed as

$$\rho_W(r) = (1 - r)|\Psi^-\rangle\langle\Psi^-| + \frac{r}{4}\mathbb{1} \quad (7.1)$$

where r is the noise admixture.

However, real noise often does not fit the characteristics of white noise[144]. To test theoretical claims of security protocols based on white noise, it is desirable to make idealized sources of noise. The creation of Werner states has been reported previously [145, 146, 147], and the common feature of these experiments was the use of a technique called temporal decoherence.

Temporal decoherence occurs when one photon in a Bell state is delayed beyond the coherence time. Thus, when coincidences are looked for the polarization correlations are less than ideal. In principle, this could be achieved by making one of the photons take a longer optical path, like an optical fiber. Previous experiments have all utilized quartz plates of varying thicknesses to achieve the timing delay. However, this is cumbersome because one would need a large collection of quartz plates to input an arbitrary amount of noise.

This chapter describes two methods for generating Werner states that avoid the use of quartz plates. The first method still uses temporal decoherence but is achieved by manipulating the detection apparatus directly. The second method uses blackbody radiation.

7.2 Making noise

7.2.1 Inducing noise via a time window

It is possible to induce white noise in our measured Bell state by manipulating the coincidence time window τ of the measurement apparatus (section 2.3). The ratio of photon pairs to singles for our experimental setup is approximately 20%. Hence, the majority of detected photons are not identified as part of a pair. To simulate noise, it is sufficient to make the detection system count these single photons as coincidences.

If the length of the time window τ was increased, the probability of detecting an

accidental coincidence increases. Essentially the system begins identifying unrelated photons as a pair. These are accidental coincidences α_c . Because the polarization of unrelated photons are not correlated, accidental pairs lead to white noise. A simple model that relates the visibility of the polarization correlations \mathcal{V} to τ is the following:

$$\begin{aligned}\mathcal{V} &= \frac{N_{max} - N_{min}}{N_{max} + N_{min} + 2s_1s_2\tau} \\ &= \frac{\mathcal{V}_o}{1 + \frac{2s_1s_2}{N_{max}+N_{min}}\tau} \\ &= \frac{\mathcal{V}_o}{1 + b\tau}\end{aligned}\tag{7.2}$$

In this expression, \mathcal{V}_o is the visibility that would be obtained the measurement apparatus had an infinitely sharp timing resolution (i.e. the $\tau = 0$). The model assumes that the α_c is a constant value¹.

In experiment, the time window value is controlled by a variable capacitor, allowing the width to be varied continuously. For each value of the time window a polarization correlation test was performed. Figure 7.1 shows the measured visibilities as function of time window values². A least squares fit to the data using equation (7.2) yields $\mathcal{V}_o = 0.97$ and $b = 0.000675$. This is taken to mean that before any noise was added, the visibility of the polarization correlations was at 97%.

7.2.2 Inducing noise via a blackbody

In the second method, an incandescent light bulb was used to mix thermal light with the collected downconversion light. An increase in noise is obtained by increasing the power delivered to the light bulb. Although increasing the power delivered to the light bulb would change the temperature of the filament and change the spectrum of the thermal light, this problem can be overcome by using interference filters with a FWHM of 5 nm (which is slightly larger than the bandwidth of light collected into single mode fibers at the SPDC source).

¹See section 2.3 for a discussion of how to calculate \mathcal{V} and how noise reduces its value.

² The measurements were limited to a maximum value of the time window because of the electronic components.

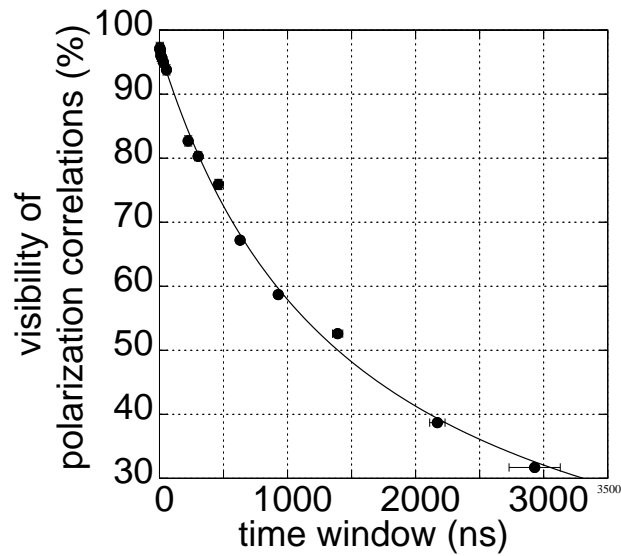


Figure 7.1: The visibility plotted against coincidence window time. Increasing the time window leads to more accidental coincidences and a corresponding loss of polarization correlation purity. The solid line is a fitted curve provided by a theoretical model. This figure is adapted from reference [63].

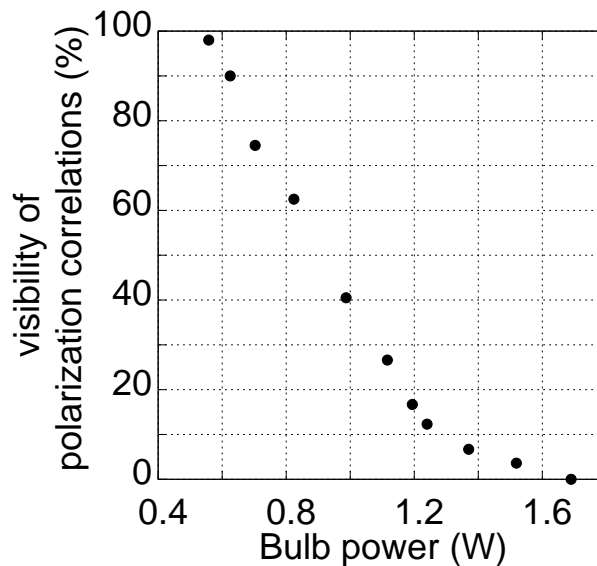


Figure 7.2: The visibility of polarization correlations plotted against the power supplied to the light bulb. Error bars here are much smaller than the plot markers. This figure is adapted from reference [63].

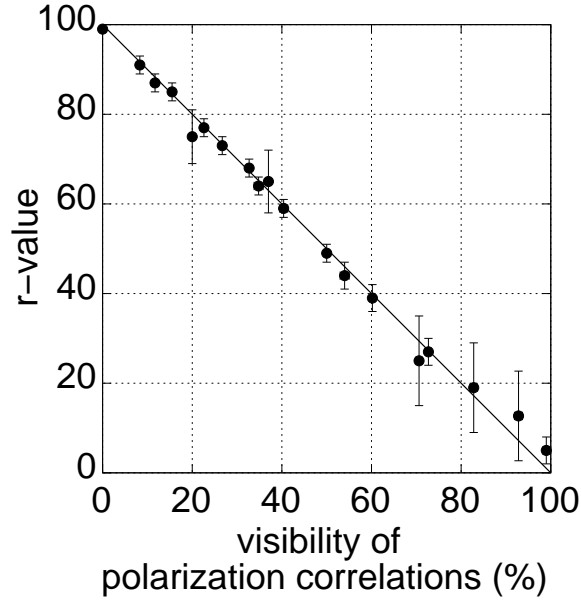


Figure 7.3: The noise admixture calculated from the tomographically obtained density matrices. The straight line is the predicted r value for corresponding visibility of the polarization correlation. This figure is adapted from reference [63].

The light bulbs are placed at any suitable position along the photon transmission channel. The resulting mixed light is then checked for polarization correlations. The change in visibility with power is shown in figure 7.2. The results show that it is possible to cause polarization correlations to reach 0% by this method, as the limit is the maximum power the light bulb can sustain.

The drop in visibility at lower bulb power levels is much faster than at high power. A simple model for the variation of \mathcal{V} with bulb power is not available because it is quite difficult to account for the saturation behavior of the detection apparatus³.

The noise admixture of a Werner state, r , and the visibility are related simply by $\text{visibility} = 1 - r$. To confirm that these methods do create a Werner state, polarization state tomography was performed and it was found that the noise admixture calculated from these density matrices vary with visibility as predicted.

³As bulb power increases, the number of thermal photons detected increases. The detection system, however, has a dead time on the order of $1.5 \mu\text{s}$ per detection event. This dead time causes fewer photons to be counted.

7.3 Density matrix of Werner states

The general density matrix of a Werner state looks like

$$\rho_W = \begin{pmatrix} \frac{r}{4} & 0 & 0 & 0 \\ 0 & \frac{2-r}{4} & \frac{r-1}{2} & 0 \\ 0 & \frac{r-1}{4} & \frac{2-r}{4} & 0 \\ 0 & 0 & 0 & \frac{r}{4} \end{pmatrix}. \quad (7.3)$$

The r values represent the amount of noise in the system. The ideal singlet state will have $r = 0$, and only the central terms of the density matrix will be non-zero. Thus, the values of r can be easily extracted from the elements of the density matrix by the following equation:

$$r = 1 + \frac{2}{3}(\rho_{11} + \rho_{44} - \rho_{22} - \rho_{33}) + \frac{1}{3}(\rho_{23} + \rho_{32}). \quad (7.4)$$

Polarization state tomography was performed for a number of states that have different polarization correlation visibilities. The noisy states used for tomography were generated by the method of mixing light from a light bulb. For each state, an estimated density matrix was obtained from which the associated r -value could be determined. The r values were plotted against the corresponding polarization correlation quality and are shown in figure 7.3. The measured data follows the theoretical model consistently, providing evidence that our selected method produced Werner states consistently over the entire range of polarization visibilities.

7.4 Spectral character of the Werner state

In most methods of producing Werner states the noise can be removed in trivial ways. For example, if a quartz plate was used to introduce timing delays, another quartz plate of the same thickness oriented properly at another place in the transmission line would reverse the delay. Similarly, in the method of generating noisy states via a larger time window, the noise could be removed by reducing the time window size.

A Werner state created by mixing with stray light, however, is much harder to

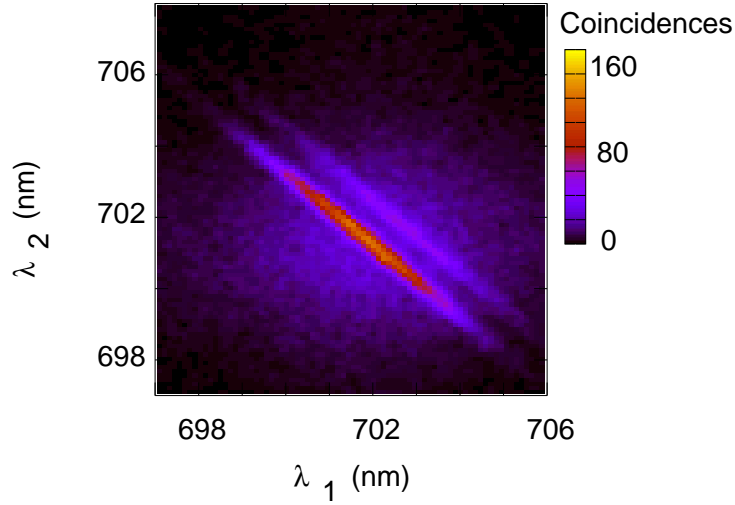


Figure 7.4: Coincidence spectrum of a Werner state. The amount of background light here was sufficient to create a Werner state with $r = 46\%$. The pump power was increased to allow the spectrum to be collected faster (leading to the two downconversion lines), but the raised background is indicative of the thermal light that has been mixed with the collected photon pairs. This figure is adapted from reference [63].

correct. In particular, one would need to see if thermal photons can be distinguished from SPDC photons. To better understand these effects the coincidence spectrum of the Werner states was measured.

The coincidence spectra for a Werner state obtained by using thermal light mixing is presented in figure 7.4. In the figure the downconversion lines are in a raised background of coincidences. This background light is scattered almost uniformly across the coincidence spectrum, while the downconversion light are restricted by energy conservation (with the pump frequencies) to two lines. Under normal operating conditions (20 mW of pump power), the weaker line corresponding to 351.4 nm of UV light is not present. It is present in this graph, because the pump power was increased to facilitate a quicker mapping of the coincidence spectrum. More importantly, however, the thermal light seems to be mixed in equally over the entire collected spectrum. With very narrow spectral filters one could hopefully remove most but never all of the thermal light. In this sense, an irreversible Werner state has been created.

Chapter 8

An experimental demonstration of the Ekert QKD protocol

8.1 Entanglement-based QKD

Widespread interest in quantum communication began with the publication of proposals for quantum key distribution (QKD) between two parties (traditionally the transmitter is called Alice and the receiver is called Bob) over two decades ago [14]. As pointed out in chapter 1, QKD was the first quantum information protocol to be implemented experimentally [23], and is still the most mature of any application that claims to be based on quantum information. This is evident from the commercial QKD devices that are now available.

Despite this, active research into QKD still continues because there are many interesting questions left to be resolved. One of them involves the question of whether entanglement can provide security for QKD beyond the BB84 protocol (and its variations, e.g. the decoy-state protocol [28]). This chapter describes a QKD experiment that investigates such a possibility. Let us begin by reviewing in some detail the 1984 protocol of Bennett and Brassard (BB84).

BB84 seeks to distribute a random encryption key (or Vernam cipher) via correlated preparation and measurement of the polarization states of single photons [14, 23]. Its strength was derived from the no-cloning theorem [21, 22] which stated that the po-

larization state of a single quantum system cannot be copied perfectly. It also implied that any attempt to copy the polarization state will cause its alteration or destruction. A measurement attempt on the distributed key is revealed as errors in the expected correlation of the polarization states.

Errors in the polarization correlations may also be caused by harmless decoherence, but these are indistinguishable from errors caused by eavesdropping. Hence, BB84 treats all noise as evidence of an eavesdropper. In practice, all distributed keys will initially have some noise, and classical communication must be employed to remove it, with a final step where any knowledge possessed by an eavesdropper is eliminated. This classical process of obtaining the final secure key is called error correction and privacy amplification [148]. Whether a completely secure key can be distilled depends on the fraction of errors in the initial key.

In BB84 each of the key-carrying photons has a well defined polarization state (figure 8.1). It is possible, in the preparation basis, to predict with absolute certainty the outcome of a polarization measurement based on the knowledge of the polarization state. In the language of classical physics, the photons are said to have an “element of reality”.

This, however, is not necessary and QKD can be performed with photons whose polarization state are not defined until a measurement has been carried out. Such a protocol was proposed in 1991 by Ekert (E91) [18]. The E91 protocol makes use of the states of maximally-entangled photon pairs where the measurement outcome on one photon appears random unless compared with the measurement outcome of its entangled twin. When both photons are measured in the same polarization basis they will always turn out to be perfectly correlated (section 2.3). Hence, if Alice and Bob share a stream of polarization-entangled photon pairs, they only have to randomly select their measurement bases and half the time they will have measurements from which it is possible to derive a secure key (figure 8.2).

The quality of entanglement for an ensemble of photon pairs can be measured by looking at the polarization correlations in two different polarization bases (section 2.3). An alternative method is to measure the degree of violation of a Bell inequality [149] (e.g.

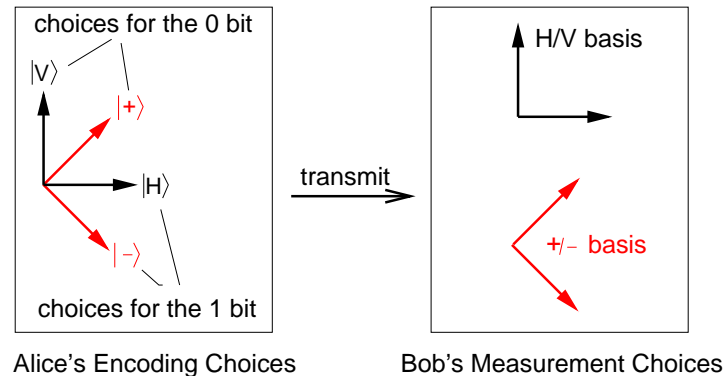


Figure 8.1: Schematic of the BB84 protocol for quantum key distribution between two parties (Alice and Bob). Bob must decide randomly between the 0 and 1 bits, as well as the polarization basis in which to encode the bit. Alice must choose randomly the measurement basis. Half the time the transmitted state is not in the measurement basis and such outcomes are discarded. The remaining cases can be used to derive a secure key. Since the polarization state is encoded before transmission, the photons have “an element of reality”.

the Clauser-Horne-Shimony-Holt (CHSH) inequality [39])). The defining feature in E91 is the suggestion to use the degree of violation of a Bell inequality as a test of security. This conjecture is related to a concept called the monogamy of entanglement [150]: the entanglement between two systems decreases when a third system (for example, the measurement apparatus of an eavesdropper) interacts with the pair.

The drawback of the original E91 protocol was that it lacked a quantitative method for determining the knowledge of an eavesdropper. This was supplied by Fuchs et al. [19] who showed that the error fraction in an E91 key is related to the degree of violation of the CHSH inequality. For entanglement-based QKD it is sufficient to monitor the CHSH violation and then derive the error fraction for use in privacy amplification. Note that the error fraction in the E91 key is exactly the background that decreases the visibility of polarization correlation measurements in section 2.3.

Although BB84 and E91 utilise different aspects of quantum mechanics, the security of their distributed key can be determined by looking only at the associated error fraction (sometimes known as the quantum bit error rate or QBER). For this reason both protocols were considered to be equivalent [151]. Entanglement was regarded simply as another source of correlations. This approach had practical benefits. The original protocol of BB84 involves an active choice when encoding the logical bits 0

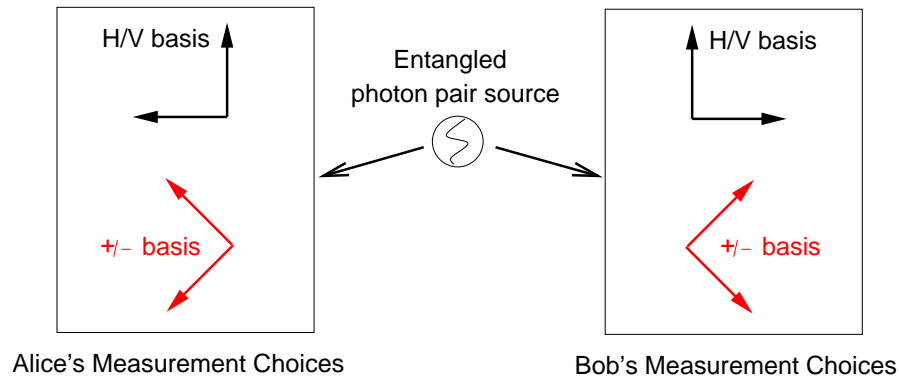


Figure 8.2: Schematic for an entanglement-based QKD protocol. Alice and Bob share a stream of polarization-entangled photon pairs. Unlike BB84, they only have to choose the measurement basis. Half the time their choices coincide, in which case a random encryption key can be derived. The remaining cases are discarded. The polarization state of individual photons are not determined until measurement, and are said to lack “an element of reality”.

and 1 into the polarization states, requiring a trusted high-bandwidth random number source [152]. In comparison no active choice is necessary for entanglement-based QKD. Hence the original attraction of entanglement was its ability to remove the need for some random number generators. The price of entanglement-based QKD is a lower key generation rate due to the limited brightness of contemporary entangled photon pair sources.

However, the notion that evidence of non-local correlations can be used to guarantee the security of an exchanged key remained alive. The idea was sometimes used qualitatively in QKD experiments. Consider the first report of a complete entanglement-based QKD system communicating over dedicated optical fibres by Jennewein et al. [54]. In that experiment a Bell-type inequality (known as the Wigner inequality) was monitored, and security was assumed when the inequality was violated. However, no quantitative measure of security (in terms of error fractions or otherwise) was obtained from the observed violation.

It is only recently that theoretical work by Acin et al. [153] has allowed a quantitative security measure to be obtained from a Bell inequality. In particular, they showed that the information accessible to an eavesdropper, I_E , can be derived from the degree of

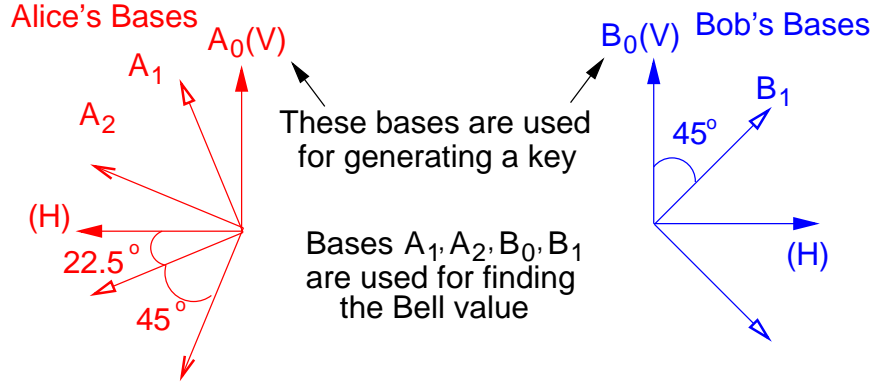


Figure 8.3: Orientation of different detector polarizations.

violation of the CHSH inequality, S with the following relationships:

$$I_E = h\left(\frac{1 + \sqrt{(S/2)^2 - 1}}{2}\right), \quad h(x) = -x \log_2(x) - (1-x) \log_2(1-x). \quad (8.1)$$

This chapter describes an entanglement-based QKD experiment that implements the Acin proposal. Not only is the experiment novel, it is also in a sense, the first complete implementation of QKD which is in the spirit of E91 ¹.

8.2 Experiment

8.2.1 Monitoring polarization states

The key idea behind the implementation is to use a minimal combination of three polarization bases A_0, A_1, A_2 on one side, and two distinct bases B_0, B_1 on the other side (figure 8.3) for performing polarization measurements on a photon pair in a singlet state $|\Psi^-\rangle = \frac{1}{\sqrt{2}}(|H_A V_B\rangle - |V_A H_B\rangle)$.

For convenience states in basis B_0 and B_1 are labeled as $1', 2'$ and $3', 4'$ respectively while states in basis A_0, A_1 and A_2 are labeled as $1, 2, 3, 4, 5$ and 6 . The bases were chosen so as to give us two sets of correlations; one of them is to be kept aside for deriving a key while the other set should be used to calculate the two-party CHSH value denoted as S . To fulfill this aim at least one pair of the bases must be identical.

¹The experiment was a team effort, and my principal co-workers were Ivan Marcikic, Matthew Peloso, Loh Huan Qian, Antia Lamas-Linares and Christian Kurtsiefer, with theoretical support provided by Valerio Scarani.

In the experiment this is supplied by the base pair A_0 and B_0 which correspond to the HV polarization basis (and states 1 and 1' are identified with the $|V\rangle$ state while 2 and 2' are identified with $|H\rangle$). In the absence of noise, coincidences in this pair of bases should lead to a perfectly anti-correlated measurement result, i.e. coincidences should happen such that state 1 occurs with state 2' and 2 occurs with 1'. Hence, correlations in this base pair are used to generate a key.

The remaining base combinations of A_1 and A_2 on one side with B_0 and B_1 on the other side are chosen such that the CHSH inequality can be tested. I will not derive the CHSH inequality here but refer the reader to chapter 20 of [154]. For our purposes, it is sufficient to note that the CHSH value is determined using four correlation coefficients E such that:

$$S = E(A_1, B_0) + E(A_1, B_1) + E(A_2, B_0) - E(A_2, B_1). \quad (8.2)$$

When only classical correlations exist then $|S| \leq 2$. The experimental value of the correlation coefficient $E(x, y)$ may be defined as:

$$E(x, y) = \frac{n_{x+y_+} + n_{x-y_-} - n_{x+y_-} - n_{x-y_+}}{n_{x+y_+} + n_{x-y_-} + n_{x+y_-} + n_{x-y_+}}. \quad (8.3)$$

The expression $n_{i,j}$ refers to the number of coincidence events between detectors monitoring state i on one side and state j on the other side, collected during a given integration time T .

Measurement bases are chosen such that a maximal violation of equation (8.2) with $|S| = 2\sqrt{2}$ could be expected. Therefore, basis B_1 has to be chosen to correspond to $\pm 45^\circ$ linear polarization, and bases A_1, A_2 need to form an orthogonal set corresponding to $\pm 22.5^\circ, \pm 67.5^\circ$ linear polarizations (figure 8.3). With that, we evaluate for example

$$\begin{aligned} E(A_1, B_0) &= \frac{n_{3,2'} + n_{4,1'} - n_{3,1'} - n_{4,2'}}{n_{3,2'} + n_{4,1'} + n_{3,1'} + n_{4,2'}} \\ &= \frac{n_{67.5^\circ, V} + n_{-22.5^\circ, H} - n_{67.5^\circ, H} - n_{-22.5^\circ, V}}{n_{67.5^\circ, V} + n_{-22.5^\circ, H} + n_{67.5^\circ, H} + n_{-22.5^\circ, V}}, \end{aligned} \quad (8.4)$$

and the other coefficients in equation (8.2) accordingly.

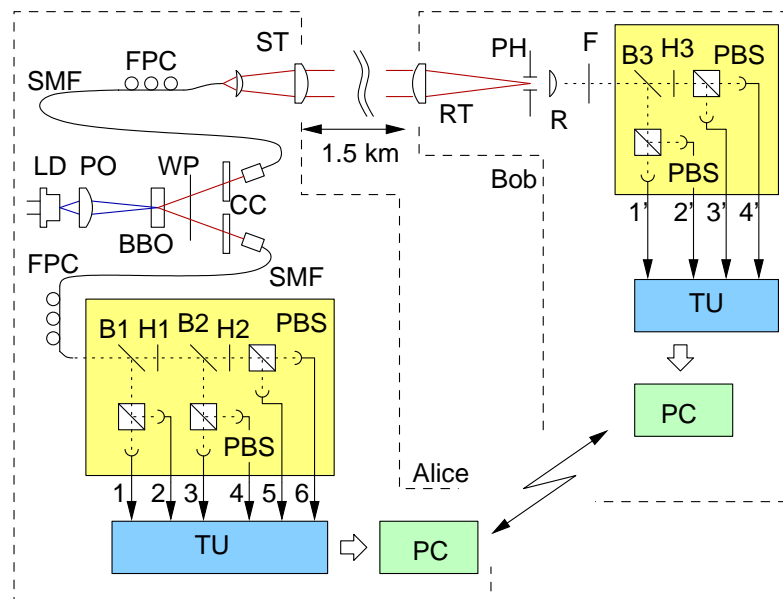


Figure 8.4: Experimental QKD setup. Polarization-entangled photon pairs are generated via parametric downconversion pumped by a laser diode (LD, PO) in a nonlinear optical crystal (BBO) with walk-off compensation (WP, CC) into single mode optical fibers (SMF). A free-space optical channel for one detector set (Bob) is realized using small telescopes on both sides (ST, RT) with some spatial and spectral filtering (PH, F). Both parties perform polarization measurements in bases randomly chosen by beam splitters (B1-B3), and defined by properly oriented wave plates (H1-H3) in front of polarizing beam splitters (PBS) and photon counting detectors. Photo events are registered separately with time stamp units (TU) connected to two personal computers (PC) linked via a classical channel.

The random choice of measurement bases on each side is performed with a combination of polarization-independent beam splitters (B1-B3, figure 8.4), with a 50:50 splitting ratio. This provides a base choice without an explicit generation of a random number by a device not necessarily trusted. The dichotomic variables in each basis setting corresponding to the angle setting shown in figure 8.3 is defined with half wave plates with appropriate orientations of their optical axes (H1 at 11.25° , H2 and H3 at 22.5°) with respect to the vertical direction. The remaining elements of the experiment are a compact source of entangled-photon pairs, and the software to detect coincidences and distill a secure key [113].

8.2.2 A compact SPDC source

Polarization-entangled photon pairs are generated in a compact diode-laser pumped non-collinear type-II parametric downconversion process, based on the source described in chapter 2. The entire source was mounted on either side of a breadboard in order to reduce its size ($80 \times 50 \times 60 \text{ cm}^3$). Figure 8.5 displays side and top views of the experimental source.

The laser diode produced a pump beam whose wavelength was 407 nm at a power of 40 mW. The beam is used to pump a 2 mm thick β -Barium Borate (BBO) crystal. Typically, the visibility of polarization correlations (section 2.3) from such a source does not exceed 92%. This is due to the broad spectrum of the pump wavelength which is revealed in the polarization dependent coincidence spectra shown in figure 8.6.

8.2.3 Experimental results

To demonstrate a key generation scenario under realistic conditions, we separated the two measurement devices by approximately 1.5 km. This introduced a link loss of about 3 dB caused primarily by atmospheric absorption at the downconverted wavelength of 810 nm and realistic fluctuations in the transmission due to scintillation in the atmosphere. The experiment was carried out during night time to reduce the influence of background light. Additional background light suppression was accomplished using a spatial filter (PH) with an acceptance range of $\Omega = 2 \cdot 10^{-8} \text{ sr}$ and an interference filter

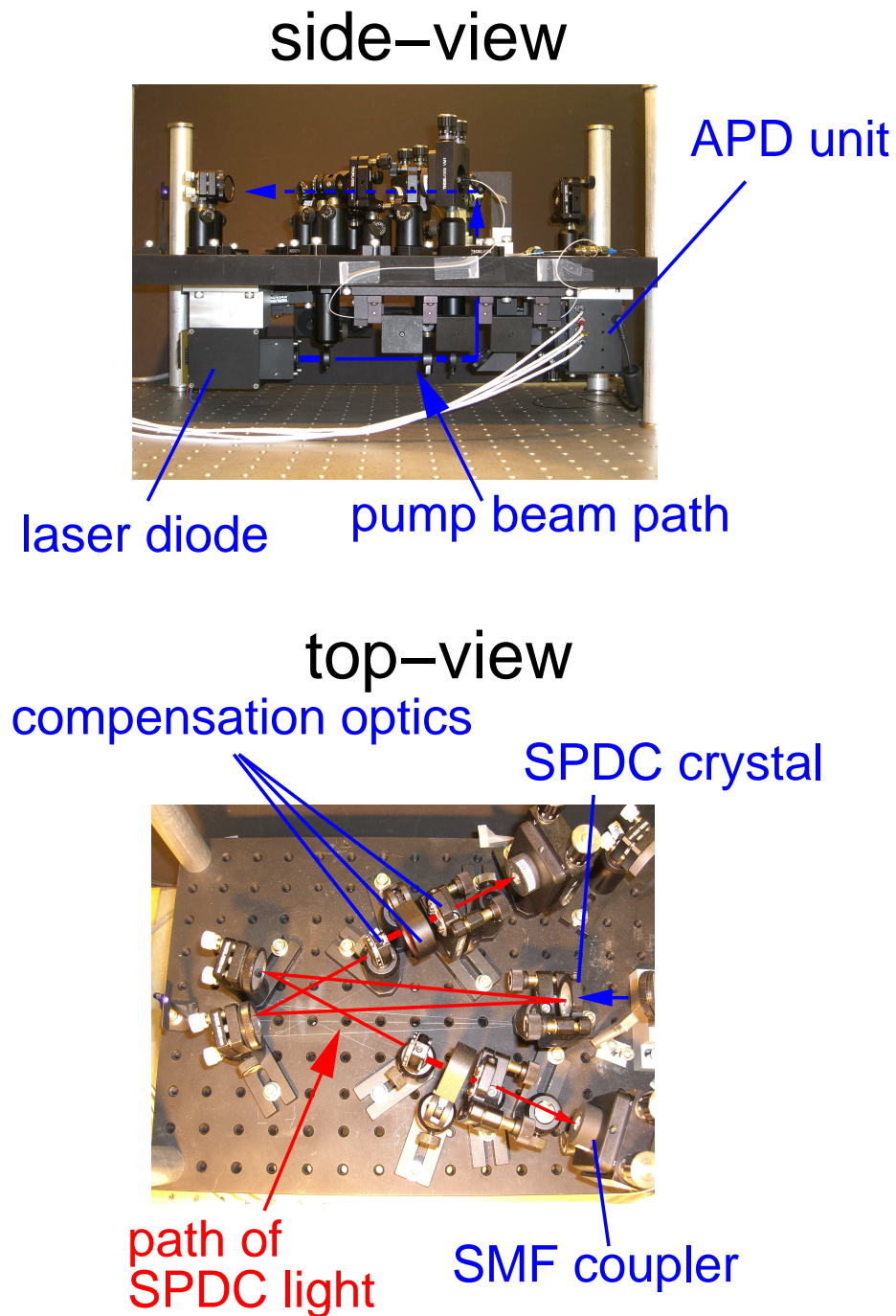


Figure 8.5: Compact source of entangled photon pairs. This was the diode-pumped source that supplied entangled photon pairs for the QKD demonstration. The pump beam profile is corrected in the lower deck (using anamorphic prisms) and then sent to the SPDC crystal in the upper deck. To restrict footprint of the source further, the downconverted light is reflected into the compensation optics and single mode fiber couplers. The apparatus was mounted on a breadboard drilled with holes that are spaced 1 inch apart. This source was first built by Antia Lamas-Linares and Loh Huan Qian.

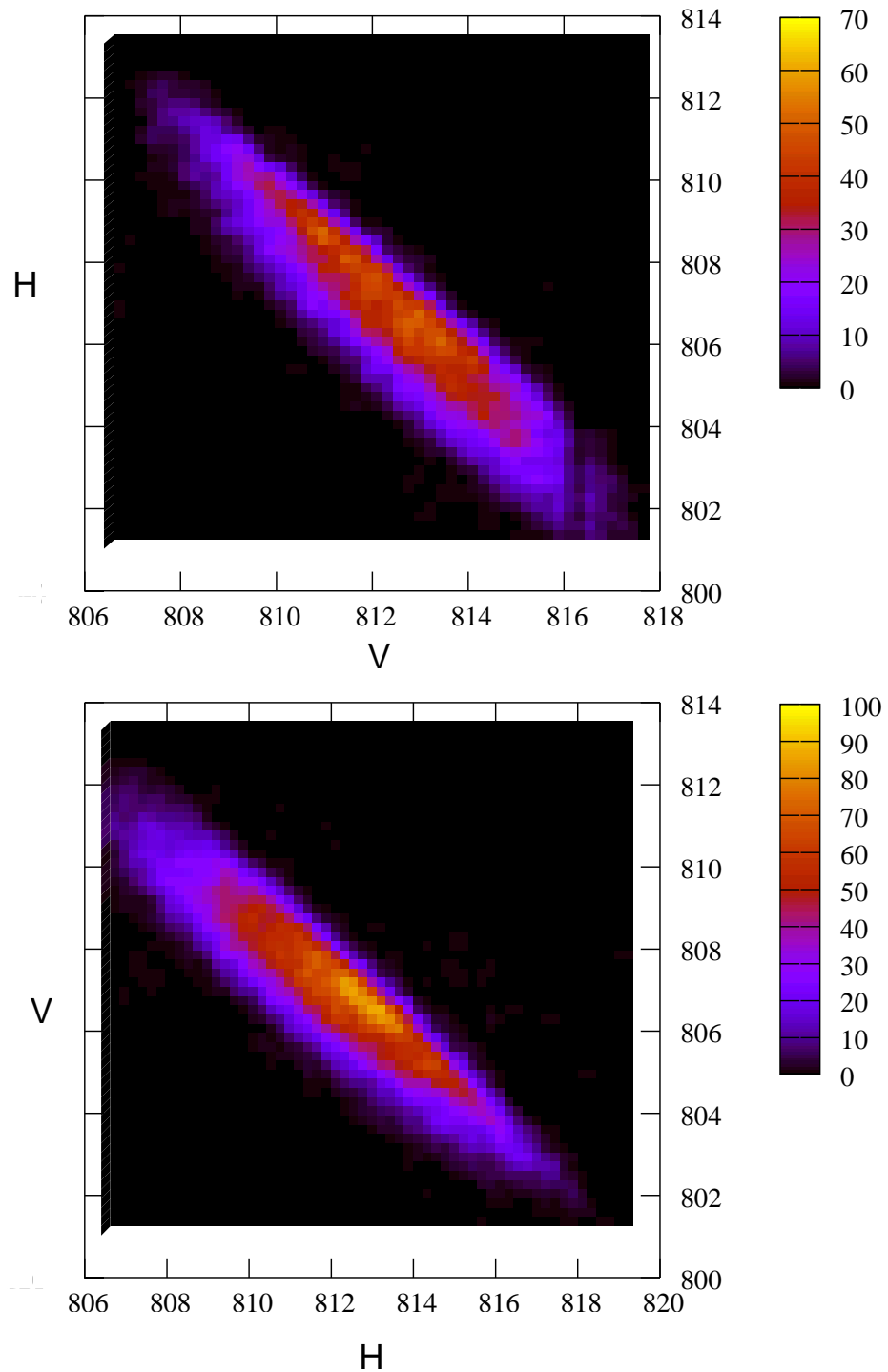


Figure 8.6: Coincidence spectrum of collected photon pairs from the diode pumped source. The spectra were measured after the photon pairs had passed through horizontal (H) and vertical (V) polarization filters. The measurements reveal that the polarization of the photon pairs may be distinguished from their spectra. These measurements were carried out by Loh Huan Qian.

with a peak transmission of 50% and a spectral width of 4.5 nm (FWHM) around the center wavelength of 810 nm.

Identification of coincidence events between both sides was performed during the experiment in software from a list of detection times registered by a time stamp unit with respect to local reference clocks. The corresponding coincidence time window for that scheme was chosen to be 3.75 ns, supplying additional suppression of accidental coincidences.

The experimental results from one typical 8 hour run are shown in figure 8.7. For the entire test run, the correlation value S remained at approximately 2.5, well clear of the value $S = 2$ at which no secure key can be distilled. The corresponding error fraction (QBER) in this experiment was approximately 4%. Error correction was performed (using the Cascade protocol [155]) on blocks of raw key of at least 10000 bits collected within 3 seconds. Hence, a final secure key was obtained at an average rate of 350 bits s^{-1} . The results show that a secure key was distributed over 1.5 km of free space via an E91 protocol.

8.3 Extending QKD beyond BB84

It is interesting to consider if this experiment constitutes a ‘device-independent’ QKD demonstration [153], where source and detection apparatus may be released into the control of an untrusted party. The answer is no. True device-independent QKD is possible only if the measured CHSH inequality represents irrefutable proof of entanglement. A Bell test using contemporary devices allows for loopholes (e.g. the detection loophole due to low detector quantum efficiency) where it may be argued that factors other than entanglement caused the apparent violation. Such loopholes may only be closed using assumptions (e.g. fair sampling) that hold when the devices are under careful control. Hence, while device-independent QKD is allowed in principle, it cannot yet be implemented with contemporary technology.

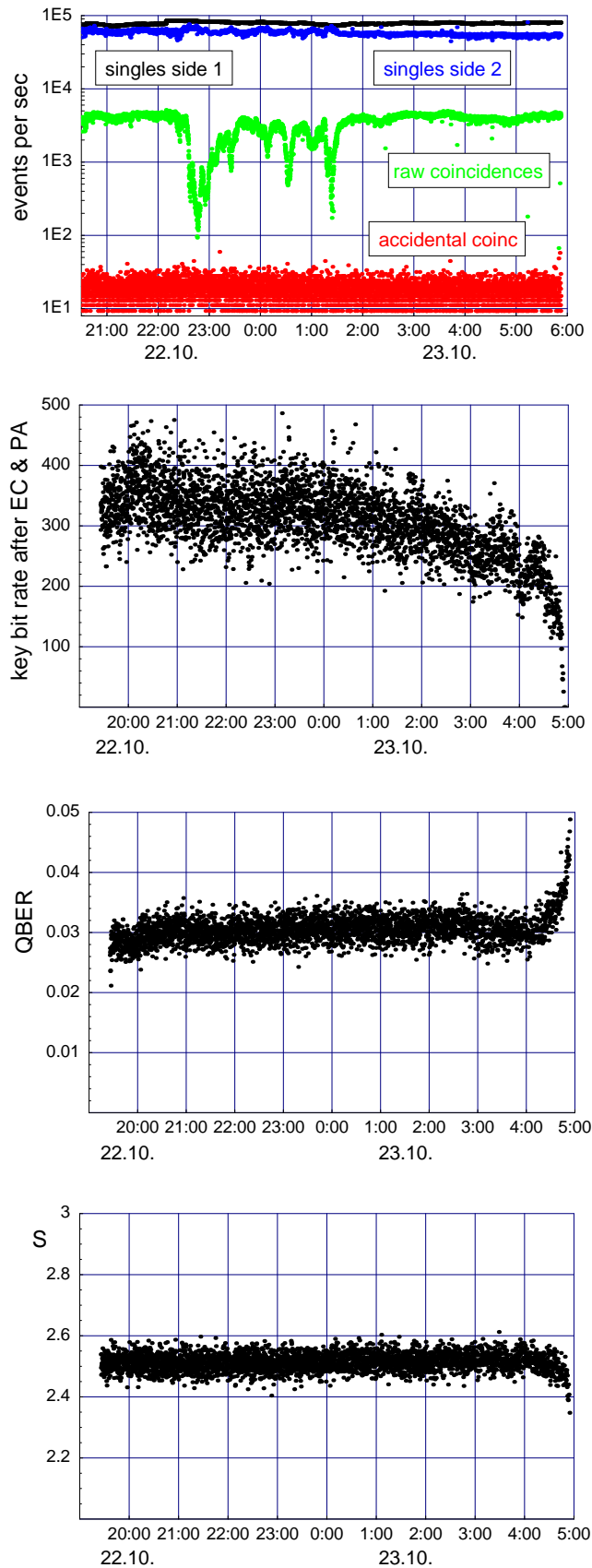


Figure 8.7: Experimental results in a key distribution experiment implementing an E91 protocol. The experiment ran for 8 hours until sunrise, when excessive background light caused too many accidental coincidences to be detected. In panel 2, the abbreviations EC and PA stand for Error Correction and Privacy Amplification respectively.

Chapter 9

Experimental Falsification of the Leggett Non-local Variable Model

In this penultimate chapter, we will turn our attention to a fundamental question about the nature of entanglement. In particular, I want to describe an experiment that tested whether the quantum correlations between polarization-entangled photon pairs could be described by a physical model of photon pairs where the individual polarization states are retained. The concept that individual particles must have a well defined state comes from classical physics. This concept was described by the EPR trio as “an element of reality” [32]. In the EPR formulation, each “element of reality” must be a local variable¹. In the context of light polarization, it is taken to mean that individual photons exist in a pure polarization state.

However, according to the rules of quantum mechanics, photons in a polarization-entangled state lose this “element of reality”. The state of individual photons that are polarization-entangled is not well-defined unless when considered together with their entangled partner. Correlations from entangled photon pairs cannot be replicated by pairs of photons that share only local variables, and this has since been confirmed experimentally with violations of the Bell inequality.

The question then becomes the following: can entanglement type correlations be explained by particles that share non-local variables? In 2003, Anthony Leggett suggested

¹As stated in chapter 1, EPR’s concept of locality is a conjunction of special relativity as well as additional classical assumptions about “completeness” in describing physical states [41].

that there was one way to rule out a particular class of models that use non-local variables. Specifically, Leggett proposed to check whether entanglement-type correlations could be given by a pair of spin-polarized particles that communicated in a non-local manner [156].

In the context of light polarization, this is a very special type of model where individual photons retain their “element of reality” (i.e. pure polarization state) but had access to (as yet unknown) non-local variables that established the inter-photon correlations. Leggett showed that such a physical model could not reproduce all the correlations predicted by quantum mechanics. Similar to Bell’s theorem, Leggett showed that inter-photon correlations from his non-local variable model never exceeded a bound. This bound can be tested in the form of an inequality (similar to Bell’s inequality), and is now known as Leggett’s inequality.

Experimentally, a violation of Leggett’s inequality is more demanding than Bell’s because of the higher entanglement quality that is necessary. The first experiment in this direction was by Gröblacher et al. who showed that contemporary SPDC sources provided polarization-entangled photon pairs of sufficient quality [47]. Motivated by this work and a simplified theoretical derivation by Cyril Branciard, Nicolas Gisin and Valerio Scarani, my supervisors and I performed an experiment to violate the Leggett inequality. The results have been published together with Branciard et al. in [48]. The remaining material in this chapter was adapted from that paper with very few changes.

9.1 Introduction

Quantum physics provides a precise rule to compute the probability that the measurement of A and B performed on two physical systems in the state $|\Psi\rangle$ will lead to the outcomes (r_A, r_B) :

$$P_Q(r_A, r_B|A, B) = \langle \Psi | \mathcal{P}_{r_A} \otimes \mathcal{P}_{r_B} | \Psi \rangle \quad (9.1)$$

where \mathcal{P}_r is the projector on the subspace associated to the measurement result r . For entangled states, this formula predicts that the outcomes are correlated, irrespective of the distance between the two measurement devices. Indeed, this was the puzzle

presented by the trio of Einstein, Podolsky and Rosen [32].

A natural explanation for correlations established at a distance is pre-established agreement: the two particles have left the source with some common information λ , called a local variable (LV), that allows them to compute the outcomes for each possible measurement; formally, $r_A = f_A(A, \lambda)$ and $r_B = f_B(B, \lambda)$. The shared information are sometimes called local *hidden* variables because in principle they can exert an influence, even when they are not known.

Satisfactory as it may seem a priori, this model fails to reproduce all quantum correlations: this is the celebrated result of John Bell [35], by now tested in a very large number of experiments. The fact that quantum correlations can be attributed neither to LV nor to communication below the speed of light is referred to as *quantum non-locality*.

While non-locality is a striking manifestation of quantum entanglement, it is not yet clear how fundamental this notion really is: the essence of quantum physics may be somewhere else [157]. For instance, non-determinism is another important feature of quantum physics, with no a priori link with non-locality. Generic theories featuring both non-determinism and non-locality have been studied, with several interesting achievements (e.g. [158, 159]); but it is not yet clear what singles quantum physics out. In order to progress in this direction, it is important to learn which other alternative models are compatible with quantum physics, which are not. Bell's theorem having ruled out all possible LV models, we have to move on to models based on *non-local variables* (NLV). The first example of a testable NLV model was the one by Suarez and Scarani [160], falsified in a series of experiments a few years ago [161]. A different such model was proposed more recently by Leggett [156]. This model supposes that the source emits product quantum states $|\alpha\rangle \otimes |\beta\rangle$ with probability density $\rho(\alpha, \beta)$, and enforces that the marginal probabilities must be compatible with such states:

$$P(r_A|A) = \int d\rho(\alpha, \beta) \langle \alpha | \mathcal{P}_{r_A} | \alpha \rangle, \quad (9.2)$$

$$P(r_B|B) = \int d\rho(\alpha, \beta) \langle \beta | \mathcal{P}_{r_B} | \beta \rangle. \quad (9.3)$$

The correlations however must include some non-local effect, otherwise this would be a (non-deterministic) LV model and would already be ruled out by Bell's theorem. What Leggett showed is that the simple requirement of consistency (i.e., no negative probabilities should appear at any stage) constrains the possible correlations, even non-local ones, to satisfy inequalities that are slightly but clearly violated by quantum physics. A recent experiment [47] demonstrated that state-of-the-art setups can detect this violation in principle. However, their falsification of the Leggett model is flawed by the need for additional assumptions, because the inequality they used, just as the original one by Leggett, supposes that data are collected from infinitely many measurement settings.

In this chapter, we present a family of inequalities, which allow testing Leggett's model against quantum physics with a finite number of measurements. We show their experimental violation by pairs of polarization-entangled photons. We conclude with an overview of what has been learned and what is still to be learned about NLV models.

9.2 Theory

We restrict our theory to the case of polarization-based qubits. We consider von Neumann measurements, that can be labeled by unit vectors in the Poincaré sphere \mathcal{S} : $A \rightarrow \vec{a}$ and $B \rightarrow \vec{b}$; their outcomes will be written $r_A, r_B \in \{+1, -1\}$. Pure states of single particles can also be labeled by unit vectors \vec{u}, \vec{v} in \mathcal{S} . Leggett's model requires²

$$P(r_A, r_B | \vec{a}, \vec{b}) = \int d\rho(\vec{u}, \vec{v}) P_{\vec{u}, \vec{v}}(r_A, r_B | \vec{a}, \vec{b}) \quad (9.4)$$

with

$$P_{\vec{u}, \vec{v}}(r_A, r_B | \vec{a}, \vec{b}) = \frac{1}{4} \left[1 + r_A \vec{a} \cdot \vec{u} + r_B \vec{b} \cdot \vec{v} + r_A r_B C(\vec{u}, \vec{v}, \vec{a}, \vec{b}) \right]. \quad (9.5)$$

The correlation coefficient $C(\vec{u}, \vec{v}, \vec{a}, \vec{b})$ is constrained only by the requirement that (9.5) must define a probability distribution over (r_A, r_B) for all choice of the measurements

²The specific form of the marginal distributions is called *Malus' law* in the case of polarization.

\vec{a}, \vec{b} . Remarkably, this constraint is sufficient to derive inequalities that can be violated by quantum physics [156]. The inequality derived (see also [162] for a subsequent shorter derivation) reads

$$|E_1(\varphi) + E_1(0)| + |E_2(\varphi) + E_2(0)| \leq 4 - \frac{4}{\pi} \left| \sin \frac{\varphi}{2} \right| \quad (9.6)$$

where the quantities $E_j(\theta)$ are defined from the correlation coefficients

$$C(\vec{a}, \vec{b}) = \sum_{r_A, r_B} r_A r_B P(r_A, r_B | \vec{a}, \vec{b}) \quad (9.7)$$

as follows. The index j refers to a plane $\{\vec{a} \in \mathcal{S} | \vec{a} \cdot \vec{n}_j = 0\}$ in the Poincaré sphere (for $\vec{n}_j \in \mathcal{S}$), and the two planes $j = 1, 2$ that appear in (9.6) must be orthogonal (i.e. $\vec{n}_1 \cdot \vec{n}_2 = 0$). For each unit vector \vec{a}_j of plane j , let's define $\vec{a}_j^\perp = \vec{n}_j \times \vec{a}_j$. $E_j(\theta)$ is then the average of $C(\vec{a}_j, \vec{b}_j)$ over *all* directions \vec{a}_j , with $\vec{b}_j = \cos \theta \vec{a}_j + \sin \theta \vec{a}_j^\perp$ ³. This is a problematic feature of inequality (9.6): it can be checked only by performing an infinite number of measurements or by adding the assumption of rotational invariance of the correlation coefficients $C(\vec{a}, \vec{b})$, as in [47]. It is thus natural to try and replace the average over all possible settings with an average on a discrete set. This is done by the following estimate. Let \vec{w} and \vec{c} be two unit vectors, and let R_N be the rotation by $\frac{\pi}{N}$ around the axis orthogonal to (\vec{w}, \vec{c}) . Then

$$\frac{1}{N} \sum_{k=0}^{N-1} \left| (R_N^k \vec{c}) \cdot \vec{w} \right| \geq u_N = \frac{1}{N} \cot \frac{\pi}{2N}. \quad (9.8)$$

Indeed, let $\tilde{\xi}$ be the angle between \vec{w} and \vec{c} , and $\xi = (\tilde{\xi} - \frac{\pi}{2}) \bmod \frac{\pi}{N}$, such that $\xi \in [0, \frac{\pi}{N}[$: then it holds $\sum_{k=0}^{N-1} |(R_N^k \vec{c}) \cdot \vec{w}| = \sum_{k=0}^{N-1} |\cos(\tilde{\xi} + \frac{k\pi}{N})| = \sum_{k=0}^{N-1} \sin(\xi + \frac{k\pi}{N}) = \sin \xi + Nu_N \cos \xi \geq Nu_N$ as announced.

Replacing the full average by the discrete average (9.8) in the otherwise unchanged

³This step is taken after (27) in the supplementary information for [47], before (8) in [162]. The derivation of the original inequalities goes through the same step between (3.9) and (3.10) in [156].

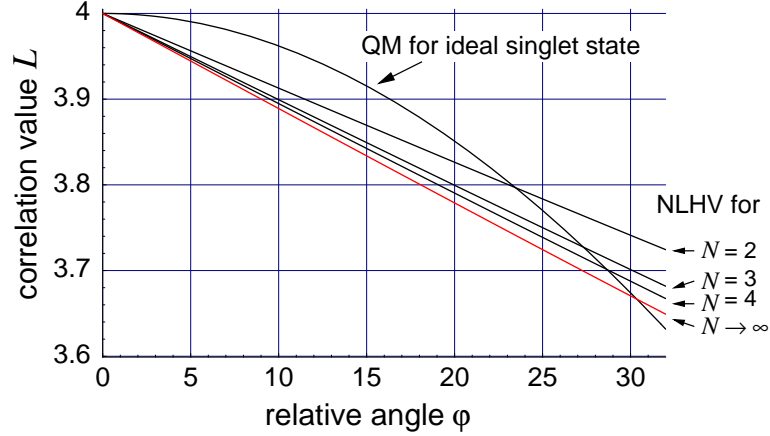


Figure 9.1: Dependency of the combined correlation parameters $L(\varphi)$ as a function of the separation angle φ for the quantum mechanical prediction for a pure singlet state, and bounds for non-local variable models assuming an averaging over various numbers of directions N . This figure is adapted from reference [48].

proofs [162], we obtain the following family of inequalities:

$$\begin{aligned} |E_1^N(\vec{a}_1, \varphi) + E_1^N(\vec{a}_1, 0)| + |E_2^N(\vec{a}_2, \varphi) + E_2^N(\vec{a}_2, 0)| \\ \equiv L_N(\vec{a}_1, \vec{a}_2, \varphi) \leq 4 - 2u_N \left| \sin \frac{\varphi}{2} \right| \end{aligned} \quad (9.9)$$

where

$$E_j^N(\vec{a}_j, \theta) = \frac{1}{N} \sum_{k=0}^{N-1} C(\vec{a}_j^k, \vec{b}_j^k) \quad (9.10)$$

with $\vec{b}_j = \cos \theta \vec{a}_j + \sin \theta \vec{a}_j^\perp$ and the notation $\vec{c}^k = (R_{N,j})^k \vec{c}$ (the $\frac{\pi}{N}$ -rotation is along \vec{n}_j). This defines $2N$ and $4N$ settings on each side. For a pure singlet state, the quantum mechanical prediction for $L_N(\vec{a}_1, \vec{a}_2, \varphi)$ is

$$L_{\Psi^-}(\varphi) = 2(1 + \cos \varphi) \quad (9.11)$$

independent of N and of the choice of \vec{a}_1, \vec{a}_2 since the state is rotationally invariant.

The inequality for $N = 1$ cannot be violated because $u_1 = 0$ ⁴. Already for $N = 2$,

⁴Actually, the data measured on a singlet state for $N = 1$, as in [47], can be reproduced by the explicit NLV Leggett-type model presented in [47]. Indeed, the validity condition for that NLV model is that there exists unit vectors \vec{u}, \vec{v} in the Poincaré sphere such that, for all pairs of observables \vec{a}, \vec{b} measured in the experiment, one has $|\vec{a} \cdot \vec{b} \pm \vec{u} \cdot \vec{a}| \leq 1 \mp \vec{v} \cdot \vec{b}$ (Eq. (10) of [47]) or, equivalently, $|\vec{a} \cdot \vec{b} \pm \vec{v} \cdot \vec{b}| \leq 1 \mp \vec{u} \cdot \vec{a}$.

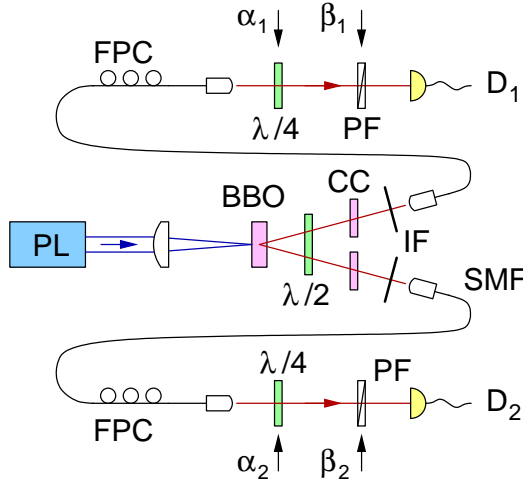


Figure 9.2: Experimental setup to test Leggett's Inequality. Polarization-entangled photon pairs are generated in β -barium-borate (BBO) by parametric downconversion of light from an Ar ion pump laser (PL). After walk-off compensation ($\lambda/2$, CC), down-converted light is collected behind interference filters (IF) into birefringence-compensated (FPC) single mode optical fibers (SMF). Polarization measurements are carried out with a combination of a quarter wave plate ($\lambda/4$) and polarization filters (PF) in front of photon counting detectors $D_{1,2}$. The measurement basis for each arm (1,2) is chosen by rotation of the wave plate and polarizing filter by angles $\alpha_{1,2}, \beta_{1,2}$ accordingly. This figure is adapted from reference [48].

however, quantum physics violates the inequality: this opens the possibility for our falsification of Leggett's model without additional assumptions⁵. For $N \rightarrow \infty$, $u_N \rightarrow \frac{2}{\pi}$: one recovers inequality (9.6). The suitable range of difference angles φ for probing a violation of the inequalities (9.9) can be identified from figure 9.1. The largest violation for an ideal singlet state would occur for $|\sin \frac{\varphi}{2}| = \frac{u_N}{4}$, i.e. at $\varphi = 14.4^\circ$ for $N = 2$, increasing with N up to $\varphi = 18.3^\circ$ for $N \rightarrow \infty$.

9.3 Experiment

We begin with our implementation of the fiber-coupled parametric downconversion source for polarization-entangled photon pairs described in section 2.2. In order to avoid a modulation of the collection efficiency with optical components due to wedge errors in the wave plates, we placed subsequent polarization analyzing elements behind

Now, for the case $N = 1$, one would measure four sets of observables $\vec{a}_j, \vec{b}_j = \cos \theta \vec{a}_j + \sin \theta \vec{a}_j^\perp$ in planes $j = 1, 2$ and for $\theta = 0, \varphi$. Then for $\vec{u} = -\vec{v}$ orthogonal to both \vec{a}_1^\perp and \vec{a}_2^\perp and whatever θ , one has $|\vec{a}_j \cdot \vec{b}_j \pm \vec{v} \cdot \vec{b}_j| = |\cos \theta \mp \vec{u} \cdot (\cos \theta \vec{a}_j + \sin \theta \vec{a}_j^\perp)| = |\cos \theta (1 \mp \vec{u} \cdot \vec{a}_j)| \leq 1 \mp \vec{u} \cdot \vec{a}_j$ as required.

⁵Note that, since the model under test is NLV, there are no such concerns as locality or memory loopholes. The detection loophole is obviously still open.

the fiber.

The projective polarization measurements for the different settings of the two observers were carried out using quarter wave plates, rotated by motorized stages by respective angles $\alpha_{1,2}$, and absorptive polarization filters rotated by angles $\beta_{1,2}$ in a similar way with an accuracy of 0.1 degree. This combination allows to project on arbitrary elliptical polarization states. Finally, the source was adjusted to produce photon pairs in a singlet state.

After birefringence compensation of the optical fibers, we observed the corresponding polarization correlations between both arms with a visibility of $99.5 \pm 0.2\%$ in the H - V basis, $99.0 \pm 0.2\%$ in the $\pm 45^\circ$ linear basis, and $98.2 \pm 0.2\%$ in the circular polarization basis. Typical count rates were 10100 s^{-1} and 8000 s^{-1} for single events in both arms, and about 930 s^{-1} for coincidences for orthogonal polarizer positions. We measured an accidental coincidence rate using a delayed detector signal of $0.41 \pm 0.07 \text{ s}^{-1}$, corresponding to a time window of 5 ns.

The two orthogonal planes we used in the Poincaré sphere included all the linear polarizations for one, and H - V linear and circular polarizations for the other. That way, we intended to take advantage of the better polarization correlations in the 'natural' basis H - V for the downconversion crystal. Each of the $4N$ correlation coefficients $C(\vec{a}, \vec{b})$ in (9.9,9.10) was obtained from four settings of the polarization filters via

$$C(\vec{a}, \vec{b}) = \frac{n_{\vec{a},\vec{b}} + n_{-\vec{a},-\vec{b}} - n_{-\vec{a},\vec{b}} - n_{\vec{a},-\vec{b}}}{n_{\vec{a},\vec{b}} + n_{-\vec{a},-\vec{b}} + n_{-\vec{a},\vec{b}} + n_{\vec{a},-\vec{b}}} \quad (9.12)$$

from the four coincident counts $n_{\pm\vec{a},\pm\vec{b}}$ obtained for a fixed integration time of $T = 4 \text{ s}$ each. For $N = 2, 3$ and 4, we carried out the full generic set of 8, 12, and 16 setting groups, respectively, with each $E_j^N(0)$ containing a H - V analyzer setting.

A summary of the values of L corresponding to inequalities for $N = 2, 3$ and 4 are shown in Fig. 9.3, together with the corresponding bounds (9.9) and the quantum expectation for a pure singlet state (9.11). The corresponding standard deviations in the results were obtained through usual error propagation assuming Poissonian counting statistics and independent fluctuations on subsequent settings. For $N = 2$, we already observe a clear violation of the NLV bound; the largest violation we found was for

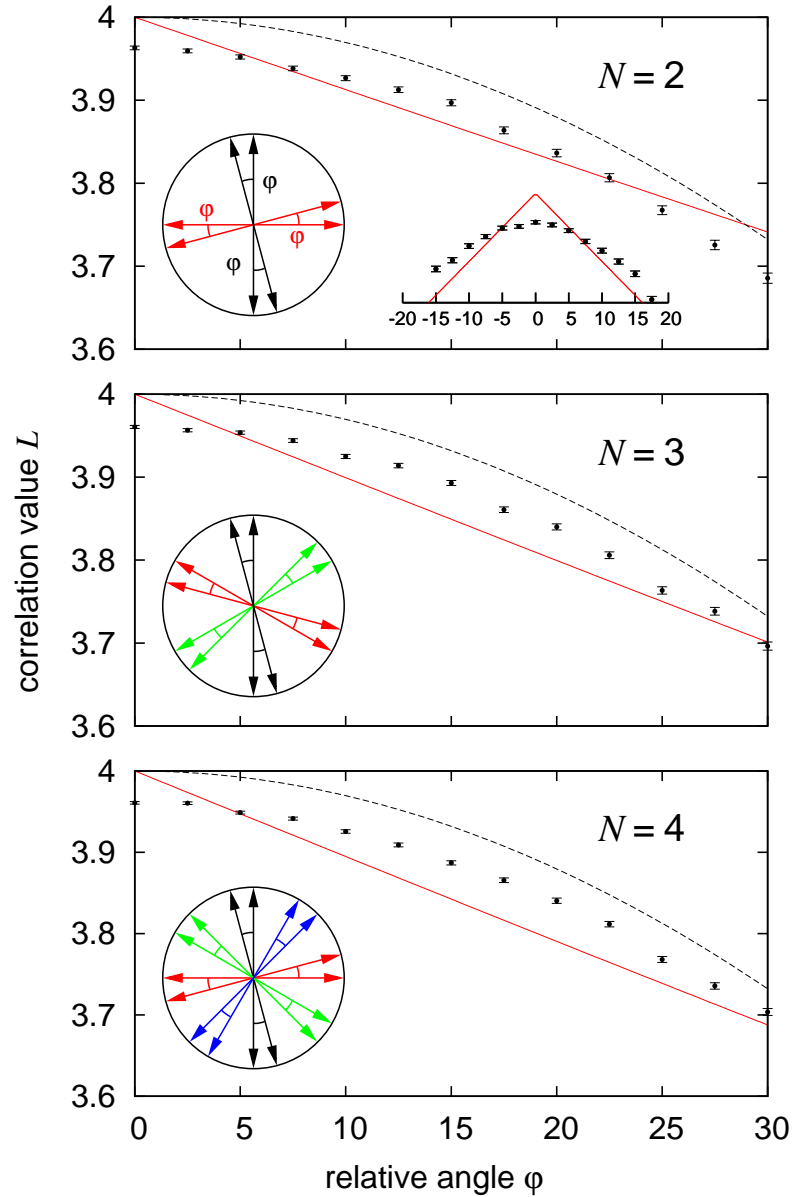


Figure 9.3: Experimental results for the observed correlation parameters L_N (dots), the quantum mechanical prediction for a pure singlet state (curved lines, dashed), and the bounds for the non-local variable models (almost straight lines). In all cases, our experiment exceeds the NLV bounds for appropriate difference angles φ . This figure is adapted from reference [48].

N	φ	L_{NLV}	$L_{\text{exp}} \pm \sigma$	$L_{\text{exp}} - L_{\text{NLV}}$
2	12.5°	3.8911	3.9127 ± 0.0033	6.45σ
2	15°	3.8695	3.8970 ± 0.0036	7.59σ
2	17.5°	3.8479	3.8638 ± 0.0042	3.83σ
3	12.5°	3.8743	3.9140 ± 0.0027	14.77σ
3	15°	3.8493	3.8930 ± 0.0030	14.58σ
3	17.5°	3.8243	3.8608 ± 0.0034	10.67σ
3	20°	3.7995	3.8400 ± 0.0036	11.15σ
4	12.5°	3.8686	3.9091 ± 0.0024	17.01σ
4	15°	3.8424	3.8870 ± 0.0026	16.84σ
4	17.5°	3.8164	3.8656 ± 0.0029	17.11σ

Table 9.1: Selected values of L violating the NLV bounds L_{NLV} for different averaging numbers N .

$N = 4$ with about 17 standard deviations above the NLV bound. As expected, the experimental violation increases with growing number of averaging settings N . Selected combinations of (N, φ) violating NLV bounds are summarized in table 9.1.

Our results are well-described assuming residual colored noise in the singlet state preparation [144]. We attribute the small asymmetry of L_{exp} in φ (see inset in Fig. 9.3) to polarizer alignment accuracy.

9.4 Overview and Perspectives

After the very general motivation sketched in the introduction, we have focused on Leggett’s model. Let’s now set this model in a broader picture. Non-locality having been demonstrated, the only classical mechanism left to explain quantum correlations is the exchange of a signal. It is therefore natural to assume, as an alternative model to quantum physics, that the source produces independent particles, which later exchange some communication.

This communication should travel faster than light, so the model has to single out the frame in which this signal propagates: it can be either a preferred frame (“quantum ether”), in which case even signaling is not logically contradictory [163]; or a frame defined by the measuring devices, in which case the model departs from the quantum predictions when the devices are set in relative motion [160, 161]. Obviously, there are NLV models that do reproduce exactly the quantum predictions. Explicit examples

are Bohmian Mechanics [164] and, for the case of two qubits, the Toner-Bacon model [165]. Both are deterministic. Now, in Bohmian mechanics, if the first particle to be measured is A, then assumption (9.2) can be satisfied, but assumption (9.3) is not. This remark sheds a clearer light on the Leggett model, where both assumptions are enforced: the particle that receives the communication is allowed to take this information into account to produce non-local correlations, but it is also required to produce outcomes that respect the marginals expected for the local parameters alone.

As a conclusion, it must be said that the broad goal sketched in the introduction, namely, to pinpoint the essence of quantum physics, has not been reached yet. However, Leggett's model and its conclusive experimental falsification reported here have added a new piece of information towards this goal.

Chapter 10

Final Remarks

This thesis has presented several results on the utility of bulk SPDC sources for entanglement-assisted quantum communication and fundamental tests of physics. In summary, the most important points are the following:

- A model giving the absolute rate of emission for fiber-coupled SPDC sources has been provided (chapter 3). This model shows that contemporary Kwiat95-type sources are operating near their optimal output.
- A minimal and optimal polarimetric technique was demonstrated for characterizing the polarization states of entangled photons (chapter 4). This method is easily extended to multi-photon states. It should be noted that the number of measurement outcomes grow exponentially with the number N of photons in the system (as 4^N). However, this is not as bad as it seems as the number of dimensions of the Hilbert space also grows exponentially with N , and the tetrahedron POVM is actually the most efficient method of state estimation that is possible with separable measurements.
- Fiber-coupled Kwiat95 type sources are able to give high quality entangled photon pairs at a reasonable rate, enabling very sensitive tests of quantum non-locality (chapter 9).
- Such sources can be miniaturized sufficiently, allowing them to be taken into the field to demonstrate advanced QKD protocols (chapter 8).

The model for absolute rate emission, in particular, has implications on the direction that future sources of entangled photons will take. In chapter 1 it was suggested that a future quantum communication network might employ atom-based memories and quantum repeaters. This requires light that is within a very narrow spectral bandwidth that should be on the order of tens of MHz.

As a comparison, consider that the spectral brightness of the source described in chapter 2 is about 4×10^{-4} pairs $\text{s}^{-1} \text{mW}^{-1} \text{MHz}^{-1}$. Based on the model presented in chapter 3, it is not expected that Kwiat95-type sources will become very much brighter. This is because the ultimate limit to the spectral brightness of bulk SPDC sources is determined only by longitudinal phase mismatch. For example, the strongest periodically poled SPDC source reported in literature is still “only” at a spectral brightness of 0.5 pairs $\text{s}^{-1} \text{mW}^{-1} \text{MHz}^{-1}$ [94]. A dramatic improvement to the photon pair rate (by several orders of magnitude) in an atomic bandwidth is not likely to be obtained from bulk SPDC crystals in a single pass pump configuration.

This is an important result, especially since spectral brightness (along with entanglement quality) will be increasingly used to evaluate entangled photon sources. Hence, although Kwiat95-type sources have a very high quality of entanglement, their generated photon pairs are not useful in advanced quantum communication protocols that require interaction with atom-like systems. To overcome this problem there are two possible strategies.

The first option is to perform SPDC in a confined volume as in a periodically poled waveguide. In such a confined volume, SPDC leads to a much higher observed spectral brightness of about 1.6 pairs $\text{s}^{-1} \text{mW}^{-1} \text{MHz}^{-1}$ as reported by Fiorentino et al. [95]. Furthermore, the same authors have estimated that with a properly designed waveguide, it is possible to achieve rate of about 2000 pairs $\text{s}^{-1} \text{mW}^{-1} \text{MHz}^{-1}$ [96]. This suggests that waveguide-based SPDC can generate enough photons to saturate conventional avalanche photo-diodes with only a few milliwatts of pump power. From such a large rate of photon pairs, it is then possible to select only pairs within a very narrow spectrum using filters. One possible problem is that even without very aggressive filtering, the pair to singles ratio is not very high (about 18%). Hence, most of the time,

the detectors are saturated due to detecting unuseable photons.

The other option is to perform SPDC within an optical cavity that also enhances the downconversion. In this way, the rate of downconversion photons is increased within the bandwidth defined by the cavity. This method was first tried out by Ou and Lu [166] who recorded a substantial increase in the photon pair rate within a narrow bandwidth. However, subsequent experiments have failed to produce high quality polarization entanglement. One reason for this is that the correlation time between a signal and idler photon become too large and too much noise is admitted into the system.

Alternatively, some groups have been pursuing entangled photon sources based on four-wave mixing in fibers [97] where they utilize the $\chi^{(3)}$ tensor. Although the elements of this tensor are weaker than in $\chi^{(2)}$, this is overcome by using very long fibers. An even more tentative possibility is to check for non-classical correlations in spontaneous light that is generated by warm atomic vapors. In these cases, the experimental setups are relatively simple and classical correlations have already been detected [167, 168, 169]. However, the conditions required for stable pair generation are still unknown and is an area of on-going research.

In short, contemporary entangled photon sources have not yet achieved the goal of having atomic-linewidth emission that is simultaneously bright and of high-quality entanglement. In the foreseeable future, the study of entangled photon sources will continue to be very active. Despite their limitations, bulk-crystal SPDC light sources still represent the cutting edge in generating entangled light, and will continue to play a role in basic research and validation of quantum communication protocols.

Appendix A

Vector Descriptions of Polarization States

This thesis makes extensive use of vector notations (known as Stokes and Jones Vectors) to express polarization states of light. Although the usage of polarization vectors is concentrated in chapter 4, they do appear throughout the thesis, and so it was decided that a separate section devoted to their derivation might be useful. When dealing with pure polarization states it is sometimes sufficient to denote the polarization state by the ket $|\rangle$ notation but it helps to be aware of the underlying mathematical description. It is hoped that this appendix will serve as an introduction to basic polarization concepts, as well as work as a consistency guide for the notation. We work exclusively with expressions for monochromatic light, which is a good approximation for a lot of the light fields that we encounter. We begin with a discussion of the transverse nature of light fields.

Light may be treated as a transverse electro-magnetic wave in cartesian space whose unit vectors are denoted by \mathbf{e}_x , \mathbf{e}_y and \mathbf{e}_z . The electric and magnetic fields oscillate in a plane that is transverse to its propagation direction z . The direction of the wave is characterized by its wave vector $\mathbf{k} = k\mathbf{e}_z$. The electric field of the wave is characterized by the electric field vector \mathbf{E} . The electric field vector can be decomposed into two components that oscillate in different orthogonal directions x - y such that $\mathbf{E} = \mathbf{E}_x + \mathbf{E}_y$

and the components are written as:

$$\mathbf{E}_x = E_{0x} \cos(kz - \omega t) \mathbf{e}_x \quad (\text{A.1})$$

$$\mathbf{E}_y = E_{0y} \cos(kz - \omega t + \epsilon) \mathbf{e}_y \quad (\text{A.2})$$

where $E_{0x,0y}$ are the field amplitudes in the relevant directions. The angular frequency of the wave is ω , and ϵ is the relative phase difference between the x and y components. A positive value of ϵ means that \mathbf{E}_y will lag behind \mathbf{E}_x in amplitude.

Each electric field vector \mathbf{E} is a unique combination of three values: E_{0x} , E_{0y} and ϵ , and represents a *polarization state*. In general, the electric field vector does not maintain a fixed *plane-of-polarization* (which is formed between the wave vector \mathbf{k} , and the electric field \mathbf{E}). This means that the plane-of-polarization generally rotates about the z -axis. Furthermore, the magnitude of the resultant electric field vector may change as it rotates. Such electric field vectors are called elliptically polarized light. We now describe some special cases of elliptical polarization.

A.1 Linear Polarization

The first set of special cases are encountered for electric field vectors that make a constant plane with the wave vector. Such waves are called *plane-polarized*, or *linearly polarized*. The simplest examples are when the electric field vector has only a single component, (e.g. $\mathbf{E} = E_{0x} \cos(kz - \omega t) \mathbf{e}_x$). In this thesis we say that the electric field vector with only the \mathbf{e}_x component is vertically polarized, and is denoted by $|V\rangle$. When the electric field vector has only the \mathbf{e}_y component it is horizontally polarized, $|H\rangle$. The polarization vectors $|H\rangle$ and $|V\rangle$, form a natural basis for polarization states, the *HV* polarization basis.

In general, the electric field can have both x - y components and still be linearly polarized. This occurs when ϵ takes integer multiples of π . If ϵ is equal to 0 or integer multiples of 2π , the two components are said to be *in phase*. If, however, ϵ is equal to odd-integer multiples of π , the two components are said to be 180° *out of phase*. For example, when $\epsilon = \pi$ and $\epsilon = 2\pi$, the electric field vector in the two cases may be

expressed as:

$$\mathbf{E}(\epsilon = 2\pi) = (E_{0x}\mathbf{e}_x + E_{0y}\mathbf{e}_y) \cos(kz - \omega t), \quad (\text{A.3})$$

$$\mathbf{E}(\epsilon = \pi) = (E_{0x}\mathbf{e}_x - E_{0y}\mathbf{e}_y) \cos(kz - \omega t). \quad (\text{A.4})$$

In both cases the resultant electric field oscillation is only in a single plane.

A special case arises when the field amplitude in the x and y directions are equal. Under the conditions for equation (A.3), we get a polarization plane that is half-way between the x and y directions. We call this the $+45^\circ$ state, denoted by $|+\rangle$. Under the conditions of equation (A.4), we get a polarization plane that is rotated by 90° to the $|+\rangle$ state. We call this the -45° state denoted by $|-\rangle$. These two states are orthogonal and also form a natural polarization basis, the $\pm 45^\circ$ basis. (Any set of orthogonal polarization states can form a basis, but the two bases mentioned here are used most often in this thesis).

A.2 Circular Polarization

The last pair of special cases we consider are for waves whose x and y components are equal in magnitude, but have a different value for the relative phase difference ϵ . In the first case, $\epsilon = \frac{\pi}{2} + 2m\pi$ where $m = 0, \pm 1, \dots$. In the second case, $\epsilon = -\frac{\pi}{2} + 2m\pi$. The resultant electric field vectors are respectively expressed as:

$$\mathbf{E}_R = E_0 (\cos(kz - \omega t)\mathbf{e}_x + \sin(kz - \omega t)\mathbf{e}_y) \quad (\text{A.5})$$

$$\mathbf{E}_L = E_0 (\cos(kz - \omega t)\mathbf{e}_x - \sin(kz - \omega t)\mathbf{e}_y) \quad (\text{A.6})$$

The polarization state in equation (A.5) is referred to as right-circular $|R\rangle$, because an observer looking at such an oncoming wave will see the vector \mathbf{E}_R rotating clockwise with constant magnitude. The vector in equation (A.6) is called left-circular $|L\rangle$, because a similar observer will see an anti-clockwise rotation of the vector \mathbf{E}_L . Together, they form another basis, the L - R polarization basis.

A.3 Jones Vector Notation

The first mathematical notation we will describe is relevant only for completely polarized light. It assumes that in the time interval under consideration, the light has only one polarization state. This is the Jones Vector Notation and utilizes the x - y components of the electric field vectors directly.

The Jones vector is written as

$$\mathbf{E} = \begin{pmatrix} E_{0x}e^{i(kz-\omega t)} \\ E_{0y}e^{i(kz-\omega t+\epsilon)} \end{pmatrix}. \quad (\text{A.7})$$

Hence, the states $|H\rangle$ and $|V\rangle$ are written as:

$$|H\rangle = \begin{pmatrix} E_{0x}e^{i(kz-\omega t)} \\ 0 \end{pmatrix} = E_{0x}e^{i(kz-\omega t)} \begin{pmatrix} 1 \\ 0 \end{pmatrix} \quad (\text{A.8})$$

$$|V\rangle = \begin{pmatrix} 0 \\ E_{0y}e^{i(kz-\omega t+\epsilon)} \end{pmatrix} = E_{0y}e^{i(kz-\omega t+\epsilon)} \begin{pmatrix} 0 \\ 1 \end{pmatrix}. \quad (\text{A.9})$$

For most cases in this thesis, it is sufficient to work with the normalized Jones vectors, where the sum of the square of both components is 1. Hence, in normalized vector notation the “special” states, $|H\rangle, |V\rangle, |+\rangle, |-\rangle, |L\rangle$ and $|R\rangle$ states are written in normalized notation as:

$$|H\rangle = \begin{pmatrix} 1 \\ 0 \end{pmatrix}, \quad |V\rangle = \begin{pmatrix} 0 \\ 1 \end{pmatrix} \quad (\text{A.10})$$

$$|R\rangle = \frac{1}{\sqrt{2}} \begin{pmatrix} 1 \\ i \end{pmatrix}, \quad |L\rangle = \frac{1}{\sqrt{2}} \begin{pmatrix} 1 \\ -i \end{pmatrix} \quad (\text{A.11})$$

$$|+\rangle = \frac{1}{\sqrt{2}} \begin{pmatrix} 1 \\ 1 \end{pmatrix}, \quad |-\rangle = \frac{1}{\sqrt{2}} \begin{pmatrix} 1 \\ -1 \end{pmatrix} \quad (\text{A.12})$$

With normalized Jones vectors, it is possible to decompose a polarized state into com-

ponents made up of states in another basis, e.g.:

$$|+\rangle = \frac{1}{\sqrt{2}} \begin{pmatrix} 1 \\ 1 \end{pmatrix} = \frac{1}{\sqrt{2}} (|H\rangle + |V\rangle) \quad (\text{A.13})$$

A.4 Stokes Vector Notation

The Jones vector notation is very concise. However, it suffers the disadvantage that it can only describe completely polarized light. The Stokes notation provides a vector notation that describes all polarization states.

We begin with the four Stokes parameters first described by G. G. Stokes in 1852 [170]. The Stokes parameters S_0, S_1, S_2, S_3 are related to the intensity of the incoming light that has passed through 4 different filters. We may choose the first filter to be a neutral density filter transmitting half of the incident light, while choosing the others to be polarization filters transmitting the states $|H\rangle, |R\rangle$ and $|+\rangle$. The intensities measured after these filters may be labeled as I_0, I_1, I_2 and I_3 respectively. The parameters are then defined as

$$S_0 = 2I_0 \quad (\text{A.14})$$

$$S_1 = 2I_1 - 2I_0 \quad (\text{A.15})$$

$$S_2 = 2I_2 - 2I_0 \quad (\text{A.16})$$

$$S_3 = 2I_3 - 2I_0 \quad (\text{A.17})$$

In this manner, the parameters $S_{1,2,3}$ reveal the composition of the input polarization state in terms of the three orthogonal bases.

We may also define the *degree of polarization* (DOP) as $\sqrt{S_1^2 + S_2^2 + S_3^2}/S_0$. In this case pure polarization states have a DOP equal to 1. States whose DOP are less than 1 have an element of randomness in the polarization; the polarization state that is completely random has a DOP of 0.

Recalling that the electric fields may be written as equations (A.1) and (A.2), we

can re-write the Stokes parameters:

$$S_0 = \langle E_{0x}^2 \rangle + \langle E_{0y}^2 \rangle \quad (\text{A.18})$$

$$S_1 = \langle E_{0x}^2 \rangle - \langle E_{0y}^2 \rangle \quad (\text{A.19})$$

$$S_2 = \langle 2E_{0x}E_{0y} \cos \epsilon \rangle \quad (\text{A.20})$$

$$S_3 = \langle 2E_{0x}E_{0y} \sin \epsilon \rangle \quad (\text{A.21})$$

$$(\text{A.22})$$

where we have placed the terms inside brackets to denote the time average. Hence, for randomly polarized light the Stokes parameters are $(\langle E_{0x}^2 \rangle + \langle E_{0y}^2 \rangle, 0, 0, 0)$ (the average of the sine and cosine functions in equations (A.1) and (A.2) go to 0), satisfying the requirement that the DOP is 0.

The Stokes parameters are sometimes arranged into a column vector, and treated as a vector (called the Stokes vector). In the same way as the Jones vectors, we may work with *normalized* Stokes vectors. Normalized Stokes vectors \vec{S} are obtained by dividing each of the Stokes parameters by the light intensity, such that $\vec{S} = (1, S_1/S_0, S_2/S_0, S_3/S_0)$. For example, the normalized Stokes for randomly polarized light will be written as $(1, 0, 0, 0)$.

Hence, we can work out the vector notation for our six “special” states:

$$|H\rangle = (1, 1, 0, 0), \quad |V\rangle = (1, -1, 0, 0) \quad (\text{A.23})$$

$$|R\rangle = (1, 0, 0, 1), \quad |L\rangle = (1, 0, 0, -1) \quad (\text{A.24})$$

$$|+\rangle = (1, 0, 1, 0), \quad |-\rangle = (1, 0, -1, 0) \quad (\text{A.25})$$

A reduced Stokes vector $\vec{S}_r = (S_1, S_2, S_3)/S_m$, identifies a point in the Poincare sphere (Fig. A.1). In the Poincare sphere, completely polarized states lie on the surface while randomly polarized light ($\text{DOP} < 1$) lies within the sphere. The completely unpolarized state is denoted by the point in the center. In this context, the magnitude of the reduced Stokes vector indicates the DOP. Also, for a Poincare sphere, we take the convention that linearly-polarized states lie on the equator while the $|R\rangle$ and $|L\rangle$

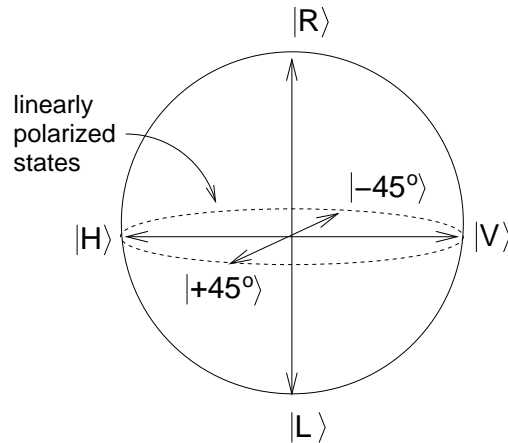


Figure A.1: Poincare sphere representation of polarization states. The Poincare sphere is a ball of unit radius. Pure polarization states lie on the sphere's surface while mixed polarization states reside within the sphere.

states lie at the poles.

In the language of spin- $\frac{1}{2}$ systems the reduced Stokes vector is the Pauli vector and the Poincare sphere is called the Bloch sphere. Hence, the polarization of quantum systems can also be described by a similar vector notation.

We have completed the description of polarization notations that are used in this thesis. We do not develop further the matrix algebra that comes with the Jones and Stokes vector notations (which are capable of describing the behavior of optical elements), as we do not use them very often in this thesis.

Appendix B

Partially Polarizing Beam Splitter (PPBS) Specification

To derive the intensity splitting ratio of the PPBS, we express the polarization states using Jones vectors unless we are describing the tetrahedron vectors \vec{b}_j . The tetrahedron (Stokes) vectors $\vec{b}_{j,k}$ have the scalar product property

$$\vec{b}_j \cdot \vec{b}_k = \frac{2}{3} + \frac{4}{3}\delta_{jk}. \quad (\text{B.1})$$

Recalling the parameters of the intensity splitting ratio of the PPBS x and y we see that a general input polarization state $\begin{pmatrix} \alpha \\ \beta \end{pmatrix}$ leads to the polarizations $\begin{pmatrix} x\alpha \\ y\beta \end{pmatrix}$ and $\begin{pmatrix} y\alpha \\ x\beta \end{pmatrix}$ in the transmitted and reflected arms of the PPBS respectively. In our polarimeter, light leaving the arms of the PPBS must be analyzed in two different polarization bases. Two orthogonal vectors that form a basis may be expressed as $\begin{pmatrix} \cos \theta \\ e^{i\phi} \sin \theta \end{pmatrix}$ and $\begin{pmatrix} -e^{-i\phi} \sin \theta \\ \cos \theta \end{pmatrix}$. This leads for example to the normalized light intensity falling on detector b_1

$$I_1/I_t = \left| \alpha x \cos \theta + \beta y e^{-i\phi} \sin \theta \right|^2. \quad (\text{B.2})$$

We choose a different measurement basis for detectors 3 and 4, for example light reaching detector 3 is

$$I_3/I_t = \left| \alpha y \cos \theta' + \beta x e^{-i\phi'} \sin \theta' \right|^2. \quad (\text{B.3})$$

Using the vector \vec{b}_1 as an example, equation (4.2) allows us to express the operator B_1 in terms of the measurement basis to fulfill equation (B.2):

$$\langle B_1 \rangle = \left| \alpha x \cos \theta + \beta y e^{-i\phi} \sin \theta \right|^2 \quad (\text{B.4})$$

$$= \left| \begin{pmatrix} x \cos \theta & y e^{-i\phi} \sin \theta \end{pmatrix} \begin{pmatrix} \alpha \\ \beta \end{pmatrix} \right|^2 \quad (\text{B.5})$$

The following choice of B_1 fulfills this condition

$$B_1 = \begin{pmatrix} x \cos \theta \\ y \sin \theta e^{i\phi} \end{pmatrix} \begin{pmatrix} x \cos \theta & y \sin \theta e^{-i\phi} \end{pmatrix}. \quad (\text{B.6})$$

Since the tetrahedron can be oriented arbitrarily we choose for convenience to measure the 45° linear polarization basis ($\theta = \pi/4$, $\phi = 0$) in the transmitted arm and the circular polarization basis ($\theta' = \pi/4$, $\phi' = \pi/2$) in the reflected arm. This reduces the measurement operators to only the beamsplitting parameters x and y

$$\left. \begin{matrix} B_1 \\ B_2 \end{matrix} \right\} = \frac{1}{2} \begin{pmatrix} x^2 & \pm xy \\ \pm xy & y^2 \end{pmatrix}, \quad \left. \begin{matrix} B_3 \\ B_4 \end{matrix} \right\} = \frac{1}{2} \begin{pmatrix} y^2 & \mp ixy \\ \pm ixy & x^2 \end{pmatrix},$$

which together with equation (4.2) allows us to express all tetrahedron vectors in terms of x and y

$$\left. \begin{matrix} \vec{b}_1 \\ \vec{b}_2 \end{matrix} \right\} = \begin{pmatrix} 1 \\ x^2 - y^2 \\ \pm 2xy \\ 0 \end{pmatrix}, \quad \left. \begin{matrix} \vec{b}_3 \\ \vec{b}_4 \end{matrix} \right\} = \begin{pmatrix} 1 \\ y^2 - x^2 \\ 0 \\ \mp 2xy \end{pmatrix}. \quad (\text{B.7})$$

From equation (B.1), we can write:

$$\vec{b}_1 \cdot \vec{b}_2 = \frac{2}{3} \text{ and } \vec{b}_1 \cdot \vec{b}_3 = \frac{2}{3}. \quad (\text{B.8})$$

This allows us to obtain an equation in x alone

$$36x^8 - 24x^4 + 1 = 0. \tag{B.9}$$

The last equation gives two solution sets; we choose the set where $x^2 = \frac{1}{2} + \frac{1}{2\sqrt{3}} \Rightarrow y^2 = \frac{1}{2} - \frac{1}{2\sqrt{3}}$.

Appendix C

Spectral Broadening in type-II non-collinear SPDC

In Spontaneous Parametric Down Conversion (SPDC), the generated photon pairs may be collected into single mode fibers. The emission of the photon pairs is said to be collinear if the emission direction is parallel to the pump beam. Otherwise, the emission is said to be non-collinear. The degree of non-collinearity is determined by a walk-off parameter Ξ , first introduced in equation (3.21). The parameter Ξ has a value of 0 for collinear emission and this value increases with the degree of non-collinearity (see section 3.2.3).

For a fixed set of experimental parameters (e.g. pump power) the spectral bandwidth of the collected downconversion photons will be different depending on the value of Ξ . The spectral bandwidth of collected downconversion photons can be quantified by its Full-Width at Half-Maximum (FWHM). In particular, the FWHM of the collected bandwidth has its smallest value for the collinear case ($\Xi = 0$). Larger values of Ξ lead to broader spectral bandwidths. This non-collinear spectral broadening is represented graphically in figure 3.2.

One consequence of spectral broadening is that the bandwidth optimizing procedure described in section 2.2.2 must be augmented by a correction factor. This factor can be obtained by comparing the FWHMs of the non-collinear and collinear cases. In order to do so, recall first that figure 3.2 is a plot of the longitudinal overlap Φ_z/l .

In general, the longitudinal overlap is an integral

$$\frac{\Phi_z}{l} = \int_0^1 du e^{-\Xi^2 u^2} \cos(\Delta\varphi u) \quad (\text{C.1})$$

In the collinear case, the longitudinal overlap is reduced to a sinc function as in equation (3.23). The expression for non-collinear cases is more involved, but is more easily determined with the aid of numerical tools like Mathematica. For the SPDC generation experiment of section 2.2.1, the non-collinearity of the setup is $\Xi = 0.933$. Hence, the expression for the longitudinal overlap after numerical integration is:

$$\begin{aligned} \left(\frac{\Phi_z}{l}\right)_{\Xi=0.933} &= 0.536e^{0.287(\Delta\varphi)^2} \sqrt{\pi} \\ &\times (\text{Erf}(0.933 - i0.536\Delta\varphi) + \text{Erf}(0.933 + i0.536\Delta\varphi)) \end{aligned} \quad (\text{C.2})$$

It is now possible to find the value of $\Delta\varphi$ at which the longitudinal overlap reaches 0.5. This is done by using the Mathematica function `FindRoot`. For example, to solve the collinear case, the complete Mathematica argument is:

$$\text{FindRoot}[\text{sinc}(\Delta\varphi) == \sqrt{0.5}\Delta\varphi, \{\Delta\varphi, 1\}]$$

This yields $\Delta\varphi = 1.39156$. Similarly, for the case of $\Xi = 0.933$, the overlap function reaches 0.5 when $\Delta\varphi = 1.578$. The spectral bandwidth is about 13% larger in the non-collinear case. Hence, the expected spectral bandwidth in section 2.2.2 is not 3.4 nm but approximately 4 nm.

Abbreviations

APD	Avalanche Photodiode
BB84	QKD protocol designed by Bennett and Brassard in 1984
BBO	β -Barium Borate
CC	Crystal Compensator
CHSH	Bell inequality designed by Clauser, Horne, Shimony and Holt
CPM	Critical Phase Matching
cps	counts per second
cw	continuous-wave
D _{1,2}	Detectors
E91	QKD protocol designed by Artur Ekert in 1991
EC	Error Correction
EPR	Einstein, Podolsky and Rosen
FPC	Fiber Polarization Control
FWHM	Full-Width at Half-Maximum
FWM	Four Wave Mixing
He-Ne	Helium-Neon
HWP	Half Wave Plate
IF	Interference Filters
Kwiat95	Polarization-entangled photon pair source designed by Paul Kwiat in 1995
LD	Laser Diode
LHV	Local Hidden Variables

LV	Local Variables
NLV	Non-local Variables
PA	Privacy Amplification
PBS	Polarizing Beam Splitter
PC	Personal Computer
PH	Pin Hole
PL	Pump light
PPBS	Partially Polarizing Beam Splitter
QBER	Quantum Bit Error Rate
QKD	Quantum Key Distribution
QM	Quantum Mechanics
QPM	Quasi-phase Matching
QWP	Quarter Wave Plate
RT	Receiving Telescope
SMF	Single Mode Fiber
SPDC	Spontaneous Parametric Down Conversion
ST	Sending Telescope
TU	Timing Unit
WP	Wave Plate

Bibliography

- [1] James K. Thompson, Jonathan Simon, Huanqian Loh, and Vladan Vuletic. A High-Brightness Source of Narrowband, Identical-Photon Pairs. *Science*, 313:74, 2006.
- [2] C. Bennett. Quantum Information and Computation. *Physics Today*, 48 (October)(10):24, 1995.
- [3] D. P. DiVincenzo. Quantum computation. *Science*, 269:255, 1995.
- [4] A. Ekert and R. Jozsa. Quantum computation and Shor's factoring algorithm. *Reviews of Modern Physics*, 68:733, 1996.
- [5] Andrew Steane. Quantum Computing. *Reports on Progress in Physics*, 61:117, 1998.
- [6] N. Gisin and R. T. Thew. Quantum communication. *Nature Photonics*, 1:165, 2007.
- [7] Jeremy O'Brien. Optical quantum computing. *Science*, 318:1567, 2007.
- [8] Benjamin Schumacher. Quantum coding. *Physical Review A (Atomic, Molecular and Optical Physics)*, 51:2738, 1995.
- [9] N. D. Mermin. From Cbits to Qbits: Teaching computer scientists quantum mechanics. *American Journal of Physics*, 71:23, 2003.
- [10] D. Bacon and N. D. Mermin. Two bits on qubits. *Physics Today*, 61 (March)(3):8, 2008.

- [11] Scott Aaronson. The Limits of Quantum Computers. *Scientific American*, March:50, 2008.
- [12] P. W. Shor. Polynomial-Time Algorithms for Prime Factorization and Discrete Logarithms on a Quantum Computer. *SIAM Journal on Scientific and Statistical Computing*, 26:1484, 1997.
- [13] Lou Grover. Quantum mechanics helps in searching for a needle in a haystack. *Physical Review Letters*, 79:325, 1997.
- [14] C. Bennett and G. Brassard. Quantum cryptography: Public-key distribution and coin tossing. In *Proceedings of IEEE International Conference on Computers, Systems and Signal Processing, Bangalore, India, December 1984*, pp. 175 - 179., 1984.
- [15] Charles H. Bennett, Gilles Brassard, Claude Crpeau, Richard Jozsa, Asher Peres, and William K. Wootters. Teleporting an unknown quantum state via dual classical and Einstein-Podolsky-Rosen channels. *Physical Review Letters*, 70:1895, 1993.
- [16] C. Bennett and S. Wiesner. Communication via one- and two-particle operators on Einstein-Podolsky-Rosen states. *Physical Review Letters*, 69:2881, 1992.
- [17] R. Rivest, A. Shamir, and L. Adleman. On digital signatures and public-key cryptosystems. Technical report, MIT, 1979.
- [18] A. K. Ekert. Quantum cryptography based on Bell's theorem. *Physical Review Letters*, 67(6):661-663, Aug 1991.
- [19] C. A. Fuchs, N. Gisin, R. B. Griffiths, C.-S. Niu, and A. Peres. Optimal eavesdropping in quantum cryptography. I. Information bound and optimal strategy. *Physical Review A (Atomic, Molecular and Optical Physics)*, 56(2):1163-1172, Aug 1997.
- [20] S. Wiesner. Conjugate Coding. *Sigact News*, 15:78, 1983.

-
- [21] W. K. Wothers and W. H. Zurek. A Single Quantum Cannot be Cloned. *Nature*, 299:802, 1982.
- [22] D. Dieks. Communicating by EPR devices. *Physics Letters A*, 92:271, 1982.
- [23] C. H. Bennett, F. Bessette, G. Brassard, L. Salvail, and J. Smolin. Experimental Quantum Cryptography. *Journal of Cryptology*, 5:3, 1992.
- [24] B. Huttner, N. Imoto, N. Gisin, and T. Mor. Quantum cryptography with coherent states. *Physical Review A (Atomic, Molecular and Optical Physics)*, 51:1863, 1995.
- [25] H. P. Yuen. Quantum amplifiers, quantum duplicators and quantum cryptography. *Journal of Optics B: Quantum and Semiclassical Optics*, 8:939, 1996.
- [26] Gilles Brassard, Norbert Lutkenhaus, Tal Mor, and Barry C. Sanders. Limitations on Practical Quantum Cryptography. *Physical Review Letters*, 85:1330, 2000.
- [27] Norbert Lütkenhaus. Security against individual attacks for realistic quantum key distribution. *Physical Review A (Atomic, Molecular, and Optical Physics)*, 61:052304, 2000.
- [28] Won-Young Hwang. Quantum Key Distribution with High Loss: Toward Global Secure Communication. *Physical Review Letters*, 91:057901, 2003.
- [29] E. Schrödinger. Die gegenwärtige Situation in der Quantenmechanik (The present situation in quantum mechanics). *Naturwissenschaften*, Nov, 1935.
- [30] Robert Eisberg and Robert Resnick. *Quantum Physics of Atoms, Molecules, Solids, Nuclei, and Particles*. John Wiley & Sons, 1985.
- [31] J. J. Sakurai. *Modern Quantum Mechanics*. Addison Wesley, 1994.
- [32] A. Einstein, B. Podolsky, and N. Rosen. Can quantum-mechanical description of physical reality be considered complete? *Physical Review*, 47:777, 1935.
- [33] D. Bohm. A Suggested Interpretation of the Quantum Theory in Terms of "Hidden" Variables. *Physical Review*, 85(2):166–179, Jan 1952.

-
- [34] H. Everett. “Relative State” Formulation of Quantum Mechanics. *Reviews of Modern Physics*, 29(3):454–462, Jul 1957.
- [35] J. S. Bell. On the Einstein-Podolsky-Rosen Paradox. *Physics*, 1:195, 1964.
- [36] J. S. Bell. *Speakable and Unsayable in Quantum Physics: Collected Papers on Quantum Philosophy*. Cambridge University Press, 2004.
- [37] Stuart J. Freedman and John F. Clauser. Experimental Test of Local Hidden-Variable Theories. *Physical Review Letters*, 28:938, 1972.
- [38] Edward S. Fry and Randall C. Thompson. Experimental Test of Local Hidden-Variable Theories . *Physical Review Letters*, 37:465, 1976.
- [39] J. F. Clauser, M. A. Horne, A. Shimony, and R. A. Holt. Proposed Experiment to Test Local Hidden-Variable Theories. *Physical Review Letters*, 23(15):880–884, Oct 1969.
- [40] A. Aspect, P. Grangier, and G. Roger. Experimental Realization of Einstein-Podolsky-Rosen-Bohm Gedankenexperiment: A New Violation of Bell’s Inequalities. *Physical Review Letters*, 49(2):91–94, Jul 1982.
- [41] Leslie E. Ballentine and J. P. Jarrett. Bell’s Theorem: Does Quantum Mechanics Contradict Relativity? *American Journal of Physics*, 55:696, 1987.
- [42] A. Aspect. Bell’s inequality test: more ideal than ever. *Nature*, 398:189, 1999.
- [43] A. Garg and N. D. Mermin. Detector inefficiencies in the Einstein-Podolsky-Rosen experiment. *Physical Review D*, 35(12):3831–3835, Jun 1987.
- [44] M. A. Rowe, D. Kielpinski, V. Meyer, C. A. Sackett, W. M. Itano, C. Monroe, and D. J. Wineland. Experimental violation of a Bell’s inequality with efficient detection. *Nature*, 409:791, 2001.
- [45] Gregor Weihs, Thomas Jennewein, Christoph Simon, Harald Weinfurter, and Anton Zeilinger. Violation of Bell’s Inequality under Strict Einstein Locality Conditions . *Physical Review Letters*, 81:5039, 1998.

-
- [46] W. Tittel, J. Brendel, B. Gisin, T. Herzog, H. Zbinden, and N. Gisin. Experimental demonstration of quantum correlations over more than 10 km. *Physical Review A (Atomic, Molecular, and Optical Physics)*, 57:3229, 1998.
- [47] S. Gröblacher, T. Paterek, R. Kaltenbaek, Č. Brukner, M. Zukowski, M. Aspelmeyer, and A. Zeilinger. An experimental test of non-local realism. *Nature*, 446:871, 2007.
- [48] C. Branciard, A. Ling, N. Gisin, C. Kurtsiefer, A. Lamas-Linares, and V. Scarani. Experimental Falsification of Leggett’s Nonlocal Variable Model. *Physical Review Letters*, 99(21):210407, 2007.
- [49] N. D. Mermin. Is the moon really there when nobody looks? Reality and quantum theory . *Physics Today*, 38 (April):47, 1985.
- [50] Antonio Acin, Nicolas Gisin, and Lluís Masanes. From Bell’s Theorem to Secure Quantum Key Distribution. *Physical Review Letters*, 97:120405, 2006.
- [51] K. Mattle, H. Weinfurter, P. G. Kwiat, and A. Zeilinger. Dense Coding in Experimental Quantum Communication. *Physical Review Letters*, 76(25):4656–4659, Jun 1996.
- [52] Dik Bouwmeester, Jian-Wei Pan, Klaus Mattle, Manfred Eibl, Harald Weinfurter, and Anton Zeilinger. Experimental quantum teleportation. *Nature*, 390:575, 1997.
- [53] D. Boschi, S. Branca, F. De Martini, L. Hardy, and S. Popescu. Experimental Realization of Teleporting an Unknown Pure Quantum State via Dual Classical and Einstein-Podolsky-Rosen Channels . *Physical Review Letters*, 80:1121, 1998.
- [54] T. Jennewein, C. Simon, G. Weihs, H. Weinfurter, and A. Zeilinger. Quantum Cryptography with Entangled Photons. *Physical Review Letters*, 84(20):4729–4732, May 2000.
- [55] H.-J. Briegel, W. Dr, J. I. Cirac, and P. Zoller. Quantum Repeaters: The Role of Imperfect Local Operations in Quantum Communication . *Physical Review Letters*, 81:5932, 1998.

- [56] L.-M. Duan, M. D. Lukin, J. I. Cirac, and P. Zoller. Long-distance quantum communication with atomic ensembles and linear optics. *Nature*, 414:413, 2001.
- [57] Brian Julsgaard, Jacob Sherson, J. Ignacio Cirac, Jaromr Fiurs caronek, and Eugene S. Polzik. Experimental demonstration of quantum memory for light. *Nature*, 432:482, 2004.
- [58] C. W. Chou, H. de Riedmatten, D. Felinto, S. V. Polyakov, S. J. van Enk, and H. J. Kimble. Measurement-induced entanglement for excitation stored in remote atomic ensembles. *Nature*, 438:828, 2005.
- [59] T. Chanelire, D. N. Matsukevich, S. D. Jenkins, S.-Y. Lan, T. A. B. Kennedy, and A. Kuzmich. Storage and retrieval of single photons transmitted between remote quantum memories. *Nature*, 438:833, 2005.
- [60] M. D. Eisaman, A. Andr, F. Massou, M. Fleischhauer, A. S. Zibrov, and M. D. Lukin. Electromagnetically induced transparency with tunable single-photon pulses. *Nature*, 438:837, 2005.
- [61] P. G. Kwiat, K. Mattle, H. Weinfurter, A. Zeilinger, A. V. Sergienko, and Y. H. Shih. New High-Intensity Source of Polarization-Entangled Photon Pairs. *Physical Review Letters*, 75(24):4337–4341, Dec 1995.
- [62] P. G. Kwiat, E. Waks, A. G. White, I. Appelbaum, and P. H. Eberhard. Ultrabright source of polarization-entangled photons. *Physical Review A (Atomic, Molecular, and Optical Physics)*, 60(2):R773–R776, Aug 1999.
- [63] A. Ling, Y. H. Peng, A. Lamas-Linares, and C. Kurtsiefer. Preparation of Bell states with Controlled White Noise. *Laser Physics*, 16:1140, 2006.
- [64] A. Ling, K. P. Soh, A. Lamas-Linares, and C. Kurtsiefer. An optimal photon counting polarimeter. *Journal of Modern Optics*, 56:1523, 2006.
- [65] A. Ling, K. P. Soh, A. Lamas-Linares, and C. Kurtsiefer. Experimental polarization state tomography using optimal polarimeters. *Physical Review A (Atomic, Molecular, and Optical Physics)*, 74(2):022309, 2006.

- [66] A. Ling, A. Lamas-Linares, and C. Kurtsiefer. Absolute emission rates of Spontaneous Parametric Down Conversion into single transverse Gaussian modes. *arXiv:0801.2220v1[quant-ph]*, 2008.
- [67] J. Brendel, N. Gisin, W. Tittel, and H. Zbinden. Pulsed Energy-Time Entangled Twin-Photon Source for Quantum Communication . *Physical Review Letters*, 82:2594, 1999.
- [68] R. T. Thew, S. Tanzilli, W. Tittel, H. Zbinden, and N. Gisin. Experimental investigation of the robustness of partially entangled qubits over 11 km. *Physical Review A (Atomic, Molecular and Optical Physics)*, 66:062304, 2002.
- [69] J. D. Franson. Bell inequality for position and time. *Physical Review Letters*, 62:2205, 1989.
- [70] W. Tittel, J. Brendel, H. Zbinden, and N. Gisin. Quantum Cryptography Using Entangled Photons in Energy-Time Bell States. *Physical Review Letters*, 84:4737, 2000.
- [71] Grgoire Ribordy, Jrgen Brendel, Jean-Daniel Gautier, Nicolas Gisin, and Hugo Zbinden. Long-distance entanglement-based quantum key distribution. *Physical Review A (Atomic, Molecular and Optical Physics)*, 63:012309, 2001.
- [72] I. Marcikic, H. de Riedmatten, W. Tittel, H. Zbinden, M. Legré, and N. Gisin. Distribution of Time-Bin Entangled Qubits over 50 km of Optical Fiber. *Physical Review Letters*, 93(18):180502, 2004.
- [73] Eugene Hecht. *Optics, 4th Edition*. Addison Wesley, 2002.
- [74] R. Ghosh and L. Mandel. Observation of Nonclassical Effects in the Interference of Two Photons. *Physical Review Letters*, 59:1903, 1987.
- [75] C. K. Hong, Z. Y. Ou, and L. Mandel. Measurement of subpicosecond time intervals between two photons by interference. *Physical Review Letters*, 59(18):2044–2046, Nov 1987.
- [76] Y. R. Shen. *The Principles of Nonlinear Optics*. Wiley Interscience, 2003.

- [77] W. H. Louisell, A. Yariv, and A. E. Siegman. Quantum Fluctuations and Noise in Parametric Processes I. *Physical Review*, 124:1646, 1961.
- [78] D. A. Kleinman. Theory of Optical Parametric Noise. *Physical Review*, 174:1027, 1968.
- [79] D. N. Klyshko. *Photons and Non-linear Optics*. Gordon and Breach Science Publishers, 1988.
- [80] C. K. Hong and L. Mandel. Theory of parametric frequency down conversion of light. *Physical Review A (Atomic, Molecular, and Optical Physics)*, 31(4):2409, Apr 1985.
- [81] D. C. Burnham and D. L. Weinberg. Observation of Simultaneity in Parametric Production of Optical Photon Pairs. *Physical Review Letters*, 25(2):84, Jul 1970.
- [82] Z. Y. Ou and L. Mandel. Violation of Bell's Inequality and Classical Probability in a Two-Photon Correlation Experiment. *Physical Review Letters*, 61:50, 1988.
- [83] Y. H. Shih and C. O. Alley. New Type of Einstein-Podolsky-Rosen-Bohm Experiment using pairs of light quanta produced by optical parametric down conversion. *Physical Review Letters*, 61:2921, 1988.
- [84] T. E. Kiess, Y. H. Shih, A. V. Sergienko, and C. O. Alley. Einstein-Podolsky-Rosen-Bohm experiment using pairs of light quanta produced by type-II parametric down-conversion. *Physical Review Letters*, 71(24):3893-3897, Dec 1993.
- [85] J. A. Armstrong, N. Bloembergen, J. Ducuing, and P. S. Pershan. Interactions between Light Waves in a Nonlinear Dielectric. *Physical Review*, 127:1918, 1962.
- [86] P. A. Franken and J. F. Ward. Optical Harmonics and Nonlinear Phenomena. *Reviews of Modern Physics*, 35:23, 1963.
- [87] M.M. Fejer, G.A. Magel, D.H. Jundt, and R.L. Byer. Quasi-phase-matched second harmonic generation: tuning and tolerances. *IEEE Journal of Quantum Electronics*, 28:2631, 1992.

- [88] S. Tanzilli, H. De Riedmatten, H. Tittel, H. Zbinden, P. Baldi, M. De Micheli, D. B. Ostrowsky, and N. Gisin. Highly efficient photon-pair source using periodically poled lithium niobate waveguide. *Electronics Letters*, 37:28, 2001.
- [89] K. Sanaka, K. Kawahara, and T. Kuga. New High-Efficiency Source of Photon Pairs for Engineering Quantum Entanglement. *Physical Review Letters*, 86(24):5620–5623, Jun 2001.
- [90] C. E. Kuklewicz, M. Fiorentino, G. Messin, F. N. C. Wong, and J. H. Shapiro. High-flux source of polarization-entangled photons from a periodically poled KTiOPO_4 parametric down-converter. *Physical Review A (Atomic, Molecular, and Optical Physics)*, 69(1):013807, 2004.
- [91] M. Fiorentino, G. Messin, C. E. Kuklewicz, F. N. C. Wong, and J. H. Shapiro. Generation of ultrabright tunable polarization entanglement without spatial, spectral, or temporal constraints. *Physical Review A (Atomic, Molecular, and Optical Physics)*, 69(4):041801, 2004.
- [92] M. Pelton, P. Marsden, D. Ljunggren, M. Tenger, A. Karlsson, A. Fragerman, C. Canalias, and F. Laurell. Bright, single-spatial-mode source of frequency non-degenerate, polarization-entangled photon pairs using periodically poled KTP. *Optics Express*, 12:3573, 2004.
- [93] A. B. U'Ren, C. Silberhorn, K. Banaszek, and I. A. Walmsley. Efficient Conditional Preparation of High-Fidelity Single Photon States for Fiber-Optic Quantum Networks. *Physical Review Letters*, 93(9):093601, 2004.
- [94] A. Fedrizzi, T. Herbst, A. Poppe, T. Jennewein, and A. Zeilinger. A wavelength-tunable fiber-coupled source of narrowband entangled photons. *Optics Express*, 15:15377, 2007.
- [95] M. Fiorentino, S. M. Spillane, R. G. Beausoleil, T. D. Roberts, P. Battle, and M. W. Munro. Spontaneous parametric down-conversion in periodically poled KTP waveguides and bulk crystals. *Optics Express*, 15:7479, 2007.

- [96] S. M. Spillane, M. Fiorentino, and Raymond G. Beausoleil. Spontaneous parametric down conversion in a nanophotonic waveguide. *Optics Express*, 15:8770, 2007.
- [97] X. Li, P. L. Voss, J. E. Sharping, and P. Kumar. Optical-Fiber Source of Polarization-Entangled Photons in the 1550 nm Telecom Band. *Physical Review Letters*, 94(5):053601, 2005.
- [98] R. E. Slusher, L. W. Hollberg, B. Yurke, J. C. Mertz, and J. F. Valley. Observation of Squeezed States Generated by Four-Wave Mixing in an Optical Cavity . *Physical Review Letters*, 55:2409, 1985.
- [99] J. Fan, M. D. Eisaman, and A. Migdall. Bright phase-stable broadband fiber-based source of polarization-entangled photon pairs . *Physical Review A (Atomic, Molecular and Optical Physics)*, 76:043836, 2007.
- [100] C. Kurtsiefer, M. Oberparleiter, and H. Weinfurter. High-efficiency entangled photon pair collection in type-II parametric fluorescence. *Physical Review A (Atomic, Molecular, and Optical Physics)*, 64(2):023802, Jul 2001.
- [101] M. H. Rubin, D. N. Klyshko, Y. H. Shih, and A. V. Sergienko. Theory of two-photon entanglement in type-II optical parametric down-conversion. *Physical Review A (Atomic, Molecular, and Optical Physics)*, 50:5122, 1994.
- [102] P. S. K. Lee, M. P. van Exter, and J. P. Woerdman. How focused pumping affects type-II spontaneous parametric down-conversion. *Physical Review A (Atomic, Molecular and Optical Physics)*, 72:033803, 2005.
- [103] C. K. Hong and L. Mandel. Experimental realization of a localized one-photon state. *Physical Review Letters*, 56(1):58–60, Jan 1986.
- [104] J. S. Neergard-Nielsen, B. Melholt Nielsen, H. Takahashi, A. I. Vistnes, and E. S. Polzik. High purity bright single photon source. *Optics Express*, 15:7940, 2007.
- [105] Alain Aspect, Philippe Grangier, and Grard Roger. Experimental Tests of Realistic Local Theories via Bell’s Theorem . *Physical Review Letters*, 47:460, 1981.

- [106] C. H. Monken, P. H. Souto Ribeiro, and S. Pádua. Optimizing the photon pair collection efficiency: A step toward a loophole-free Bell's inequalities experiment. *Physical Review A (Atomic, Molecular, and Optical Physics)*, 57(4):R2267, Apr 1998.
- [107] F. A. Bovino, P. Varisco, A. M. Colla, G. Castagnoli, G. D. Giuseppe, and A. V. Sergienko. Effective fiber-coupling of entangled photons for quantum communication. *Optics Communications*, 227:343, 2003.
- [108] S. Castellato, I. P. Degiovanni, A. Migdall, and M. Ware. On the measurement of two-photon single-mode coupling efficiency: in parametric downconversion photon sources. *New Journal of Physics*, 6:87, 2004.
- [109] D. Ljunggren and M. Tengner. Optimal focusing for maximal collection of entangled narrow-band photon pairs into single-mode fibers. *Physical Review A (Atomic, Molecular, and Optical Physics)*, 72(6):062301, 2005.
- [110] N. Boeuf, D. Branning, I. Chaperot, E. Dauler, S. Guerin, G. Jaeger, A. Muller, and A. Migdall. Calculating characteristics of noncollinear phase matching in uniaxial and biaxial crystals. *Optical Engineering*, 39:1016, 2000.
- [111] K. Koch, E. C. Cheung, G. T. Moore, S. H. Chakimakijan, and J. M. Liu. Hot spots in parametric fluorescence with a pump beam of finite cross section. *IEEE Journal of Quantum Electronics*, 31:769, 1995.
- [112] R. S. Klein, G. E. Kugel, A. Maillard, A. Sifi, and K. Polgar. Absolute Quantum Efficiency Measurements Using Correlated Photons: Toward a Measurement Protocol. *Optical Materials*, 22:163, 2003.
- [113] I. Marckic, A. Lamas-Linares, and C. Kurtsiefer. Free-space quantum key distribution with entangled photons. *Applied Physics Letters*, 89:101122, 2006.
- [114] S. Massar and S. Popescu. Optimal Extraction of Information from Finite Quantum Ensembles. *Physical Review Letters*, 74:1259, 1998.

- [115] R. Derka, V. Buzěk, and A. K. Ekert. Universal Algorithm for Optimal Estimation of Quantum States from Finite Ensembles via Realizable Generalized Measurement. *Physical Review Letters*, 80(8):1571–1575, Feb 1998.
- [116] J. I. Latorre, P. Pascual, and R. Tarrach. Minimal Optimal Generalized Quantum Measurements. *Physical Review Letters*, 81(7):1351–1354, Aug 1998.
- [117] R. D. Gill and S. Massar. State estimation for large ensembles. *Physical Review A (Atomic, Molecular, and Optical Physics)*, 61(4):042312, Mar 2000.
- [118] R. Schack, T. A. Brun, and C. M. Caves. Quantum Bayes rule. *Physical Review A (Atomic, Molecular, and Optical Physics)*, 64(1):014305, Jun 2001.
- [119] E. Bagan, M. Baig, R. Muñoz Tapia, and A. Rodríguez. Collective versus local measurements in a qubit mixed-state estimation. *Physical Review A (Atomic, Molecular, and Optical Physics)*, 69(1):010304, 2004.
- [120] J. Reháček, B.-G. Englert, and D. Kaszlikowski. Minimal qubit tomography. *Physical Review A (Atomic, Molecular, and Optical Physics)*, 70(5):052321, 2004.
- [121] D. F. V. James, P. G. Kwiat, W. J. Munro, and A. G. White. Measurement of qubits. *Physical Review A (Atomic, Molecular, and Optical Physics)*, 64(5):052312, Oct 2001.
- [122] R. M. A. Azzam. *Handbook of Optics, Vol. 2*. McGraw-Hill, New York, 1995.
- [123] A. Ambirajan and D. C. Look. Optimum angles for a polarimeter: part I. *Optical Engineering*, 34(6), 1651, 1995.
- [124] A. Ambirajan and D. C. Look. Optimum angles for a polarimeter: part II. *Optical Engineering*, 34(6), 1656, 1995.
- [125] R.M.A. Azzam and A. De. Optimal beam splitters for the division-of-amplitude photopolarimeter. *Journal of the Optical Society of America A*, 20(5), 955, 2003.
- [126] D. S. Sabatke, M. R. Descour, E. L. Dereniak, W. C. Sweatt, S. A. Kemme, and G. S. Phipps. Optimization of retardance for a complete Stokes polarimeter. *Optics Letters*, 25(11):802, 2000.

- [127] D. Bruß, M. Christandl, A. Ekert, B.-G. Englert, D. Kaszlikowski, and C. Macchiavello. Tomographic Quantum Cryptography: Equivalence of Quantum and Classical Key Distillation. *Physical Review Letters*, 91(9):097901, Aug 2003.
- [128] Y. C. Liang, D. Kaszlikowski, B.-G. Englert, L. C. Kwek, and C. H. Oh. Tomographic quantum cryptography. *Physical Review A (Atomic, Molecular, and Optical Physics)*, 68(2):022324, Aug 2003.
- [129] B.-G. Englert, D. Kaszlikowski, H. K. Ng, W. K. Chua, J. Řeháček, and J. Anders. Highly Efficient Quantum Key Distribution With Minimal State Tomography. *arXiv:quant-ph/0412075v3*, 2005.
- [130] K. Kraus. *States, Effects and Operations. Fundamental Notions of Quantum Theory. Lecture Notes in Physics Vol. 190*. Springer-Verlag, 1983.
- [131] B.-G. Englert, K. M. Tin, C. G. Goh, and H. K. Ng. Single-loop interferometer for minimal ellipsometry. *Laser Physics*, 15:7–9, 2005.
- [132] Edward L. O’Neill. *Introduction to Statistical Optics*. Dover Publications, 1991.
- [133] R. M. A. Azzam and F. F. Sudrajat. Single-layer-coated beam splitters for the division-of-amplitude photopolarimeter. *Applied Optics*, 44:190, 2005.
- [134] R.M.A. Azzam, I.M. Elminyawi, and A.M. El-Saba. General analysis and optimization of the four-detector photopolarimeter. *Journal of the Optical Society of America A*, 5:(5), 681, 1988.
- [135] A. Uhlmann. The transition probability in the state space of a *-algebra. *Reports on Mathematical Physics*, 9:273, 1976.
- [136] R. Jozsa. Fidelity for Mixed Quantum States. *Journal of Modern Optics*, 41:2315, 1994.
- [137] S. Gaertner, H. Weinfurter, and C. Kurtsiefer. Fast and compact multichannel photon coincidence unit for quantum information processing. *Review of Scientific Instruments*, 76:123108, 2005.

- [138] A. Gilchrist, N. K. Langford, and M. A. Nielsen. Distance measures to compare real and ideal quantum processes. *Physical Review A (Atomic, Molecular, and Optical Physics)*, 71(6):062310, 2005.
- [139] W. P. Grice and I. A. Walmsley. Spectral information and distinguishability in type-II down-conversion with a broadband pump. *Physical Review A (Atomic, Molecular, and Optical Physics)*, 56(2):1627–1634, Aug 1997.
- [140] Y.-H. Kim and W. P. Grice. Measurement of the spectral properties of the two-photon state generated via type II spontaneous parametric downconversion. *Optics Letters*, 30(8):908–910, 2005.
- [141] H. S. Poh, C. Y. Lum, I. Marcikic, A. Lamas-Linares, and C. Kurtsiefer. Joint spectrum mapping of polarization entanglement in spontaneous parametric down-conversion. *Physical Review A (Atomic, Molecular, and Optical Physics)*, 75(4):043816, 2007.
- [142] W. Wasilewski, P. Wasylczyk, P. Kolenderski, K. Banaszek, and C. Radzewicz. Joint spectrum of photon pairs measured by coincidence Fourier spectroscopy. *Optics Letters*, 31:1130, 2006.
- [143] R. F. Werner. Quantum states with Einstein-Podolsky-Rosen correlations admitting a hidden-variable model. *Physical Review A (Atomic, Molecular, and Optical Physics)*, 40(8):4277–4281, Oct 1989.
- [144] A. Cabello, A. Feito, and A. Lamas-Linares. Bell’s inequalities with realistic noise for polarization-entangled photons. *Physical Review A (Atomic, Molecular, and Optical Physics)*, 72(5):052112, 2005.
- [145] A. G. White, D. F. V. James, W. J. Munro, and P. G. Kwiat. Exploring Hilbert space: Accurate characterization of quantum information. *Physical Review A (Atomic, Molecular, and Optical Physics)*, 65(1):012301, Dec 2001.
- [146] Y.-S. Zhang, Y.-F. Huang, C.-F. Li, and G.-C. Guo. Experimental preparation of the Werner state via spontaneous parametric down-conversion. *Physical Review A (Atomic, Molecular, and Optical Physics)*, 66(6):062315, Dec 2002.

- [147] M. Barbieri, F. De Martini, G. Di Nepi, and P. Mataloni. Generation and Characterization of Werner States and Maximally Entangled Mixed States by a Universal Source of Entanglement. *Physical Review Letters*, 92(17):177901, 2004.
- [148] C.H. Bennett, G. Brassard, C. Crepeau, and U.M. Maurer. Generalized privacy amplification. *IEEE Transactions on Information Theory*, 41(6):1915–1923, 1995.
- [149] J. S. Bell. On the Problem of Hidden Variables in Quantum Mechanics. *Reviews of Modern Physics*, 38(3):447–452, Jul 1966.
- [150] V. Coffman, J. Kundu, and W. K. Wootters. Distributed entanglement. *Physical Review A (Atomic, Molecular and Optical Physics)*, 61(5):052306, Apr 2000.
- [151] C. H. Bennett, G. Brassard, and N. D. Mermin. Quantum cryptography without Bell’s theorem. *Physical Review Letters*, 68(5):557–559, Feb 1992.
- [152] J. Bienfang, A. Gross, A. Mink, B. Hershman, A. Nakassis, X. Tang, R. Lu, D. Su, C. Clark, C. Williams, E. Hagley, and J. Wen. Quantum key distribution with 1.25 Gbps clock synchronization. *Optics Express*, 12(9):2011–2016, 2004.
- [153] A. Acin, N. Brunner, N. Gisin, S. Massar, S. Pironio, and V. Scarani. Device-Independent Security of Quantum Cryptography against Collective Attacks. *Physical Review Letters*, 98(23):230501, 2007.
- [154] Leslie E. Ballentine. *Quantum Mechanics A Modern Development*. World Scientific, 1999.
- [155] G. Brassard and L. Salvail. Secret key reconciliation by public discussion. In *Advances in Cryptology: Eurocrypt. 93*, page 410, 1993.
- [156] A. J. Leggett. Nonlocal Hidden-Variable Theories and Quantum Mechanics: An Incompatibility Theorem. *Foundations of Physics*, 33:1469, 2003.
- [157] S. Popescu and D. Rohrlich. Quantum nonlocality as an axiom. *Foundations of Physics*, 24:379, 1994.

- [158] N. J. Cerf, N. Gisin, S. Massar, and S. Popescu. Simulating Maximal Quantum Entanglement without Communication. *Physical Review Letters*, 94(22):220403, 2005.
- [159] N. Brunner, N. Gisin, and V. Scarani. Entanglement and non-locality are different resources. *New Journal of Physics*, 7:88, 2005.
- [160] A. Suarez and V. Scarani. Does entanglement depend on the timing of the impacts at the beam-splitters? *Physics Letters A*, 232:9, 1997.
- [161] H. Zbinden, J. Brendel, N. Gisin, and W. Tittel. Experimental test of nonlocal quantum correlation in relativistic configurations. *Physical Review A (Atomic, Molecular, and Optical Physics)*, 63:022111, 2001.
- [162] S. Parrott. Comments on “An experimental test of non-local realism” by S. Groeblacher, T. Paterek, R. Kaltenbaek, C. Brukner, M. Zukowski, M. Aspelmeyer, and A. Zeilinger, *Nature* 446 (2007), 871-875. *arXiv:0707.3296v2[quant-ph]*, 2007.
- [163] Ph. Eberhard. *A Realistic Model for Quantum Theory with a Locality Property*. Springer, Berlin, 1989.
- [164] D. Bohm and B. J. Hiley. *The undivided universe*. Routledge, N. Y., 1993.
- [165] B. F. Toner and D. Bacon. Communication Cost of Simulating Bell Correlations. *Physical Review Letters*, 91(18):187904, Oct 2003.
- [166] Z. Y. Ou and Y. J. Lu. Cavity Enhanced Spontaneous Parametric Down-Conversion for the Prolongation of Correlation Time between Conjugate Photon. *Physical Review Letters*, 83:2556, 1999.
- [167] A. S. Zibrov, M. D. Lukin, and M. O. Scully. Nondegenerate Parametric Self-Oscillation via Multiwave Mixing in Coherent Atomic Media. *Physical Review Letters*, 83:4049, 1999.
- [168] K. Motomura, M. Tsukamoto, A. Wakiyama, K. Harada, and M. Mitsunaga. Observation of correlated anti-Stokes emissions by multiwave mixing in sodium

-
- vapor. *Physical Review A (Atomic, Molecular, and Optical Physics)*, 71:043817, 2005.
- [169] K. Harada, M. Ogata, and M. Mitsunaga. Four-wave parametric oscillation in sodium vapor by electromagnetically induced diffraction. *Optics Letters*, 32:1111, 2007.
- [170] George Gabriel Stokes. On the composition and resolution of streams of polarized light from different sources. *Transactions Cambridge Philosophical Society*, 9:399, 1852.

Publications

- A. Ling, Y.-H. Peng, A. Lamas-Linares and C. Kurtsiefer. “Preparation of Bell states with Controlled White Noise”. *Laser Physics*, Vol. 16, pg. 1140 (2006).
- A. Ling, K.-P. Soh, A. Lamas-Linares and C. Kurtsiefer. “An optimal photon counting polarimeter”. *Journal of Modern Optics*, Vol. 10, pg. 1523 (2006).
- A. Ling, K.-P. Soh, A. Lamas-Linares and C. Kurtsiefer. “Experimental polarization state tomography using optimal polarimeters”. *Physical Review A*, Vol. 73, pg. 022309 (2006)
- C. Branciard, A. Ling, N. Gisin, C. Kurtsiefer, A. Lamas-Linares and V. Scarani, “Experimental Falsification of Leggett’s Non-local Variable Model”. *Physical Review Letters*, Vol. 99, pg. 210407 (2007)
- A. Ling, A. Lamas-Linares and C. Kurtsiefer. “Absolute rate of SPDC emission into single transverse modes”. URL=<http://arxiv.org/pdf/0801.2220>.
- A. Ling, M. Peloso, I. Marcikic, A. Lamas-Linares, V. Scarani and C. Kurtsiefer. “Experimental implementation of device-independent QKD”. In preparation.

Index

- $\chi^{(2)}$, 13, 33, 109
- $\chi^{(3)}$, 16, 109
- Řeháček, Jaroslav, 48
- Abbreviations, 120
- accidental coincidences, 25, 79
- Armstrong, JA, 15
- Aspect, Alain, 7
- atomic memories, 108
- bandwidth
 - optimization, 20
 - spectral, 69
- BB84, 3, 12, 84
- BBO, 19
- Bell states, 18
- Bell's inequality, 7, 13, 85, 96
 - detection loophole, 8
 - fair-sampling, 8
 - locality loophole, 8
- Bell's theorem, 7
- Bell, John, 7
- Bennett, Charles, 3, 84
- bi-partite, 5
- blackbody, 79
- Bohm, David, 7
- Brassard, Giles, 3, 84
- Burnham, David, 14
- CHSH, 7, 85
- Clauser-Horne-Shimony-Holt, *see* CHSH
- coincidence time window, 25, 78
- collection bandwidth, 19
- coupling efficiency, 32
- density matrix, 59, 82
- E91, 4, 84
- Ekert, Artur, 4, 85
- emission rate
 - absolute , 40
 - spectral, 39
- entangled photons
 - sources, 9
 - polarization-entangled, 12
 - sources, 13
 - time-bin entangled, 12
- entanglement, 4
 - entangled state, 5, 22
 - quality, 9, 22
- EPR, 6, 96
 - element-of-reality, 96
- error correction, 85
- Everett, Hugh, 7

- Fedrizzi, A, 15
- Fermi's Golden Rule, 39
- fidelity, 57
- four-wave mixing, 15
- Franken, JF, 15
- Franson, James, 12
- FWM, *see* four-wave mixing
- Gaussian beam
 - paraxial, 31
- Gröblacher, S., 97
- Grice, Warren, 70
- Grover search method, 2
- Hamiltonian
 - interaction, 36
- Heisenberg Uncertainty Principle, 3
- Hong, CK, 14
- HWP, 25
- idQuantique, 4
- James, Daniel, 51
- Kleinman, DA, 14, 32
- Klyshko, Daniel, 14, 32
- Kurtsiefer, Christian, 19
- Kwiat, Paul, 14
- Lütkenhaus, Norbert, 4
- Leggett, Anthony, 96
- LHV, *see* Local Hidden Variable
- Local Hidden Variable, 6
- local variable, 96
- Louisell, WH, 13
- MagiQ, 4
- Mandel, Louis, 14
- mismatch
 - wave vector, 37
- monochromator, *see* spectrometer
- no-cloning theorem, 3, 84
- non-local variables, 97
- optical fibers
 - single mode, 31
- overlap integral, 36
- Pauli matrices, 49
- PBS, 25, 50
- periodic poling, 15
- phase matching
 - critical, 14
 - quasi, 14
- phase mismatch, 37
 - longitudinal, 38, 108
- polarimeter, 48, 50
 - calibration, 53
- polarimetry, 46
 - accuracy, 62
 - efficiency, 61
 - minimal and optimal, 47
 - scaling law, 68
 - tetrahedron, 48
- polarization
 - Jones vector, 23, 48

- Poincare sphere, 48
- Stokes vector, 48
- polarization-entangled state, 18
- POVM, 48, 61
- PPBS, 50
- privacy amplification, 85
- QBER, 94
- qbit, *see* qubit
- QKD, 4, 84
 - bit rate, 94
- quantum communication, 3, 9, 12, 107
- quantum computation, 3
- quantum information theory, 3
- quantum repeaters, 108
- qubit, 2, 9
 - state tomography, 46
- Rayleigh range, 21
- Schrödinger, Erwin, 5
- Shor algorithm, 2
- single transverse mode, 31
- singlet, 23
- SPDC, *see* Spontaneous Parametric Down Conversion
 - Conversion
- spectral brightness, 9, 108
- spectral correlations, 69
- spectrometer, 70
- Spontaneous Parametric Down Conversion,
 - 13, 14, 16, 31, 69, 107
 - collection mode, 35
 - pump mode, 34
 - coincidence spectra, 71
 - conversion efficiency, 32, 44
 - singles spectra, 22
 - type I, 14
 - type II, 14, 16
 - collinear, 17
 - emission angle, 21
 - emission profile, 21
 - non-collinear, 17, 20
- Stern-Gerlach
 - apparatus, 5
- superposition, 2
- tetrahedron, 61
 - model, 62
- thick crystal regime, 38
- thin crystal regime, 38
- tomography, *see* polarimetry
 - single photon ensemble, 57
 - two photon ensemble, 58
- trace distance, 62
- Vernam cipher, 84
- visibility, 25, 72, 79
- walk-off
 - longitudinal, 18
 - parameter, 38
 - transverse, 18
- Walmsley, Ian, 70
- Ward, PA, 15

weak coherent pulses, 4

Weinberg, Donald, 14

Werner state, 77

 coincidence spectra, 83

Wiesner, Stephen, 3

Wigner inequality, 87